# A COMPACT, RECONFIGURABLE PENNING TRAP FOR QUANTUM APPLICATIONS

A Dissertation
Presented to
The Academic Faculty

By

Brian J. McMahon

In Partial Fulfillment
of the Requirements for the Degree
Doctor of Philosophy in the
School of Physics
Department of Physics

Georgia Institute of Technology

August 2021

**A COMPACT, RECONFIGURABLE PENNING TRAP FOR QUANTUM APPLICATIONS**

Thesis committee:


Dr. Brian C. Sawyer
Chief Engineer, Quantum Systems Division
*Georgia Tech Research Institute*

Dr. Robert Wyllie
Division Chief, Quantum System Division
*Georgia Tech Research Institute*

Dr. Michael Chapman
Department of Physics
*Georgia Institute of Technology*

Dr. Martin Mourigal
Department of Physics
*Georgia Institute of Technology*

Dr. Ali Adibi
Department of Electrical and Computer Engineering
*Georgia Institute of Technology*



Date approved: July 28, 2021

Our virtues and our failings are inseparable, like force and matter. When they separate, man is no more.

*-Nikola Tesla*

For my parents, Tim and Michele.

## ACKNOWLEDGMENTS

The journey for my doctoral degree really began 15 years ago, when I found that physics was my passion. My parents always encouraged whichever path was of most interest to me. They have supported me throughout- mentally, emotionally, and physically. I wouldn't be here today without them. This thesis is dedicated to them. I am also grateful to my sister, who has helped me with a few mathematical concepts during the arduous period of taking graduate courses.

Once in college, I was fortunate enough to work for Professor Kenneth Brown at Georgia Tech. In his lab, my passion for quantum physics grew. I owe a great deal to his mentorship and support. In his lab, I learned the basics of experimental physics under the guidance of then postdoc, Dr. Gang (Rick) Shu. Thank you, Rick.

As the experimental lead on a project in Ken's lab, I was supported by Dr. Curtis Volin and Dr. Alexa Harter, (Georgia Tech Research Institute (GTRI)). Without the confidence of Ken, Alexa, and Curtis, I wouldn't be where I am today. They gave me the opportunity and for that I will always be grateful. After moving to a position at GTRI, I was mentored by some amazing colleagues, Dr. Jason Amini, Dr. Creston Herold, and Dr. Robert Wyllie. I will always be thankful for them. Each one of them has taught me different methods for experimental work and each has helped mold me to be the productive research scientist that I am now.

Working with Dr. Brian Sawyer has been an honor. He is truly a gifted experimentalist with an equally strong theoretical intuition. I genuinely enjoy the time we spend working together, and the time we spend bouncing ideas off each other. I have learned countless things from him over our few years working together. Words cannot express the gratitude I have for his mentorship and being my GTRI advisor.

I am very thankful to Dr. Michael Chapman. He is always supportive and willing to listen with helpful comments/ concerns. I am indebted to him for taking the role as my

advisor.

## TABLE OF CONTENTS

## LIST OF TABLES

## LIST OF FIGURES

## LIST OF ACRONYMS

**2D** two dimensional

**AMO** atomic, molecular, and optical

**AOM** acousto-optic modulator

**AR** anti-reflection coating

**BGIT** Brown-Gabrielse Invariance Theorem

**CF** conflat

**CTE** coefficient of thermal expansion

**DAC** digital to analog converter

**DDS** direct digitial synthesizer

**EMCCD** electron multiplying charge-coupled device

**EOM** electro-optic modulator

**FOTOC** fidelity out-of-time-order correlators

**FWHM** full width at half maximum

**GNSS** global navigation satellite system

**GPS** global positioning service

**GTRI** Georgia Tech Research Institute

**HCI** highly charged ion

**ID** inner diameter

**LUT** look-up table

**NIST** National Institute for Standards and Technology

**OD** outer diameter

**PCF** photonic crystal fiber

**PD** photodiode

**PMT** photon multiplier tube

**PNT** position, navigation, and timing

**QED** quantum electrodynamics

**REM** rare-earth permanent magnets

**RF** radio frequency

**SNR** signal-to-noise ratio

**SS** stainless steel

**SWAP** size, weight, and power

**TTL** transistor-transistor logic

**UHV** ultra-high vacuum

**UV** ultraviolet

## SUMMARY

Penning ion traps are versatile tools for studying atomic and molecular physics. They use static electric and magnetic fields to confine charged particles in 3-dimensional space. Most Penning traps employ a magnetic field produced by a large superconducting coil. However, in this thesis I detail the design and creation of compact, reconfigurable permanent magnet Penning trap based on rare earth permanent magnets instead of a superconducting coil [1]. For the first time in a permanent magnet trap, I demonstrate Doppler laser cooling of calcium-40 and beryllium ions. I perform magnetic gradiometry across the trap region using transport of an ion crystal to probe different positions. The magnetic field is found directly by implementing a spin flip across the ground state Zeeman-shifted levels. The magnetic field uniformity and temporal stability are each measured to a precision of $\sim 10$ ppb, demonstrating the quality of the magnetic field environment.

Beryllium ions are co-trapped with calcium ions, which serve as a sympathetic coolant. This enables long integration times for measurement of the beryllium ions' hyperfine structure. The nearest magnetic-field-insensitive (clock) transition of $^{9}Be^{+}$ is probed for up to $0.5$ s with no observed loss of coherence. However, several challenges remain for working with $^{9}Be^{+}$ as an atomic clock ion. Planned improvements to the system are discussed.

# CHAPTER 1
# INTRODUCTION

## 1.1 Penning Traps

In the twentieth century, a quantum theory was developed to describe the behavior of small systems near atomic size. These small systems behave in a way that is counter-intuitive to the mechanics we as humans observe every day. Classical physics fails to describe physical systems at the smallest scales. The dynamics of these systems are probabilistic in nature. Physicists have found that the system properties, such as the internal energy of an atom, take on discrete rather than continuous values. Quantum states can also exhibit superposition and entanglement - properties with no classical analogues. The values of these energy levels are determined by the interaction of the constituent particles via fundamental forces with each other and their environment. The study of this structure and interactions is the focus of atomic physics.

Internal atomic states and transition frequencies are not only determined by interactions between the constituent particles. External electromagnetic fields and colliding particles, for example, can perturb the energies and lifetimes of atomic states. In order to accurately measure fundamental atomic properties, the atoms must be isolated from the environment. This can be achieved by placing the atoms in a vacuum like found in deep space. In a vacuum, the atoms under study have largely reduced collision rates with other background gas atoms. Next, a method is needed to confine or trap the particles at a localized position where they can be observed. By ionizing the atoms, we can use electromagnetic forces to strongly couple the ion's motion to applied electromagnetic fields, thus, constraining their motion or 'trapping' them. Hans Dehmelt first demonstrated a trap using these principles in a device he named the Penning trap, after inspiration from F. M. Penning [2]. In this trap,

a quadrupole electric field confines the ions in one spatial dimension, while static magnetic fields confine the particle in the other two spatial dimensions. In parallel, Wolfgang Paul developed the quadrupole ion trap, which was later named the Paul trap [3]. The Paul trap uses a RF electric field to constrain the ions in two dimensions and a static electric field for the other dimension. In 1989, Hans Dehmelt shared the Nobel Prize with Wolfgang Paul and Norman Ramsey[1] for developing ion trapping techniques [4].

Many experiments have since been performed that leverage or study the quantum behavior of charged particles. In particular, Penning traps are used for precision mass spectrometry [5, 6, 7, 8], quantum information science/ simulation [9, 10, 11, 12, 13, 14, 15, 16, 17, 18], atomic clocks/ atomic sensing [19, 20, 21, 22], and particle/ antiparticle studies [23, 8, 24, 25]. Paul traps are also used for these areas of study, but Penning traps have some advantages over Paul traps. In contrast to Paul traps, Penning traps require only static electric and magnetic fields for ion confinement. As such, they induce no driven RF micromotion. When trapping cold ion ensembles, one can create 2D or 3D ion Coulomb crystals on demand by controlling the collective crystal rotation frequency. Penning traps do require a large uniform magnetic field for operation. This is usually supplied from a large superconducting coil ($> 1$ m$^3$). Optical access to the trap region requires routing laser beams around the superconducting magnet. However, in this thesis we demonstrate a new compact and reconfigurable apparatus for a Penning trap that relies on rare earth permanent magnets for magnetic field generation [1].

In the field of quantum information science, some of the largest quantum simulation experiments have been performed in Penning traps. Entanglement of $> 200$ ions was generated via application of a quantum Ising interaction [12, 26]. A simulator of the Dicke Hamiltonian was implemented in a two dimensional (2D) crystal with $\sim 70$ ions [15]. Later, R. J. Lewis-Swan et al. (2019) demonstrated fidelity out-of-time-order correlators (FOTOC) in the Dicke model using a Penning trap [27]. Jain, et al. (2020) proposed a

[1]Norman Ramsey's portion of the prize was "for the invention of the separated oscillatory fields method and its use in the hydrogen maser and other atomic clocks" [4]. This technique is used in chapter 8.

method for digital quantum computing via arrays of micro-Penning traps [17]. Many of these experiments use beryllium ions, because beryllium has a low mass, $9$ amu, and lacks the low lying D-states which complicate laser cooling. However, the Thompson group at Imperial College introduced laser-cooling of calcium-40 ions in a Penning trap [28]. They implemented sideband cooling of the radial and axial modes of a 1D array of ions in a Penning trap in efforts towards Penning trap quantum computing [29, 18].

Penning traps are also used for measurements of fundamental constants. For example, precision Penning traps were used to make a $300$ ppt measurement of the proton magnetic moment [25] and a $1.5$ ppb measurement of the antiproton magnetic moment [8]. Koehler et al. measured the g-factor difference between lithium-like calcium isotopes, a variation explained by quantum electrodynamics (QED) [30].

The inherent frequency dependence of the ion's motion with respect to its mass enables these measurements. Penning trap systems have facilitated the most precise measurements of particle mass. For example, the most precise value for the deuteron mass was measured [6]. The development of novel mass measurement techniques are ongoing. In 2020, a new technique was used to distinguish the difference of the an highly charged ion (HCI)'s valence electron energy in an excited metastable state compared to its ground state via mass measurement [5]. This technique uses Einstein's $E = mc^2$ relation to make the comparison. The authors claim the method will be used for looking for other soft-X-ray frequency references for potential atomic clock candidates [5].

The major inspiration for the work in this thesis comes from the atomic clock demonstration done by Bollinger, et al. (1991) [19]. In this publication, they operate their Penning trap at the clock field. The clock field is the magnetic field value for which the ion has a pair of neighboring states that form a linearly insensitive transition to magnetic field fluctuations. In the beryllium ion's ground state manifold, a clock transition is formed at $0.8194$ T for a pair of neighboring hyperfine states. Bollinger, et al (1991) probes the hyperfine transition with a Ramsey delay time of $550$ s [19]. The use of such a standard for an atomic

clock is promising, but unfortunately uses large superconducting magnets. A major goal of the work detailed in this thesis is to drastically reduce the size of the Penning trap frequency reference while maintaining atomic frequency stability.

## 1.2 Atomic Clocks

Of the interesting phenomena found while studying atoms, it was discovered that these systems have discrete energy levels. Because all atoms of a species are identical, the discrete energy levels of an atomic system are always identical to those of another atom of the same element and isotope. This means that the energy needed to change an atom's electronic state is identical for all atoms of that isotope. Electromagnetic radiation of the right energy, or equivalently frequency, can deliver the exact energy to the atom to change its internal state. Matching the frequency of radiation to the atom's level spacing precisely matches the frequency to all atoms of that isotope. This property makes atoms an ideal reference for time. The inherent universality of the atomic structure gives us the ability to measure time via the frequency of the radiation that interacts with the atom. Currently, this is the most precise way to measure time and has been adopted internationally. The definition of the second is defined by the Bureau International des Poids et Mesures as the number of oscillations of the electromagnetic radiation in the unperturbed ground state hyperfine structure of the cesium 133 atom [31].

In addition to accurate and precision timing, atomic clocks enable other scientific advances, see [32] and sources therein. Examples include tests of fundamental physics, measuring variations of fundamental constants, improvements to position, navigation, and timing (PNT), and geodesy. Atomic clocks enable tests of fundamental physics such as the equivalence principle and therefore general relativity. In general relativity, the equivalence principle is related to the local Lorentz invariance, local position invariance, and the universality of the gravitational redshift [32]. A gravitational redshift causes two clocks at different gravitational potentials to traverse time at different rates. The ratio of two clocks'

frequencies located in different gravitational potentials should agree with the predictions of general relativity. Any modulation from the expected frequency ratio is a sign of local position variance and a violation of general relativity [32]. In addition to tests of general relativity, portable atomic clocks could utilize the effects of gravitational redshifts at varied latitudes and longitudes to map the matter distribution/shape of the earth [32].

Fundamental constants can also be probed through the properties of the clock atoms. Clock transitions between electronic states can be parameterized as a function of the fine structure constant, $\alpha$; clock transitions between hyperfine states can be parameterized as a function of $\alpha$ and the proton-to-electron mass ratio, $\mu$. Ratios of these transitions allow one to bound the temporal variations of $\alpha$ and $\mu$ [33]. For example, Huntemann, et al. [33] bounded the fractional rate of change of $\alpha$ and $\mu$ at the $\sim 10^{-16}$ level using measurements of a transition in $^{171}Yb^{+}$, two caesium fountain clocks, and data from previous measurements. Rosenband, et al. [34] bounded $\dot{\alpha}/\alpha$ at a level of $\sim 10^{-17}$.

Having precision timing standards allows for accurate PNT. In an article by Kitching [35], he gives an overview of the need for better chip-scale atomic frequency references. The global navigation satellite system (GNSS) uses measurements of position and time from a minimum of four satellites in order to pinpoint locations on the Earth. GNSS receivers rely on two different communication protocols for receiving position and timing information, the precise code (P(Y) code) and the civilian access (C/A code). For GNSS receivers that only rely on P(Y) code, their acquisition time is related to how far out of sync they are. More accurate/precise atomic clocks would reduce these receivers' triangulation time. Older military hardware relys on C/A code in addition to the global positioning service (GPS) P(Y) code to triangulate position, but C/A code is sensitive to jamming by adversaries. High accuracy/low drift clocks would remove the need for C/A code and shield receivers from jamming. In addition, some environments prevent the use of four satellites, because they either aren't available or communications are blocked. A receiver outfitted with one of these high accuracy/ low drift clocks could also reduce the number of satellites

needed for triangulation [35, 36].

### 1.2.1 Limitations of Available Clocks

Currently, the most stable atomic clocks rely on optical atomic transitions and have optical fractional frequency uncertainties at the $\sim 10^{-18} - 10^{-19}$ level. For example, some clocks at this level are implemented with strontium atoms in optical lattices [37] or with an aluminum-27 ion in a Paul trap [38, 39, 40]. All of these clock experiments aim to create a new SI standard of time with an optical transition. Here, we seek to push the boundaries of deployable atomic clocks, within the constraints of size, weight, and power (SWAP). There are lower SWAP, commercially available options for atomic clocks, but they do not achieve the same performance as a laboratory grade atomic clock. Most of these solutions operate via spectroscopy of neutral rubidium or cesium atoms. Alkaline earth metal ions and alkali elements such as these have a single valence electron which is used to perform spectroscopy. The interaction of the nuclear and electron spins of these isotopes results in a splitting of the fine structure with magnitudes in the megahertz- gigahertz range, which is a convenient place for RF electronics [41].

These commercial clocks all operate via spectroscopy of neutral atoms and their clock stability is commonly compared using Allan deviation. The Allan deviation is half of the average of sample variances over the frequency dataset for different averaging times [42]. This form of the Allan deviation can be expressed as

$$\sigma_y(\tau) = \sqrt{\frac{1}{2}\left\langle (\bar{y}_{n+1} - \bar{y}_n)^2 \right\rangle} \tag{1.1}$$

where $y$ is the frequency, $\bar{y}_n$ is the average frequency over a time step of length $\tau$, and $\bar{y}_{n+1}$ is the average frequency over the next time step in the data.

A sample of commercial clocks' performance is shown in the Allan deviation plot below. The most stable is the Microsemi 5071A which is slightly smaller than a standard

3U rack unit and boasts an Allan deviation of $5.0 \times 10^{-12}$ at 1 s [43]. This clock operates via spectroscopy of a Cesium beam. Microsemi also sells a much lower SWAP clock, the Microsemi Low Noise Chip-Scale Atomic Clock (LN-CSAC) which has a volume of $< 46$ cm$^3$ and an Allan deviation of $3 \times 10^{-11}$ at 1 s [44]. For comparison, Stanford Research Systems sells a bench top rubidium clock, the FS725, which fits in a half-width 2U chassis and claims an Allan deviation of $2 \times 10^{-11}$ at 1 s [45]. The FS725 and LN-CSAC both operate via rubidium vapor cell spectroscopy. Their performance limits are dictated by the vapor-related systematics. The cesium beam clock's performance is limited mainly by the uncertainty of the second-order Doppler shift.

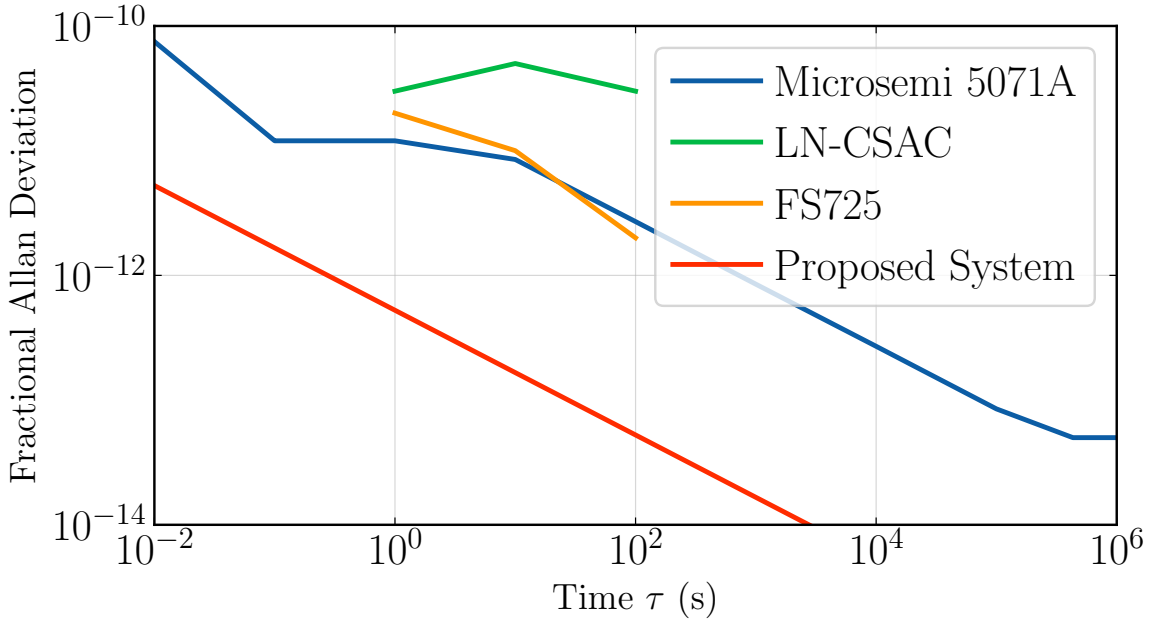


Figure 1.1: Fractional Allan deviation of select low-SWAP atomic clock technology.

There are also efforts to develop a miniature trapped-ion atomic clock in $^{171}Yb^+$ [46, 47]. This buffer gas-cooled clock stabilizes its crystal oscillator to the ground state hyperfine splitting of a trapped $^{171}Yb^+$ cloud. Unfortunately in Paul-style ion traps, inherent trap RF micromotion cannot be nulled for all ions and therefore there is a large second-order Doppler shift. With an average ion temperature of 1000 K in this trap, the ion temperature fluctuations limit the clock performance to greater than $10^{-12}$ [48]. A recent publication

details a space-deployed atomic clock based on a Paul trap which uses a higher order multipole trapping potential to minimize the second-order Doppler shift [49]. All Paul-style traps have uncertainties that suffer from this second-order Doppler shift [40, 50].

## 1.3 Thesis Overview

In this thesis, I describe the development and demonstration of a new kind of Penning trap based on rare earth permanent magnets. With this apparatus I characterize the system, perform Doppler laser cooling, and coherent quantum operations. Although rare earth permanent magnet Penning traps have been created before [51, 52, 53], to the best of our knowledge there have been no published reports of Doppler laser cooling or quantum operations in these devices. This design based on permanent magnets demonstrates a compact reconfigurable trap design versatile for atomic, molecular, and optical (AMO) physics experiments [1].

In chapter 2, I give a background of the electrostatic components of a Penning trap, the Hamiltonian of the trapped ions, as well as a description of the relevant atomic structure of the ions used in this thesis, calcium and beryllium. In chapter 3, I detail the apparatus including the electrode design, magnetic field source, vacuum system, laser systems, and experiment controls. Chapter 4 and chapter 6 describe initial ion trapping of calcium-40 and beryllium, respectively. The two species are trapped separately and co-trapped. Chapter 5 details the characterization of the experiment's spatial and temporal magnetic field variations. Chapter 7 presents the measurements of the nuclear, clock, and microwave transitions in the ground state of beryllium. Lastly, in chapter 7 I give a conclusion to the fate of the beryllium clock and future work.

# CHAPTER 2

# PENNING TRAP THEORY AND ATOMIC SPECIES

In this chapter, I detail the theoretical background for the experiment in this thesis. First, the theory of charged particle motion in a Penning trap is described. Then, I discuss the Hamiltonian for trapped ions including the trap interaction, strong magnetic field, and electromagnetic radiation driving the transitions in the ions. Finally, I review the atomic structure of the two species, calcium-40 and beryllium ions, their relevant transitions, and the functions for the transitions.

## 2.1 Penning Traps

Penning traps rely on static electric and magnetic fields to confine charged particles in 3-dimensional space. A static uniform magnetic field, typically $> 0.5$ T, is used to constrain the particles motion in the radial direction. A static electric quadrupole field (magnitude for stable determined by the magnetic field strength) is used to confine the particles in the vertical direction.

### 2.1.1 Magnetic Trapping Field

The Lorentz force keeps the charged particles trapped in a circular orbit. The force is given by, $\mathbf{F}_L = q\mathbf{v} \times \mathbf{B}$, where $q$ is the particle's charge, $\mathbf{v}$ is the particle's velocity vector, and $\mathbf{B}$ is the magnetic field vector. The frequency of this circular motion can be calculated by equating the Lorentz force to the force due to centripetal acceleration, $qv_\perp B/m = v_\perp^2/r$, and $v_\perp = \omega r$. The variable, $v_\perp$, is the velocity component perpendicular to the magnetic field direction and tangent to the circular motion, $m$ is the particle mass, and $r$ is its radius.

One sees that the rotation rate of the charged particles is

$$\omega_c = qB/m \tag{2.1}$$

where $\omega_c$ is known as the cyclotron frequency. However, this 'bare' cyclotron frequency is not directly measurable in a Penning trap, because the particles are also interacting with the static electric confining potential.

### 2.1.2 Electric Trapping Field

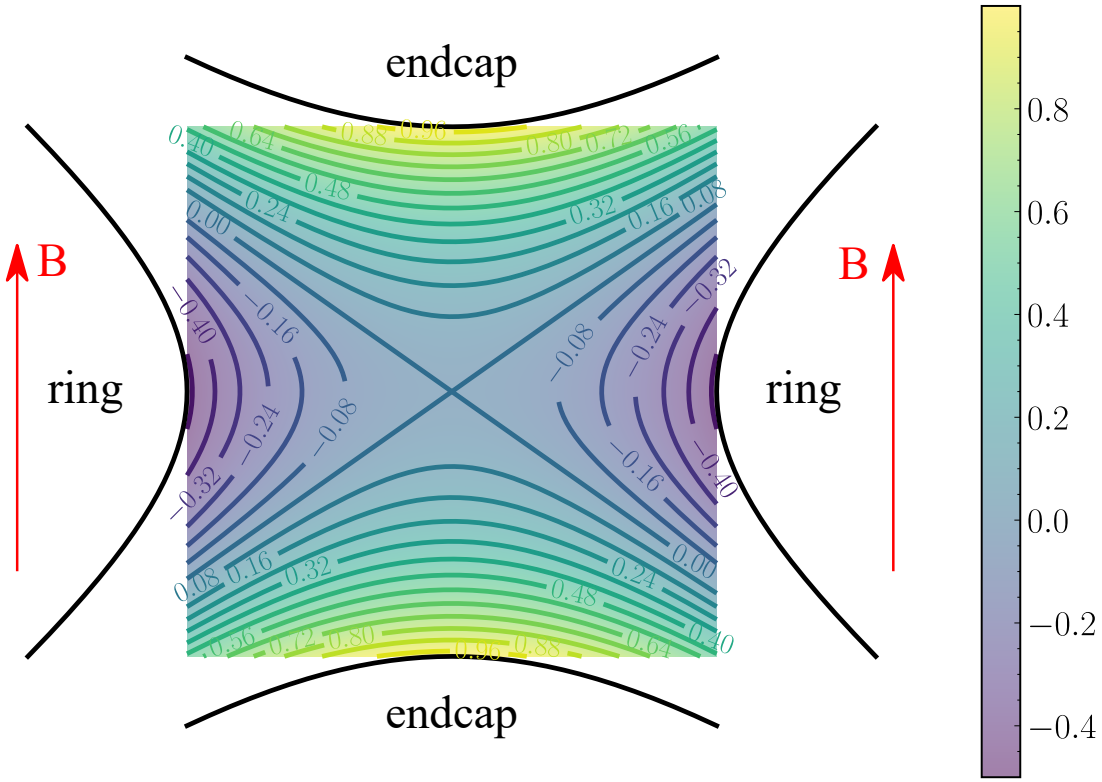


Figure 2.1: A section view through the hyperbolic trap to show the potential between the trap electrodes. The black lines show the boundaries for the endcap and ring electrodes. Contours follow the quadrupole potential lines and are color-coded to match the underlying heat map.

In the axial direction along the magnetic field, the Lorentz force is zero; confinement is achieved instead via a static electric quadrupole field. The quadrupole potential is of the

form

$$\phi = \frac{U_0}{2d_0^2}(2z^2 - \rho^2) \tag{2.2}$$

where $d_0^2 = \frac{1}{2}(\rho_0^2 + 2z_0^2)$, $\rho_0$ is the radius from the center of the trap to the ring electrode, $z_0$ is the distance from the center of the trap to the endcap, $\rho$ is the radial coordinate, $z$ is the vertical coordinate with the origin located at the trap center, and $U_0$ is the potential difference between the ring and endcap electrodes. The potential can be seen in the contour plot of Figure 2.1. The earliest Penning trap designs employed hyperbolic shaped electrodes to create this quadrupole field. This can be seen on the left side of Figure 2.2. These electrode shapes provide the potential boundary that geometrically define a quadrupole field. The electric field is created by applying a potential difference between the ring and endcap electrodes. Small corrections to the field shape are sometimes needed due to imperfections in the electrode shapes or alignments (due to machining tolerances) and are achieved via potentials applied to the compensation electrodes [54].

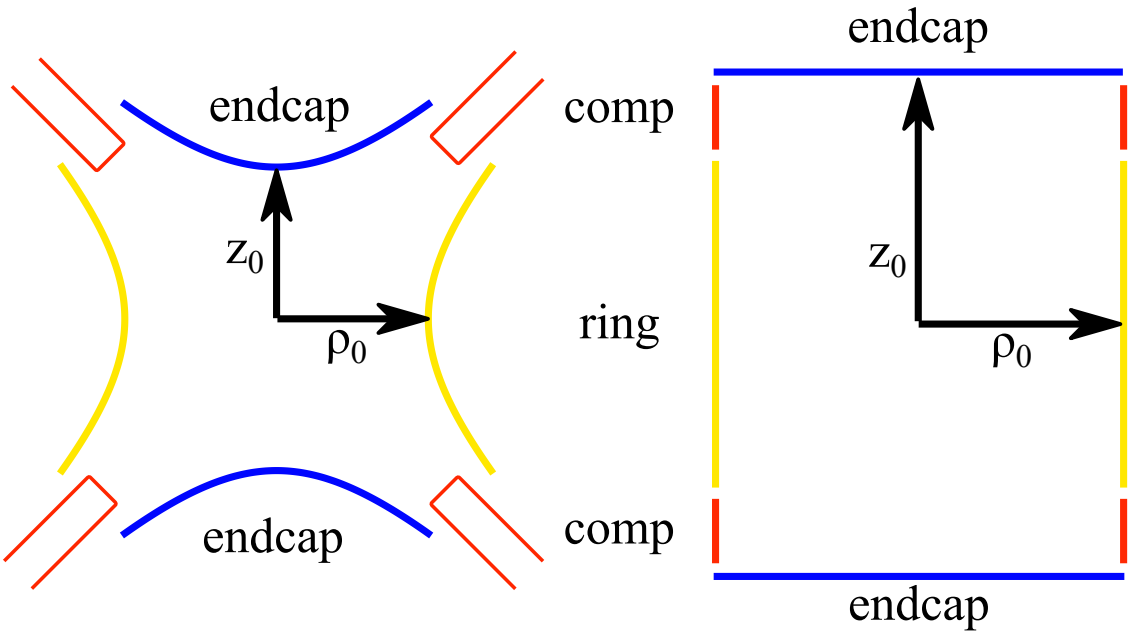


Figure 2.2: Electrode structure on the left is a hyperbolic trap, and the structure on the right is a closed, flat-endcap, cylindrical trap. The electrodes are color coded to guide the eye: the ring electrodes are yellow, the endcap electrodes are blue, and the compensation electrodes are red.

Alternatively, an approximately quadrupole potential can be created using a stack of concentric ring electrodes. An example of this type of trap is shown on the right of Figure 2.2. Fabrication of electrodes in this configuration is much simpler, cheaper, and precise; many modern Penning trap experiments now use this design. By choosing the proper dimensions of the electrodes and proper compensation voltages, one can make the electric fields near the trap center look very similar to the perfect electric quadrupole form achieved by a hyperbolic trap [54].

### 2.1.3 Trapped Particle Motion

With the Lorentz force from the uniform magnetic field and the Coulomb force from the electrode quadrupole potential, we can form a set of equations describing the motion of the trapped particles. If we set the z-direction to be the magnetic field direction, and the radial direction to be in the x-y plane, then the equations of motion are

$$\ddot{x}(t) = \frac{1}{2}\omega_z^2 x + \omega_c \dot{y}(t) \tag{2.3}$$

$$\ddot{y}(t) = \frac{1}{2}\omega_z^2 y - \omega_c \dot{x}(t) \tag{2.4}$$

$$\ddot{z}(t) = -\omega_z^2 z \tag{2.5}$$

The motion in the radial direction can be solved by rewriting the two differential equations into a single differential equation by changing variables. The reparameterization uses the form, $u = x + iy$. The axial direction, z, is a simple differential equation with a known simple harmonic oscillatory solution, where the axial oscillation frequency is

$$\omega_z = \sqrt{\frac{4qU_0}{md_0^2}} \tag{2.6}$$

The solution for the equations of motion, eq. (2.3) , are

$$\begin{aligned} x(t) &= r_- \cos(\omega_- t + \theta_-) + r_+ \cos(\omega_+ t + \theta_+) \\ y(t) &= -r_- \sin(\omega_- t + \theta_-) - r_+ \sin(\omega_+ t + \theta_+) \\ z(t) &= r_z \cos(\omega_z t + \theta_z) \end{aligned} \tag{2.7}$$

where the $r_-$, $r_+$, and $r_z$ are the amplitudes of the oscillatory motion for each mode and $\theta_-$, $\theta_+$, and $\theta_z$ are the initial phases for the motion given by the location of the ions created in the trap.

In the radial direction, the motion is composed of two frequency components,

$$\omega_+ = \frac{1}{2}(\omega_c + \omega_1) \tag{2.8}$$

$$\omega_- = \frac{1}{2}(\omega_c - \omega_1) \tag{2.9}$$

where $\omega_1 \equiv \sqrt{\omega_c^2 - 2\omega_z^2}$. The first Equation 2.8 is commonly referred to as the modified cyclotron frequency[1] (sometimes also referred to as the reduced cyclotron frequency) and the second as the magnetron frequency (sometimes also denoted $\omega_m$).

[1] Some scientists, especially in mass spectrometry, refer to this as the cyclotron frequency, which shouldn't be confused for $\omega_c$, the bare cyclotron frequency.

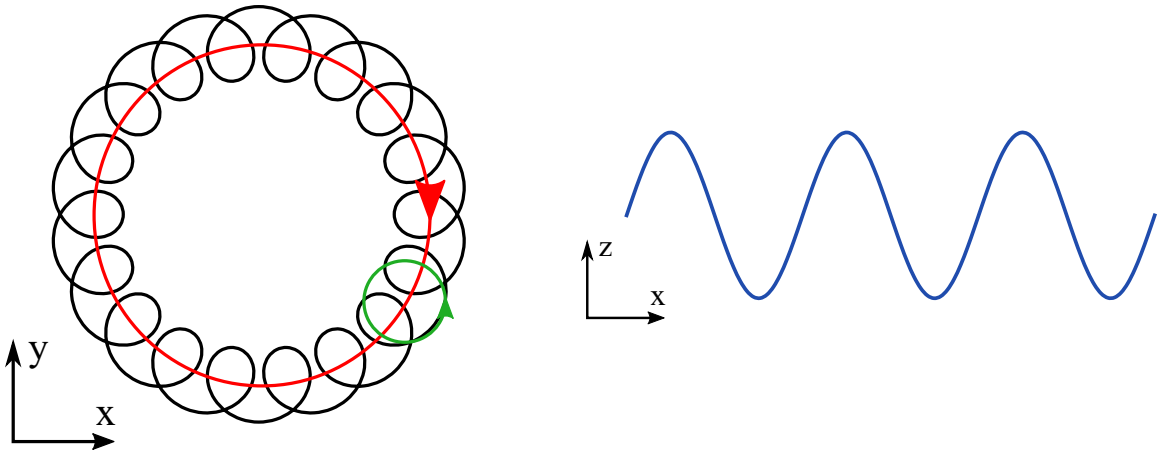


Figure 2.3: Pictures of the radial (left) and axial (right) trajectories of the ions. The radial motion is shown as the black curve and can be decomposed into the two modes represented by red (magnetron) and green curves (modified cyclotron). The axial motion is shown in the blue trace on the right.

In many circumstances, the frequencies follow the relation $\omega_- \ll \omega_z \ll \omega_+ < \omega_c$. Figure 2.3 shows the particle's three frequency components and the collective motion. The trap becomes unstable when the frequency $\omega_1$ becomes imaginary (i.e. the radial confinement disappears). This enforces a stability condition:

$$\omega_c < \sqrt{2}\omega_z \tag{2.10}$$

In other words, the trapping condition is a limit to the maximum possible potential used to confine the ions axially that can be applied to the trap electrodes for a given magnetic field strength. This is simply because the cyclotron frequency is directly proportional to the magnetic field strength and the axial frequency is proportional to the square root of the applied potential. An intuitive way to think about this is that the magnetic field provides the radial confinement; the electric quadrupole potential acts to confine in the axial direction but also deconfines in the radial direction. At the edge of the stability, eq. (2.10) is an equality, the radial deconfining force from the electric trapping potential can no longer be compensated by the Lorentz force.

The equations for the motional frequencies have some fundamental mathematical relations that are useful. One sees that the magnetic field can be calculated from $\omega_+$ and $\omega_-$ through $\omega_c$.

$$\omega_+ + \omega_- = \omega_c \tag{2.11}$$

In addition, the cyclotron frequency (and magnetic field) can be calculated from the measured mode frequencies.

$$\omega_c^2 = \omega_z^2 + \omega_+^2 + \omega_-^2 \tag{2.12}$$

This relation is named the Brown-Gabrielse Invariance Theorem (BGIT) [55]. It can be thought of as a conservation of the motional frequencies. The theorem is invariant to imperfections in the trap magnetic and electric fields, for example, if the magnetic field axis is tilted with respect to the electric field axis [56].

*Trapped Particle Energy*

Using the equations for the particle's position in the trap (eq. (2.7)) and their derivatives, one can calculate the potential and kinetic energies for the trapped particle. For a single particle in a Penning trap, the total energy in the system can be described by eq. (2.13),

$$E = \frac{1}{2}m\left(\omega_z^2 r_z^2 + \frac{1}{2}r_-^2(2\omega_-^2 - \omega_z^2) + \frac{1}{2}r_+^2(2\omega_+^2 - \omega_z^2)\right) \tag{2.13}$$

where $r_+$ is the radius of the modified cyclotron orbit, $r_z$ is the amplitude of the axial oscillation, and $r_-$ is the radius of the magnetron orbit. The first term in eq. (2.13) is the energy due to the harmonic axial motion of the particle. The last two terms are the contributions to the energy from the radial motion, the magnetron and modified cyclotron energies, respectively. The term proportional to the magnetron motion amplitude, $(2\omega_-^2 - \omega_z^2)$, is always negative in sign, while the other two terms are always positive. Thus, the axial and modified cyclotron modes can be cooled by removing energy from the system, but the magnetron mode approaches zero by adding energy to the system [57]. This complicates

laser cooling. A cooling technique must be used that satisfies these requirements, and this will be discussed in chapter 4.

## 2.2 Ion Hamiltonian

For a single atomic ion trapped in a Penning trap, the Hamiltonian is

$$H = H_0 + H_B + H_{trap} + H_L \tag{2.14}$$

where the atom's internal energy structure is encapsulated in $H_0$. The internal energy of the atom is perturbed by the magnetic trapping field described by $H_B$. The energy from the interaction with the trapping fields is given by $H_{trap}$, and the interaction of the Doppler cooling laser is described by the term $H_L$. The methods for calculations in this section can be found in atomic physics textbooks such as [58, 59, 60].

### 2.2.1 Trapping Hamiltonian

A convenient way of describing the electromagnetic fields in the Hamiltonian uses the symmetric gauge with the magnetic vector potential, $\mathbf{A}$. This choice of gauge gives a magnetic vector potential, $\mathbf{A} = B_z(-y/z, x/2, 0)$, for a magnetic field, $\mathbf{B} = (0, 0, B_z)$. Then we can write the form of the trap Hamiltonian with $\mathbf{A}$ and the electric field potential, $\Phi$,

$$H_{trap} = \frac{(\mathbf{p} - q\mathbf{A})^2}{2m} + q\Phi \tag{2.15}$$

where $q$ is the charge of the ion, $m$ is its mass, and $\mathbf{p}$ is the momentum operator. Using the forms for the magnetic vector potential and the electric potential described above, we see that

$$\begin{aligned} H_{trap} &= \frac{p^2}{2m} + \frac{U_0 q}{2d_0^2}(2z^2 - r^2) + \frac{q^2 B_z^2}{2m}(y^2 + x^2) - \frac{qB_z}{2m}(p_y x - p_x y) \\ &= \frac{p^2}{2m} + \frac{m\omega_z^2}{4}(2z^2 - r^2) + \frac{\omega_c^2 m r^2}{8} - \frac{\omega_c L_z}{2} \end{aligned} \tag{2.16}$$

where $L_z$ is the angular momentum of the atom in the z-direction of the trap.

With substitution of the $x$, $y$, $z$, $r$ and their derivatives in eq. (2.16), one arrives at the form for the energy like the equation shown above in eq. (2.13).

$$E_{trap} = \frac{1}{2} m R_z^2 \omega_z^2 + m\omega_1 (R_+^2 \omega_+ - R_-^2 \omega_-) \tag{2.17}$$

The negative term is the contribution from the magnetron motion. As was mentioned earlier, the overall negative sign makes this mode unstable. Loss of energy in the mode results in growth of the ion's radius until it leaves the trapping region. Instead, energy has to be added to the mode to keep the ion stable.

### 2.2.2 Zeeman Effect

Placing an atom in a magnetic field introduces a perturbation to the internal atomic structure. The term $H_B$ in eq. (2.14) describes the effect of the magnetic field. When the field is sufficiently small so that the energy levels splittings are small with respect to the smallest effects in $H_0$, then it can be treated as a perturbation. The perturbation from the magnetic field is

$$H_B = -\mu \cdot \mathbf{B} \tag{2.18}$$

where $\mu$ is the magnetic moment of the atom. The magnetic moment here is the total of the electronic and nuclear moments. The calculations in this section can be found in most atomic physics textbooks such as [58, 59].

*Weak Zeeman Effect, No Hyperfine Structure*

In the even numbered isotopes of calcium, there is no net nuclear magnetic moment so the ion's magnetic moment $\mu$ is described by

$$\mu = \frac{\mu_B g_J \mathbf{J}}{\hbar} = \frac{\mu_B (g_l \mathbf{L} + g_s \mathbf{S})}{\hbar} \tag{2.19}$$

where $\mu_B$ is the Bohr magneton, $\mathbf{J}$ is the total electronic angular momentum, $\hbar$ is reduced Planck's constant, and $g$ is the Lande' g-factor. The total electronic angular momentum, can be broken down into its components of the orbital angular momentum $\mathbf{L}$ and $\mathbf{S}$ and their respective gyromagnetic ratios, $g_l$ and $g_s$. Then, the first order correction to the energy is

$$\begin{aligned} E^{(1)} &= \left\langle n^{(0)} \right| \mu \cdot \mathbf{B} \left| n^{(0)} \right\rangle \\ &= \frac{\mu_B B_z}{\hbar} \left\langle n^{(0)} \right| g_J \mathbf{J} \left| n^{(0)} \right\rangle = \mu_B g_J B_z m_J \end{aligned} \tag{2.20}$$

where $m_J$ is the projection of the total electronic angular momentum in the z-direction. The braket states, $\left|n^(0)\right\rangle$ are the unperturbed energy level states. The second order correction to the energy is

$$E^{(2)} = \sum_{m \neq n} \frac{\mu_B^2 B_z^2 \left| \left\langle m^{(0)} \right| g_J J_z \left| n^{(0)} \right\rangle \right|^2}{\hbar^2 (E_n^{(0)} - E_m^{(0)})} \tag{2.21}$$

*Strong Zeeman Effect with Hyperfine Structure*

An ion with nonzero nuclear magnetic moment, such as the odd numbered isotopes of calcium or beryllium[2], has additional interactions that must be considered. The effect of the interaction of the nuclear spin with the electron spin is called the hyperfine structure. The magnetic fields used in a Penning trap are strong enough to produce Zeeman shifts of similar or far greater magnitude than the shifts due to hyperfine coupling- in some cases, the shifts can even be comparable to the fine structure splitting. Thus, the Zeeman effect cannot simply be treated as a perturbation to the atomic structure. Instead, a Hamiltonian must be constructed that includes all effects of that magnitude. Then, it can be diagonalized to solve for the energy shifts to the levels and the proper eigenvectors. The Hamiltonian

[2]Beryllium only has a single stable, naturally occurring isotope with mass $\sim 9$ amu.

takes the form of

$$\begin{aligned} H &= H_{HFS} + H_B \\ &= \hbar A_{HFS}\mathbf{I}\cdot\mathbf{J} + \hbar B_{HFS}\frac{3(\mathbf{I}\cdot\mathbf{J})^2 + 3/2(\mathbf{I}\cdot\mathbf{J}) - I(I+1)J(J+1)}{2I(2I-1)J(2J-1)} - \mu\cdot\mathbf{B} \\ &= \hbar A_{HFS}\mathbf{I}\cdot\mathbf{J} + \hbar B_{HFS}\frac{3(\mathbf{I}\cdot\mathbf{J})^2 + 3/2(\mathbf{I}\cdot\mathbf{J}) - I(I+1)J(J+1)}{2I(2I-1)J(2J-1)} \\ &\quad - (\mu_B g_J\mathbf{J} + \mu_N g_I\mathbf{I})\cdot\mathbf{B} \end{aligned} \tag{2.22}$$

where $\mu_N$ is the nuclear magneton, $g_I$ is the nuclear g-factor, and $\mathbf{I}$ is the vector nuclear magnetic moment. The first term of the equation is proportional to $A_{HFS}$, electric dipole hyperfine constant. The second term is proportional to the electric quadrupole hyperfine constant, $B_{HFS}$. This hyperfine constant is nonzero for states that have $J > 1/2$ and $I > 1/2$. The last term is a sum of the interactions of the total electronic angular momentum and the nuclear angular momentum with the magnetic field.

**Hyperfine Structure Terms**

The dot product in the hyperfine structure terms can be expanded in terms of the vector components, $\mathbf{I}\cdot\mathbf{J} = I_xJ_x + I_yJ_y + I_zJ_z$. The x-y terms can be rewritten in terms of raising and lowering operators for each spin operator from the relation, $L_\pm = L_x \pm iL_y$. Using a basis set of states that have known eigenvalues with the given operators, one can compose expressions for the values of the matrix elements of the Hamiltonian due to the electric quadrupole hyperfine interaction.

$$H_{HFS-E1} = \hbar A\mathbf{I}\cdot\mathbf{J} = \hbar A I_zJ_z + \hbar A/2(J_+I_- + J_-I_+) \tag{2.23}$$

This expansion of $\mathbf{I}\cdot\mathbf{J}$ can be similarly used for the electric quadrupole term.

At low field, $F$ and $m_F$ are good quantum numbers, however, at high field, $m_F$, $m_I$ and thus $m_J$ are good quantum numbers. States of different $F$ and like $m_F$ are coupled by the magnetic field as it increases. The high field regime is closest to the fields used in

a Penning trap so those are the quantum numbers best used to span the eigenvector space. Depending on the field strength, however, these quantum numbers are not perfect. The calculated eigenvectors when diagonalizing the Hamiltonian will contain small mixtures of other states ($< 10^{-2}$). The terms in the mixture will be the states that correspond to the same quantum number, $m_F$. Using the high field regime states as eigenvectors, the matrix entries for the electric dipole hyperfine structure Hamiltonian terms are then,

$$\begin{aligned}\langle H_{HFS-E1}\rangle = &\frac{\hbar A}{2}\sqrt{(I+m_I)(I-m_I+1)}\sqrt{(J-m_J)(J+m_J+1)}\delta_{m'_J,m_J+1}\delta_{m'_I,m_I-1}\\ &+\frac{\hbar A}{2}\sqrt{(I-m_I)(I+m_I+1)}\sqrt{(J+m_J)(J-m_J+1)}\delta_{m'_J,m_J-1}\delta_{m'_I,m_I+1}\\ &+\hbar A m_I m_J \delta_{m'_J,m_J}\delta_{m'_I,m_I}\end{aligned} \tag{2.24}$$

where this form is obtained by using the general form for the angular momentum raising and lowering operators, $L_\pm |L, m_L\rangle = \sqrt{(L \mp m_L)(L \pm m_L + 1)}\, |L, m_L \pm 1\rangle$. This procedure is the same for calculating the electric quadrupole hyperfine terms. A full diagonalizion of the Hamiltonian matrix should include these terms for highest accuracy.

**External Magnetic Field Terms**

The last two terms of the Zeeman effect Hamiltonian will be of similar structure to Equation 2.20,

$$H_B = -(\mu_B g_J \mathbf{J} + \mu_N g_I \mathbf{I}) \cdot \mathbf{B}\ . \tag{2.25}$$

The magnetic field vector, $\mathbf{B}$, only has a component in the z-direction. Thus, the dot product selects the projection of the magnetic momentum vectors in the z-direction. The interaction of each spin with the magnetic field gives a contribution to the Hamiltonian matrix elements

$$\langle H_B\rangle = -(\mu_B g_J B_z m_J \delta_{m'_J,m_J} + \mu_N g_I B_z m_I \delta_{m'_I,m_I})\ . \tag{2.26}$$

All the Hamiltonian terms of similar strength are combined into a single matrix. It is

then diagonalized to obtain the eigenvectors and their corresponding energies.

### 2.2.3 Two State Internal Hamiltonian

If one considers a free ion with only two electronic states, the internal Hamiltonian can be described by

$$H_0 = \frac{\hbar\omega_0}{2}\left|e\right\rangle\left\langle e\right| - \frac{\hbar\omega_0}{2}\left|g\right\rangle\left\langle g\right| = -\frac{\hbar\omega_0}{2}\sigma_z \tag{2.27}$$

where $\sigma_z$ is the Pauli-z operator, $\hbar\omega_0$ is the energy between the ground, $|g\rangle$, and excited, $|e\rangle$, states, and the zero-point energy is taken to be halfway between the ground and excited states.

### 2.2.4 Electromagnetic Plane Wave Interaction with an Atom

Like the trap Hamiltonian was parametrized above, the same can be done with the interaction for a charged particle with electromagnetic radiation [59].

$$H_L = \frac{(\mathbf{p} - q\mathbf{A})^2}{2m} = \frac{\mathbf{p}^2}{2m} - \frac{q}{2m}(\mathbf{p}\cdot\mathbf{A} + \mathbf{A}\cdot\mathbf{p}) + \frac{q^2\mathbf{A}^2}{2m} \tag{2.28}$$

But the operator $\mathbf{p} = -i\hbar\nabla$ and the Coulomb gauge condition $\nabla\cdot\mathbf{A} = 0$, then the Hamiltonian is

$$H_L = \frac{\mathbf{p}^2}{2m} - \frac{q}{2m}(\mathbf{A}\cdot\mathbf{p}) + \frac{q^2\mathbf{A}^2}{2m} \tag{2.29}$$

The first term is the kinetic energy term which is not a part of the radiation interaction and the third term is the diamagnetic term which is small for weak electromagnetic intensities. In the Coulomb gauge condition and using $\mathbf{E} = -\frac{\partial\mathbf{A}}{\partial t}$, the form for a electromagnetic plane wave is

$$\mathbf{A} = \frac{\hat{\epsilon}_\mathbf{L}E_0}{2i\omega_L}\left(e^{i(\mathbf{k}_L\cdot\mathbf{r}-\omega_L t)} + e^{-i(\mathbf{k}_L\cdot\mathbf{r}-\omega_L t)}\right) \tag{2.30}$$

where $\hat{\epsilon}_L$ is the wave polarization direction, $E_0$ is the electric field strength, $\omega_L$ is the angular frequency of the wave, $\mathbf{k}_L$ is the wavevector, $\mathbf{r}$ is the position, and $t$ is the time.

The vector potential can be Taylor expanded in $e^{i\mathbf{k}_L\cdot\mathbf{r}}$ and substituted into the Hamiltonian

$$H_L = -\frac{qE_0}{4im\omega_L}(\hat{\epsilon_0}\cdot\mathbf{p})((1+i\mathbf{k_L}\cdot\mathbf{r}+h.o.)e^{-i\omega_L t}+H.c.) \tag{2.31}$$

The first term in the Taylor series is the electric dipole term, whereas, the second gives rise to the electric quadrupole and magnetic dipole terms.

*Electric Dipole Interaction (E1)*

Consider a perfect, monochromatic laser that has an electric field,

$$\mathbf{E}(t) = \frac{\hat{\epsilon}_\mathbf{L}E_0}{2}\left(e^{i(\mathbf{k}_L\cdot\mathbf{r}-\omega_L t)}+e^{-i(\mathbf{k}_L\cdot\mathbf{r}-\omega_L t)}\right) \tag{2.32}$$

where $\hat{\epsilon_\mathbf{L}}$ is the polarization unit vector, $E_0$ is the electric field amplitude, $\mathbf{k}$ is the wavevector, and $\mathbf{r}$ is the position vector. If we expand the exponent in the wave vector dot product using the Taylor expansion, we get that $e^{i\mathbf{k}_L\cdot\mathbf{r}} = 1+i\mathbf{k}_L\cdot\mathbf{r}-(\mathbf{k}_L\cdot\mathbf{r})^2/2+....$ The electric field can be rewritten

$$\mathbf{E}(t) = \frac{\hat{\epsilon}_\mathbf{L}E_0}{2}\left((1+i\mathbf{k}_L\cdot\mathbf{r}-(\mathbf{k}_L\cdot\mathbf{r})^2/2)e^{-i\omega_L t}+H.c.\right) \tag{2.33}$$

if we truncate the series at the second order term. In the small argument limit, $e^{i\mathbf{k}_L\cdot\mathbf{r}}\approx 1$, we have what is known as the dipole approximation. This approximation is only valid for small values of $\mathbf{k}_L\cdot\mathbf{r}$. Physically, this means that the spatial extent of $\mathbf{r}$ should be small with respect to the laser electric field spatial extent. In the dipole approximation, our electric field equation can be rewritten as

$$\mathbf{E}(t) = \frac{\hat{\epsilon}_L E_0}{2}\left(e^{-i\omega_L t}+e^{i\omega_L t}\right)\ . \tag{2.34}$$

The energy from this electric field interaction with the ion can be written from the interaction of the field with the ion's electric multipole moment. Using the ion's electric

dipole moment, the energy for the laser interaction can be written as $-e\mathbf{r}\cdot\mathbf{E}$. Alternatively, the electromagnetic fields from the monochromatic light can be rewritten with the magnetic vector potential using the Coulomb gauge, as shown in the beginning of the section. With radiation near that of the energy level spacing, the Hamiltonian is

$$H_{laser} = \frac{eE_0}{2}\hat{\epsilon}_L \cdot \mathbf{r}(e^{-i\omega_L t} + e^{i\omega_L t}) = \frac{\hbar\Omega_0}{2}(\sigma_+ + \sigma_-)(e^{-i\omega_L t} + e^{i\omega_L t}) \tag{2.35}$$

where $\Omega_0 = eE_0 \langle e| \hat{\epsilon}_L \cdot \mathbf{r} |g\rangle$ is defined as the rabi rate of the electric dipole transition, and $a^\dagger$ and $a$ are the raising and lowering operators.

We can now shift into the interaction picture using the transformation $H_{int} = U_0^\dagger H_{laser} U_0$, where $U_0 = e^{-i/\hbar H_0' t}$ and $H_0' = H_0 + H_B + H_{trap}$ is the ion's internal Hamiltonian including the electronic structure, the perturbing magnetic field, and the atom motion. If we are interacting with a stationary ion, then $H_0' = H_0 + H_B$. The form for the interaction Hamiltonian can be simplified using the rotating wave approximation. This removes the terms oscillating at $\omega_0 + \omega_L$ which is much faster than any of the other relevant dynamics. Finally, the interaction is

$$H_{int}(t) = \frac{\hbar}{2}\Omega_0(\sigma_+ e^{-i\delta t} + \sigma_- e^{i\delta t}) \tag{2.36}$$

where $\delta$ is a frequency detuning $\delta = \omega_L - \omega_0$.

Now this can be used with the Schrodinger equation

$$i\hbar\frac{\partial}{\partial t}|\Psi(t)_{int}\rangle = H_{int}(t)|\Psi(t)_{int}\rangle \tag{2.37}$$

to find the evolution of the states. We start with the state $|\Psi(t)_{int}\rangle = c_g|g\rangle + c_e|e\rangle$, where the $|g\rangle$ and $|e\rangle$ are already transformed into the interaction picture. The state amplitudes

then are

$$\begin{aligned}\dot{c}_g(t) &= \frac{i\Omega_0}{2}e^{i\delta t}c_e(t) \\ \dot{c}_e(t) &= -\frac{i\Omega_0}{2}e^{-i\delta t}c_g(t)\end{aligned} \tag{2.38}$$

For an initial condition where all the population starts in the ground state, $|c_g(0)|^2 = 1$ and $|c_e(0)|^2 = 0$, the differential equations can be solved analytically. The populations will follow the form

$$\begin{aligned}|c_g(t)|^2 &= \frac{\Omega_0^2}{\Omega^2}\cos^2(\frac{\Omega t}{2}) \\ |c_e(t)|^2 &= \frac{\Omega_0^2}{\Omega^2}\sin^2(\frac{\Omega t}{2})\end{aligned} \tag{2.39}$$

where $\Omega^2 = \Omega_0^2 + \delta_L^2$ is the effective rabi frequency or rabi rate. This shows that detuning from the transition resonance, $\omega_0$ will increase the oscillation frequency but will decrease the amplitude of the oscillations. An oscillation between the two states is known as a Rabi flop and the time needed to swap the populations of the states is referred to as the pi time. The electromagnetic pulse with a given power and duration calibrated to perform a population swap is known as a pi pulse. The pi pulse time is defined as $t_\pi = \pi/\Omega$.

*Electric Quadrupole Interaction (E2)*

The second term of the Taylor expansion inside the laser interaction Hamiltonian, Equation 2.31,

$$\frac{-qE_0}{4m\omega_L}(\hat{\epsilon_0}\cdot\mathbf{p})(\mathbf{k}_L\cdot\mathbf{r})[e^{-i\omega_L t} - e^{i\omega_L t}], \tag{2.40}$$

gives higher order interactions. If the matrix elements for an electric dipole transition are zero, then the transition is denoted electric dipole forbidden. However, transitions between these states can still happen with a higher order interaction. The matrix elements of the Hamiltonian can be rewritten between the ground and excited states for a transition. The

operators can be further separated into two terms,

$$\begin{aligned}\langle e|\,(\hat{\epsilon_0}\cdot\mathbf{p})(\mathbf{k}_L\cdot\mathbf{r})\,|g\rangle &= \frac{1}{2}\langle e|\,(\hat{\epsilon_0}\cdot\mathbf{p})(\mathbf{k}_L\cdot\mathbf{r})+(\mathbf{k}\cdot\mathbf{p})(\hat{\epsilon_0}\cdot\mathbf{r})\,|g\rangle \\ &+\frac{1}{2}\langle e|\,(\hat{\epsilon_0}\cdot\mathbf{p})(\mathbf{k}_L\cdot\mathbf{r})-(\mathbf{k}\cdot\mathbf{p})(\hat{\epsilon_0}\cdot\mathbf{r})\,|g\rangle\,.\end{aligned} \tag{2.41}$$

The first term gives the electric quadrupole transition. It can also be rewritten as

$$\frac{1}{2}\mathbf{k_L}\cdot\langle e|\,\mathbf{rp}+\mathbf{pr}\,|g\rangle\cdot\hat{\epsilon_0} = \frac{-im\omega_0}{2}\mathbf{k_L}\cdot\langle e|\,\mathbf{rr}\,|g\rangle\cdot\hat{\epsilon_0} \tag{2.42}$$

because of the anti-commutator relation, $\{\mathbf{r},\mathbf{p}\}=\frac{im}{\hbar}[H_0,\mathbf{rr}]$. So the E2 transition matrix element can be written as

$$\begin{aligned}\langle e|\,H_L^{E2}\,|g\rangle &= -\frac{iqE_0\omega_0}{8c}[\hat{\mathbf{k}}_\mathbf{L}\cdot\langle e|\,\mathbf{rr}\,|g\rangle\cdot\hat{\epsilon_0}](e^{i\omega_L t}-e^{-i\omega_L t}) \\ &= \frac{qE_0\omega_0}{4c}[\hat{\mathbf{k}}_\mathbf{L}\cdot\langle e|\,\mathbf{rr}\,|g\rangle\cdot\hat{\epsilon_0}]\sin(\omega_L t)\end{aligned}$$

where $\mathbf{k_L}=\hat{\mathbf{k}}_\mathbf{L}\omega_L/c$ and $c$ is the speed of light in vacuum.

*Magnetic Dipole Interaction (M1)*

The second term of Equation 2.41 contributes to the magnetic dipole interaction in addition to the electron's spin interaction with the magnetic field. The matrix element is

$$\langle e|\,H_L^{M1}\,|g\rangle = \frac{-qE_0}{8m\omega_L}[e^{-i\omega_L t}-e^{i\omega_L t}]\,\langle e|\,(\hat{\epsilon_0}\cdot\mathbf{p})(\mathbf{k}_L\cdot\mathbf{r})-(\mathbf{k_L}\cdot\mathbf{p})(\hat{\epsilon_0}\cdot\mathbf{r})\,|g\rangle-\langle e|\,\mu\cdot\mathbf{B}\,|g\rangle \tag{2.43}$$

The first term can be rewritten using the Binet-Cauchy Identity in three dimensions, $(A\times B)\cdot(C\times D)=(A\cdot C)(B\cdot D)-(A\cdot D)(B\cdot C)$. Then the Hamiltonian is

$$\langle e|\,H_L^{M1}\,|g\rangle = \frac{-qE_0}{8mc}[e^{-i\omega_L t}-e^{i\omega_L t}](\hat{\mathbf{k}}_\mathbf{L}\times\hat{\epsilon}_0)\cdot\langle e|\,\mathbf{r}\times\mathbf{p}\,|g\rangle-\langle e|\,\mu\cdot\mathbf{B}\,|g\rangle \tag{2.44}$$

Given a monochromatic plane wave, the cross product, $\hat{\mathbf{k}}_\mathbf{L} \times \hat{\epsilon}_0$, is just the radiation magnetic field direction. The other cross product, $\mathbf{r} \times \mathbf{p}$, is the orbital angular momentum operator, $\mathbf{L}$. The second term of the Hamiltonian is the magnetic dipole moment is $\mu = \mu_B(g_s\mathbf{S} + g_L\mathbf{L})/\hbar = \mu_B g_J \mathbf{J}/\hbar$ interacting with the field from the radiation. The Hamiltonian is then

$$\langle e| H_L^{M1} |g\rangle = \frac{qE_0}{8mc}[e^{i\omega_L t} - e^{-i\omega_L t}]\hat{\mathbf{B}} \cdot \langle e| \mathbf{L} |g\rangle - \frac{\mu_B g_J}{\hbar} \langle e| \mathbf{J} \cdot \mathbf{B} |g\rangle \tag{2.45}$$

*Interaction Hamiltonian Including Motion*

Using the internal Hamiltonian $H_0'$, which includes ion motion, the resultant laser interaction can be simplified using the rotating wave approximation and introducing the Lamb-Dicke parameter, $\eta = k\sqrt{\hbar/(2m\nu_m)}$. The Lamb-Dicke parameter is defined as product of the wavenumber of the light interacting with the ion, $k$, and the size of the ground state wave function, $z_0 = \sqrt{\hbar/(2m\nu_m)}$, where $\nu_m$ is the mode motional frequency. The interaction Hamiltonian then becomes,

$$H_{int}(t) = \frac{\hbar}{2}\Omega_0(\sigma_+ e^{-i\delta t} e^{i\eta[ae^{i\nu_m t} + a^\dagger e^{-i\nu_m t}]} + H.c.) \tag{2.46}$$

where $H.c.$ stands for Hermitian conjugate. The rotating wave approximation removes the terms which oscillate much faster than the dynamics of the rest of the system. The terms with the Lamb-Dicke parameter can be expanded as well, $e^{i\eta[ae^{i\nu_m t} + a^\dagger e^{-i\nu_m t}]} = 1 + \eta(a_{int} + a_{int}^\dagger) + ...$, where $a_{int} = ae^{i\nu_m t}$. For small values of the parameter, $\eta$, the series can be truncated and the interaction dynamics are referred to as being in the 'Lamb-Dicke regime'. In this regime,

$$H_{int}(t) = \frac{\hbar}{2}\Omega_0(\sigma_+ e^{-i\delta t}(1 + \eta(a_{int} + a_{int}^\dagger)) + H.c.) \tag{2.47}$$

For the work in this thesis, the microwave and nuclear spin flip transitions have very long wavelengths compared to the size of the ground state wavefunction, thus $\eta \sim 0$. Therefore, the dynamics are similar to the interactions with a stationary ion, as shown above.

## 2.3 Calcium-40

Calcium-40 is a common element used for ion trapping experiments. It has a compromise of features that make it convenient in atomic physics laboratories. It is the most abundant naturally occurring form of calcium on Earth with an abundance of $96.941\%$ and a mass of $39.962591$ amu [61]. Its nucleus has no magnetic moment, so it has no hyperfine structure. It has a relatively low mass compared to the other possible trapped ions on the periodic table, while still being heavier than beryllium. This allows for larger motional frequencies than for other heavier ion species. Calcium's lowest lying levels are well-spaced to allow for Doppler cooling, because the required laser frequencies are all achievable by direct diode lasers.

### 2.3.1 Calcium Neutral Atomic Structure

Neutral calcium-40 has a simple atomic structure for ionization that is shown in Figure 2.4. The atoms have an electric dipole transition from the $^1S_0$ state to the $^1P_1$ state. This transition has a wavelength of $\sim 423$ nm ($709.07837301(35)$ THz) and a linewidth of $\sim 35$ MHz [62]. However, the $^1P_1$ state splits into three levels when in a magnetic field due to the Zeeman effect. Two components have net magnetic moment projections of opposite sign, $m_J = \pm 1$ and a third component has no net magnetic moment, $m_J = 0$. Thus, there is a magnetic field insensitive transition and two field sensitive ones.

One way to ionize calcium atoms is to use a two photon resonant ionization method [63]. In this method, the first photon excites the electron to the $^1P_1$ state and then another photon of wavelength shorter than 389 nm excites the electron to the continuum. The isotopic shifts of the calcium isotopes are much greater than the linewidth of the transition,

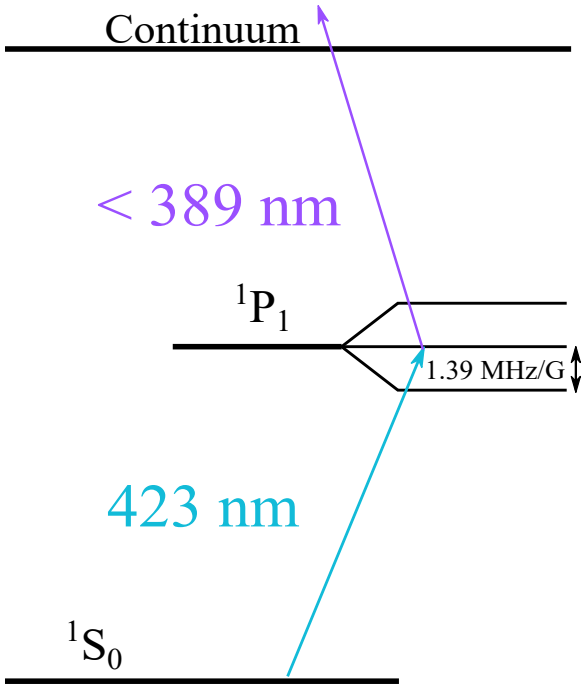


Figure 2.4: A diagram of the lowest energy levels used for ionization in $^{40}$Ca neutral atoms.

so this ionization process is naturally isotopically selective [63].

### 2.3.2 Calcium ions

The calcium-40 ion has a relatively simple atomic structure. The main low lying levels used in calcium are its ground state, $^2S_{1/2}$, two P-levels commonly used for Doppler cooling, $^2P_{1/2}$ and $^2P_{3/2}$, and two lower-lying metastable D-levels, $^2D_{3/2}$ and $^2D_{5/2}$. Figure 2.5 shows the relevant transitions and the wavelengths of the radiation needed to address a transition between them. Table 2.1 shows each of the transition frequencies at zero magnetic field, the corresponding branching ratios, and the Einstein A coefficients. Table 2.1 shows each state's lifetime, 1st and 2nd order magnetic field sensitivities. With the magnetic field required for a Penning trap, the calcium ions' levels are split by several GHz due to the Zeeman effect. With these splittings, even more lasers are required for Doppler cooling.

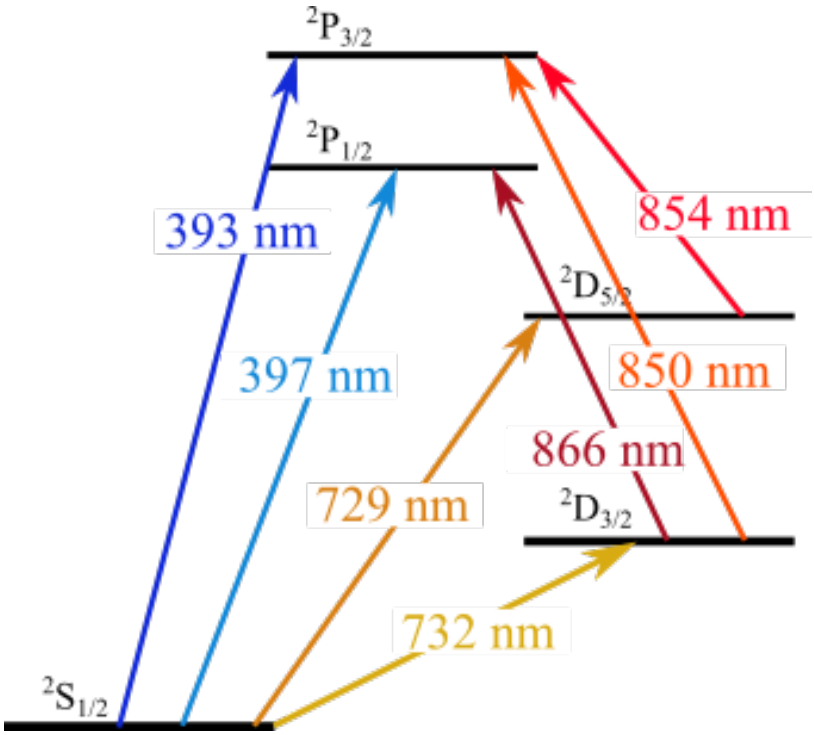


Figure 2.5: A diagram of the fine structure energy levels used in calcium ions and all possible transitions.

Table 2.1: For each of the lowest lying transitions commonly used in $^{40}Ca^{+}$: the frequency of the transitions in vacuum (0 G), the branching ratios, and $A_{12}$ coefficients are tabulated.

| Transitions | | | |
|---|---|---|---|
| Transition | Frequency at 0 G (MHz) | Branching Ratios | $A_{12}$ Coefficient |
| 393 nm | 761905012.606(91) [64] | 0.9347(3) [65] | 1.47e8 [66] |
| 397 nm | 755222765.896(88) [67] | 0.93565(7) [68] | 1.4e8 [66] |
| 729 nm | 411042129.776393 [69] | - | 0.856(5) [70] |
| 732 nm | 409222530.754868(8) [71] | - | 0.837(6) [72] |
| 850 nm | 352682481.844(82) [71] | 0.00661(4) [65] | 1.11e6 [66] |
| 854 nm | 350862882.823(82) [71] | 0.0587(2) [65] | 9.9e6 [66] |
| 866 nm | 346000234.867(96) [73] | 0.06435(7) [68] | 1.06e7 [66] |

Table 2.2: For calcium-40: The B-field sensitivity of the $S_{1/2}$ state is calculated using the best measured value for the Lande g-factor for the state, $g_J = 2.00225664(9)$[74]. The first order B-field sensitivity for the $D_{5/2}$ state is calculated using the best measure of the Lande g-factor of that state, $g_J = 1.2003340(3)$ [69]. The values without a reference were calculated instead of measured.

| Levels List | | | |
|---|---|---|---|
| Level | Lifetime | B-Field Sensitivity (MHz/G) | 2nd Order B-Field Sensitivity (MHz/G$^2$) |
| $^2S_{1/2}$ | - | 2.8024074(1) [74] | 0 |
| $^2P_{1/2}$ | 6.924(19) ns [75] | 0.9320 | 0 |
| $^2P_{3/2}$ | 7.098(20) ns [75] | 1.8672 | 6.51 ($m_J = \frac{1}{2}$) |
| $^2D_{3/2}$ | 1.195(8) s [72] | 1.1190 | -25.8 ($m_J = \frac{1}{2}$), -17.2 ($m_J = \frac{3}{2}$) |
| $^2D_{5/2}$ | 1.168(7) s [70] | 1.6800169(4) [69] | 25.8 ($m_J = \frac{1}{2}$), 17.2 ($m_J = \frac{3}{2}$) |

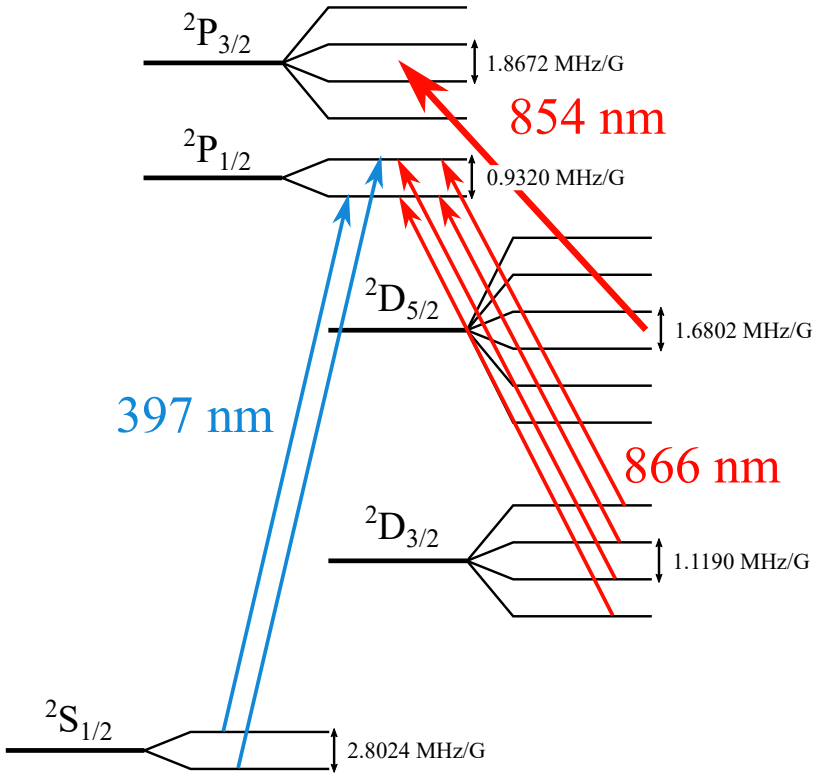


Figure 2.6: A diagram of the energy levels used in calcium ions and our 397 nm Doppler cooling scheme.

*397 nm Doppler Cooling*

The $^2S_{1/2}$ to $^2P_{1/2}$ at 397 nm is the commonly used transition for Doppler cooling due to its fast decay time. However, the $^2P_{1/2}$ state has a probability of decaying to the metastable $^2D_{3/2}$ state. Most of the transitions made to the $^2P_{1/2}$ state will return to the $^2S_{1/2}$ ground state, but $6.435(7)\%$ [68] will decay to the $^2D_{3/2}$ state. Thus, a resonant 866 nm laser is needed to repump the electron back to the $^2P_{1/2}$ so that it can return to the fast cycling transition. At our magnetic field, Doppler cooling requires two 397 nm lasers, four 866 nm repump laser tones, and an 854 nm laser. The 854 nm laser is necessary due to j-mixing. This Doppler cooling configuration is shown in Figure 2.6.

*J-mixing*

In a very strong magnetic field, the 'good' quantum numbers describing the fine structure begin to break down. This effect is observed in typical Penning traps with magnetic fields $> 1$ T. In this regime, states with the same total angular momentum projection, $m_J$, begin to get mixed between levels with the same L and $m_J$ numbers. This effect is termed 'j-mixing'.

With only the 397 nm and 866 nm lasers at low field, the transitions form a closed group due to selection rules. At our field, we see some ions end up shelved in the $^2D_{5/2}$ level. This is because of a small mixing of the $^2P_{3/2}$ with the $^2P_{1/2}$ [76]. Thus, there is a small probability of the electron decaying into the normally forbidden $^2D_{5/2}$ states. During continuous Doppler cooling, the best results are achieved with an 854 nm laser to deshelve the metastable state.

The magnitude of the mixed states can be directly calculated. The magnetic field does the mixing, so we need to calculate the matrix with elements described by the magnetic dipole interaction,

$$-\langle J', m_J'| \mu \cdot \mathbf{B} |J, m_J\rangle \tag{2.48}$$

for the 6 states making up the $^2P_{1/2}$ and $^2P_{3/2}$ manifolds, where $J$ and $J'$ are the total angular momentum numbers, and $m_J$ and $m'_J$ are the z-projections of the total angular moment. The magnetic moment is $\mu = \mu_B g_J \vec{\mathbf{J}}/\hbar$, where $g_J$ is the Lande g-factor, $\mu_B$ is the Bohr magneton, and $\vec{\mathbf{J}}$ is the total angular momentum operator. If the magnetic field in the trap is $\mathbf{B} = (0, 0, B)$, then the dot product only takes the z-component. However, $\mathbf{J}$ is no longer a good quantum number; we need to break the interaction into the uncoupled basis, $\mu = -\mu_B(g_S\mathbf{S} + g_L\mathbf{L})/\hbar$. The terms $\mathbf{S}$ and $\mathbf{L}$ are the forms for the spin and orbital angular momentum operators, respectively. Then the matrix elements are now

$$\frac{B\mu_B}{\hbar} \langle J', m'_J | \, g_S S_z + g_L L_z \, | J, m_J \rangle \tag{2.49}$$

where we only need the z-components of the operators from the dot product. The states need also to be rewritten in terms of the uncoupled basis using the formula

$$|J, m_J\rangle = \sum_{m_S, m_L} (-1)^{L-S+m_J} \sqrt{2J+1} \begin{pmatrix} L & S & J \\ m_L & m_S & -m_J \end{pmatrix} |L, m_L, S, m_s\rangle \tag{2.50}$$

where the matrix in parentheses is a Wigner 3-j symbol and the sum is over all possible spin and orbital angular momentum z-projection numbers, $m_S$ and $m_L$. By moving to the uncoupled basis by substituting Equation 2.50 for both the bra and ket of the matrix element, Equation 2.49, the operators can directly act on the transformed basis states. The matrix element is then

$$\begin{aligned} \langle -\mu \cdot \mathbf{B} \rangle = \frac{\mu_B B}{\hbar} \sum_{m'_s m'_L} \sum_{m_S m_L} (-1)^{L'+L-S'-S+m'_J+m_J} \sqrt{2J'+1}\sqrt{2J+1} \\ \begin{pmatrix} L' & S' & J' \\ m'_L & m'_S & -m'_J \end{pmatrix} \begin{pmatrix} L & S & J \\ m_L & m_S & -m_J \end{pmatrix} \delta_{L'L}\delta_{S'S}\delta_{m'_L m_L}\delta_{m'_S m_S}(g_S m_S + g_L m_L) \end{aligned} \tag{2.51}$$

A full 6x6 matrix can be generated from the form for the matrix element. Each term

describes the coupling between the each of the $^{40}Ca^{+}$ P-states. In order to find the amount of state mixing, the energy for the fine strtucture splitting also needs to be included in the calculation. This can be done by simply adding the energy to the matrix's diagonal terms cooresponding to the $P_{3/2}$ states.

However, generating the full 6x6 matrix is not necessary here. Because each state in the $P_{1/2}$ only couples to one state in the $P_{3/2}$, there are effectively two uncoupled, two-level systems that can be solved analytically. The two systems should result in the same mixing amount for Zeeman splittings small compared to the fine structure splitting. For the $m_J = 1/2$ coupled states, the necessary matrix is defined by

$$\begin{pmatrix} \left\langle \frac{1}{2},\frac{1}{2}\right| -\mu\cdot\mathbf{B}\left|\frac{1}{2},\frac{1}{2}\right\rangle & \left\langle \frac{1}{2},\frac{1}{2}\right| -\mu\cdot\mathbf{B}\left|\frac{3}{2},\frac{1}{2}\right\rangle \\ \left\langle \frac{3}{2},\frac{1}{2}\right| -\mu\cdot\mathbf{B}\left|\frac{1}{2},\frac{1}{2}\right\rangle & \left\langle \frac{3}{2},\frac{1}{2}\right| -\mu\cdot\mathbf{B}\left|\frac{3}{2},\frac{1}{2}\right\rangle + h\Delta_{FS} \end{pmatrix} = \begin{pmatrix} S_1 & C_1 \\ C_1^* & S_3+\Delta \end{pmatrix} \tag{2.52}$$

where the states are written as $|J, m_J\rangle$, the fine structure splitting is $h\Delta_{FS} = \left\langle \frac{3}{2},\frac{1}{2}\right| H_{FS} \left|\frac{3}{2},\frac{1}{2}\right\rangle$, $h$ is Planck's constant, and $H_{FS}$ is the Hamiltonian for the fine structure. The eigenvectors for this matrix show the probability densities of the states. By redefining the matrix into symbols, it can be solved entirely analytically. Using variables for the terms in the matrix above, the solution for the fractional amount of mixing is

$$\frac{(S_1 - S_3 - \Delta + \sqrt{4C_1^2 + (-S_1+S_3+\Delta)^2})^2}{8C_1^2 + 2(S_1-S_3-\Delta)(S_1-S_3-\Delta+\sqrt{3C_1^2+(S_1+S_3+\Delta)^2})}. \tag{2.53}$$

For a field of $0.6540$ T, the $^2P_{3/2}$ state is mixed with the $^2P_{1/2}$ state by $420$ ppb. So if the ion scatters photons at $125$ MHz, it will have made $\sim 50$ transitions to the $^2P_{3/2}$ state in $1$ s. However, only $6\%$ of the photons scattered to the coupled state results in a transition to the $^2D_{5/2}$, or about $3$ photons. The lifetime of the $^2D_{5/2}$ state is $1.168(7)$ s [70]. So if the ion is scattering photons with a period near the $P_{1/2}$ state lifetime, then there will be a slight buildup in the dark $^2D_{5/2}$ state. In order to keep Doppler cooling at an optimal rate,

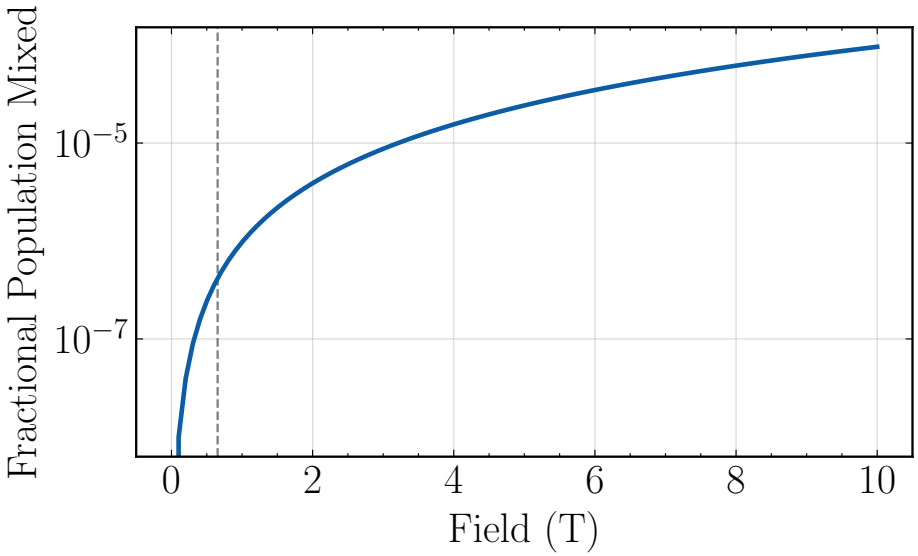


Figure 2.7: A plot to show the fractional amount of j-mixing for the calcium-40 P-states. The vertical dashed line shows the magnetic field produced by the permanent magnets in the trap region. The mixing at the intersection of the lines is $420$ ppb.

we find that it is best to keep an 854 nm laser on during the Doppler cooling process. At this field strength, the laser is not tuned to any transition, but simple kept in the center of the possible transitions.

*Shelving Transitions*

The transitions from the ground state, $^2S_{1/2}$, to the D-states are electric dipole forbidden, but they are electric quadrupole allowed. The $^2S_{1/2}$ to $^2D_{5/2}$ transition provides a means for 'shelving' the electron into the metastable state, explicitly removing it from the Doppler cooling cycle. This allows for the ability to perform state dependent detection of the ion.

## 2.4 Beryllium

Beryllium is the lowest mass alkaline earth metal. There is only one naturally occurring isotope with mass $9.012182$ amu and nuclear spin of $3/2$ [77]. Its nuclear spin produces hyperfine structure and thus clock transitions at certain magnetic field strengths [19]. The disadvantage to working with beryllium is that all of its transitions lay in the ultraviolet

(UV) and are inaccessible by direct diode lasers. Laser cooling of beryllium requires frequency doubling of another laser source [78, 79, 80].

### 2.4.1 Be Neutral Atomic Structure

Neutral beryllium has a $^1S_0$ to $^1P_1$ transition to use for first step of photoionization similar to calcium. However, this deep-UV transition is at $235$ nm and is the nearest transition from the neutral atom's ground state. So one could perform second harmonic generation on $470$ nm laser light to generate the necessary laser light. Then any light with wavelength $< 297$ nm will ionize the excited atom; including the $235$ nm laser light [81].

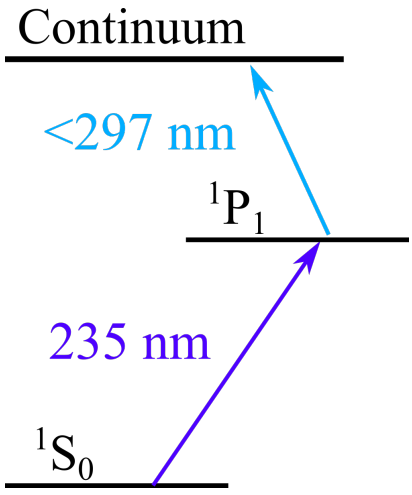


Figure 2.8: Level drawing of neutral beryllium relevant for photoionization.

Alternatively, we can use a multi-photon off-resonant photoionization method to ionize the atoms. This method involves using multiple photons whose sum of energy is larger than but close to the ionization energy needed. With this method, a significant peak power is needed. The ionization threshold for beryllium atoms is $9.32$ eV, which is $< 0.2\%$ below the energy from two $266$ nm photons [81].

### 2.4.2 Be ions

Beryllium ions have no low lying D states to complicate laser cooling like calcium. The states normally used in beryllium are the ground state, $^2S_{1/2}$, and two P-levels commonly

used for Doppler cooling, $^2P_{1/2}$ and $^2P_{3/2}$. Because of beryllium's nuclear spin of $3/2$ and the electron spin $1/2$, each level is split into 8 states. In Figure 2.9, the relevant states for Doppler cooling are shown and labeled via the strong magnetic field regime's good quantum numbers, $m_I$ and $m_J$.

*313 nm Doppler Cooling*

The S and P states are connected via electric dipole radiation at 313 nm. Doppler cooling has to be performed from one of the two stretch states in the $^2S_{1/2}$ manifold. These two states are $m_J = 1/2,\ m_I = 3/2$ and $m_J = -1/2,\ m_I = -3/2$. In any Penning trap magnetic field, these levels exist without mixing with other levels. All the other S-manifold states are mixed at various magnetic fields. This means that their transitions will not be closed upon scattering a photon to the $^2P_{3/2}$ manifold.

So one can chose to Doppler cool from the $m_J = 1/2,\ m_I = 3/2$ (denoted as upper stretch state) to the $m_J = 3/2$ state in the $^2P_{3/2}$ manifold. Alternatively, one can chose to Doppler cool from the $m_J = -1/2,\ m_I = -3/2$ (lower stretch state) to the $m_J = -3/2$ state in the $^2P_{3/2}$ manifold. Figure 2.9 shows the cooling transition from the upper stretch state. This cooling transition is a closed process, but it is still possible to off-resonantly scatter a photons with the nearest dipole allowed level in the P-manifold, $m_J = 1/2$. At the fields used in our Penning trap, the nearest P-state dipole allowed transition will be $> 10$ GHz away. The effective Rabi rate, $\Omega_{eff} = \frac{\Omega_0^2}{\Omega_0^2+\delta^2}$, for the off resonant electric dipole transition is scaled down by the detuning, $\delta$. The P-state lifetime is $8.1(4)$ ns, which corresponds to a P-state linewidth of $19.6(2)$ MHz [82]. In our system, where the resonant Rabi rate at saturation is $\sim 10^8$ Hz, the off-resonant scattering effect is small for $\delta > 10^{10}$ Hz. In practice, a small fraction of a beryllium ion cloud will end up in the dark ground state. In a similar process, the far off resonant cooling light eventually brings the electron back into the cycling transition.

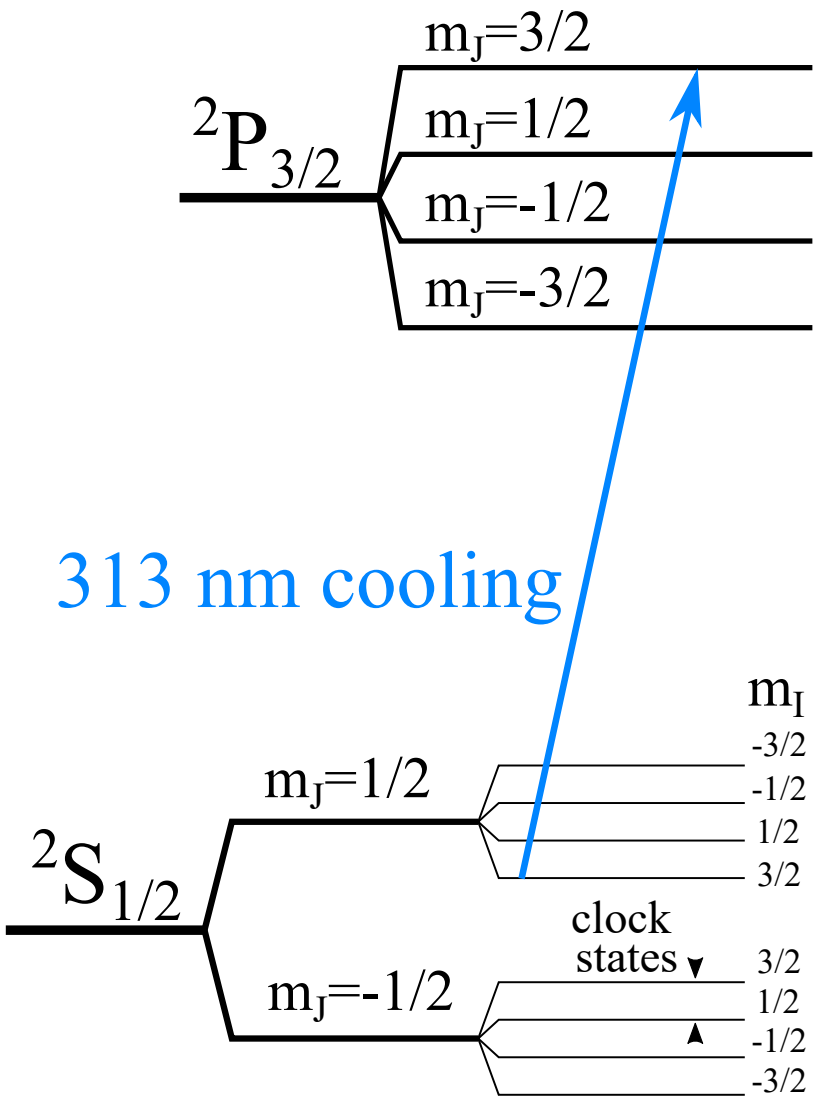


Figure 2.9: A diagram of a beryllium ion's ground state hyperfine structure, ${}^2S_{1/2}$, and transitions to the ${}^2P_{3/2}$. This diagram does not show the hyperfine structure of the ${}^2P_{3/2}$ state nor the ${}^2P_{1/2}$ level.

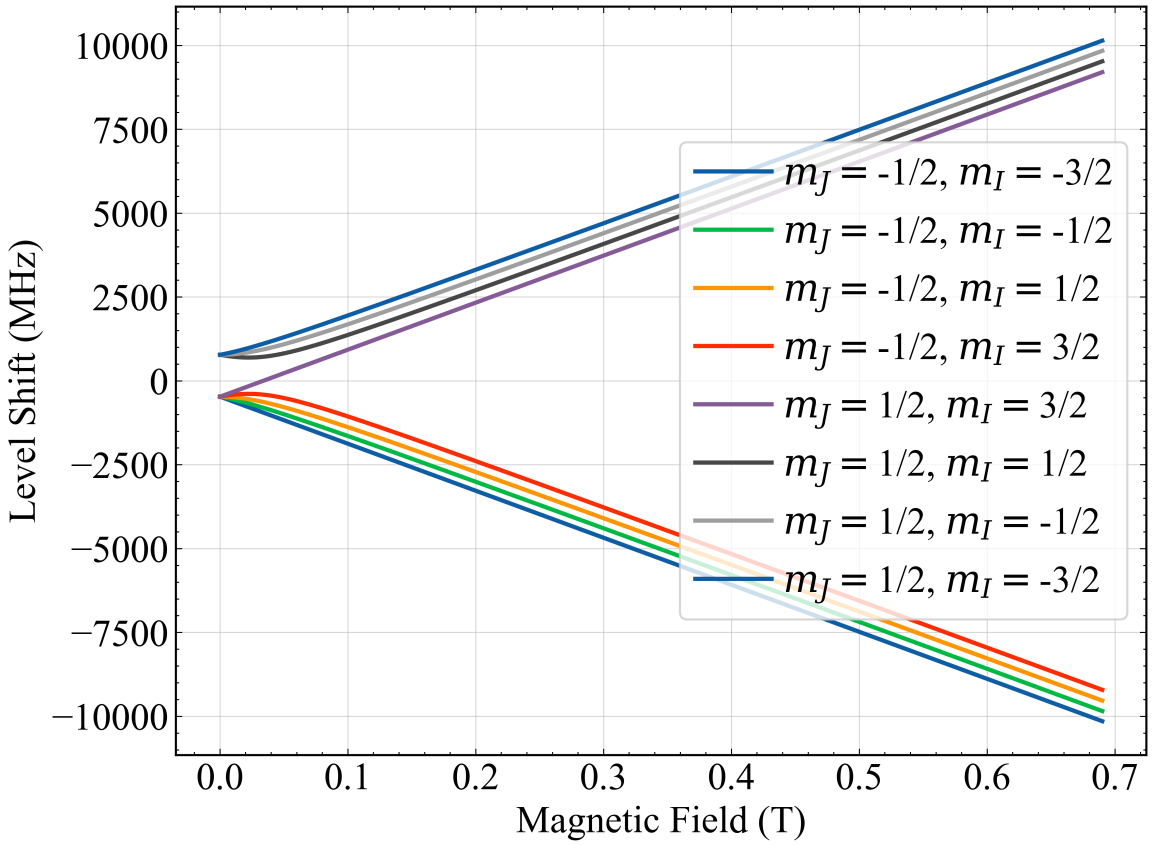


Figure 2.10: A diagram of a $^9Be^+$ ground state energy shifts for varied magnetic field strengths.

*Ground State Structure and Clock Transitions*

Because of the hyperfine structure and the Zeeman effect, the sensitivity of each state's frequency shift to a magnetic field changes for different magnetic field strengths. A plot of each states' shift for different magnetic field strengths can be seen in Figure 2.10. The solutions for the positions of these states are found by numerical diagonalization of the Hamiltonian containing the relevant terms of similar magnitudes. The details for each of the terms can be found in subsubsection 2.2.2.

There are magnetic field points where the magnetic field sensitivities, $d\nu/dB$, are the same for two different levels. These are the locations of clock fields. At these points, small variations of the magnetic field will not change the energy spacing between the two energy levels. This first order insensitivity makes the transition robust against magnetic pertur-

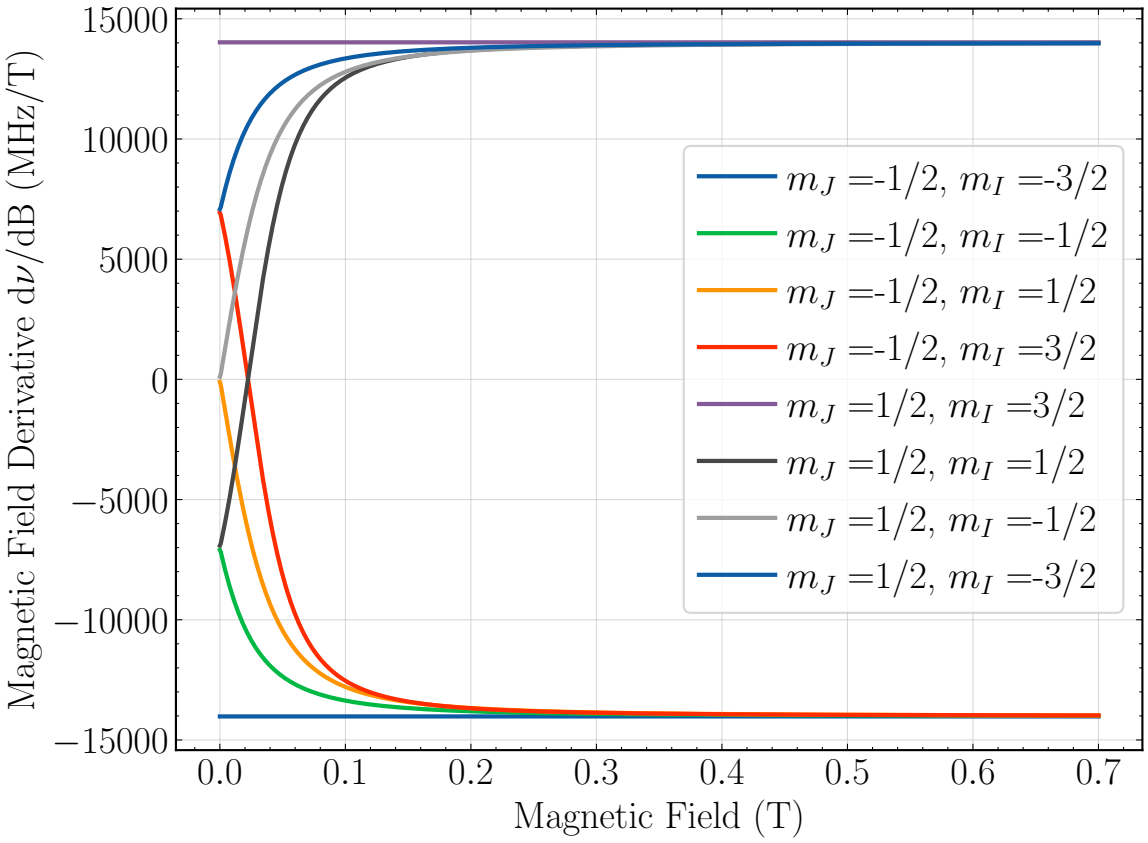


Figure 2.11: A diagram of a beryllium ion's S-state magnetic field sensitivities.

bations and ideal for use as an absolute frequency reference. Many of these transitions exist as can be seen in Figure 2.11. However, there are two clock transitions which are particularly well located at magnetic field strengths accessible by the fields created from permanent magnets, one at $0.6774$ T and another at $0.8194$ T. The plots in Figure 2.12 are zoomed in versions of the Figure 2.11 show where the magnetic field sensitivities intersect at these two clock fields.

The $0.6774$ T clock field is the closest accessible transition to the field produced by our permanent magnets. At that field strength, the nuclear spin flips, $\Delta m_I = \pm 1$, have transition frequencies of about $300$ MHz and the electronic spin flips, $\Delta m_J = \pm 1$, have transition frequencies of $18 - 20$ GHz.

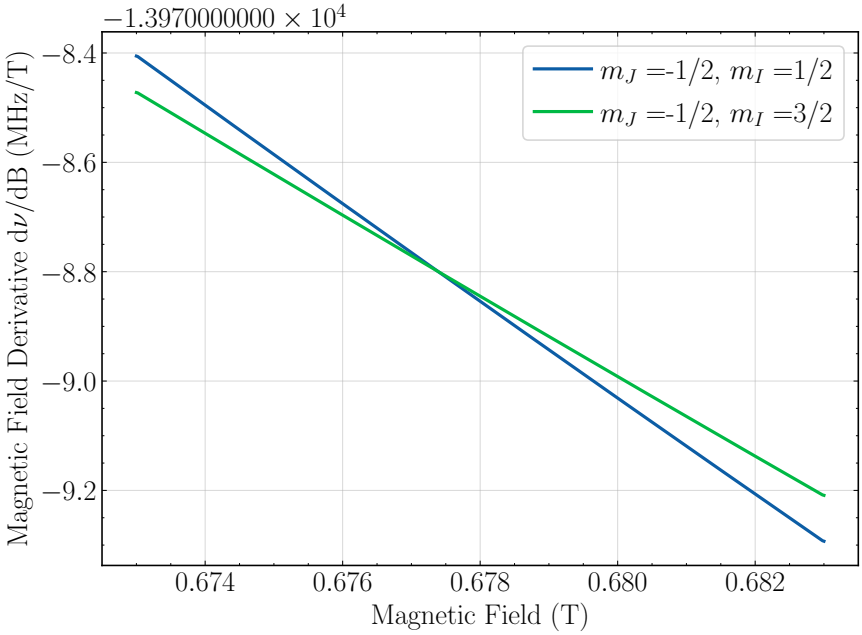


(a) Beryllium clock transition at 0.6774 T.

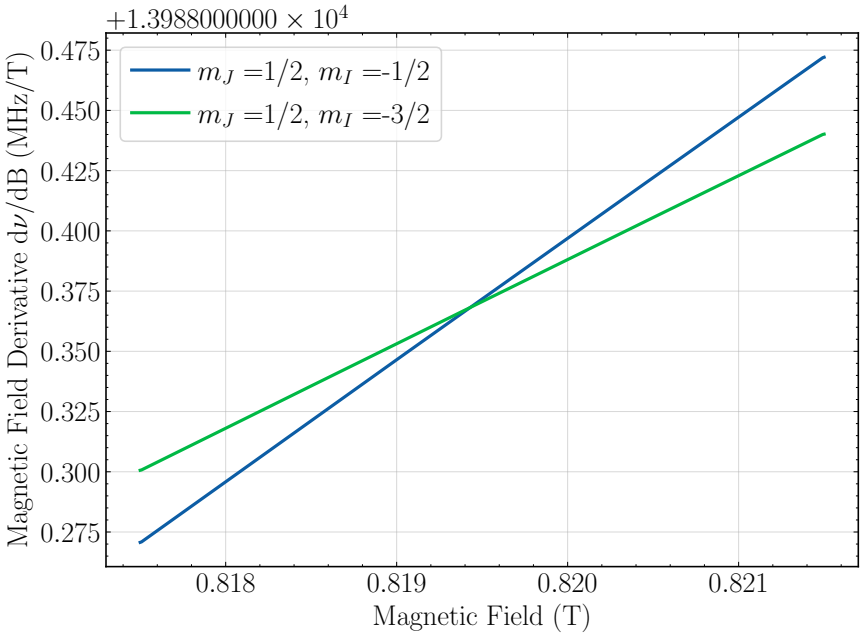


(b) Beryllium clock transition at 0.8194 T.

Figure 2.12: The two pairs of states in beryllium that form clock transitions at magnetic fields accessible with permanent magnets.

# CHAPTER 3

# EXPERIMENT SETUP

In this chapter, the details of the experimental apparatus and hardware are described. The trap electrodes and magnet configuration were designed and built according to the specifications determined by the analysis described in this chapter. The trap sits inside the constructed vacuum system shown in the following figures. I also list the laser systems and control electronics for implementing Doppler laser cooling and coherent quantum control.

## 3.1 Electrode Design

Using the polynomial expansion of the electric potential from a set of concentric ring electrodes, one can create an approximate quadrupole potential at the trap center. The calculations for creating such a trap with compensated parameters is detailed in [54, 83]. The potential can be described by

$$V = \frac{1}{2} V_0 \sum_{k=0,even}^{\infty} C_k \left(\frac{r}{d}\right)^k P_k(\cos\theta) \tag{3.1}$$

where $V_0$ is the applied trap potential, $d = \sqrt{\frac{1}{2}(z_0^2 + \frac{1}{2}\rho_0^2)}$ is the trap dimension. The parameter $z_0$ is the distance from the trap center to the endcap electrode and $\rho_0$ is the distance from the trap center to the ring electrode. The form of the potential contains the sum over all possible Legendre polynomial $P_k(\cos\theta)$, where $\theta$ is the polar angle. Azimuthal symmetry removes any dependence on the azimuthal angle $\phi$.

For an ideal quadrupole trap, all coefficients $C_4$ and higher are zero, while $C_2 = 1$. Then the axial frequency is directly described by $\omega_z^2 = \frac{qV_0}{md^2} C_2$, where $m$ is the trapped ion's mass and $q$ is its charge.

### 3.1.1 Trap Imperfections

With an imperfect trap, the higher order coefficients contribute to the axial frequency. If $C_4 \neq 0$, the axial frequency is shifted by

$$\Delta\omega_z = \frac{3E_z}{2qV_0}\frac{C_4}{C_2^2}\omega_z \tag{3.2}$$

where $E_z$ is the energy associated with the axial motion [83]. The effect of $C_6$ can be represented by modifiying $C_4$ to a effective amplitude-dependent coefficient, $\tilde{C}_4$. Then $C_4$ can be rewritten as

$$\tilde{C}_4 = C_4 + 5/2C_6\frac{E_z}{qV_0C_2}. \tag{3.3}$$

### 3.1.2 Trap Compensation

Using a trap with cylindrical electrodes will always result in anharmonicities that deviate from the ideal electric quadrupole. However, they can be largely mitigated via the use of compensation electrodes and an "orthogonalized trap" design [54]. The details for the calculations of the coefficients can be found in [83, 54].

The total potential from the ring, compensation, and endcap electrodes can be written as a superposition of the individual potentials $V = V_0\phi_0 + V_c\phi_c$. The form of $\phi$ for the ring and compensation electrodes is found by applying potential to that electrode and grounding the others. This creates the necessary boundary conditions to describe the potential. The solutions are

$$\begin{aligned}\phi_0 &= 1/2\sum_{k=0}^{\infty} C_k^{(0)}(\frac{r}{d})^k P_k(\cos\theta)\\ \phi_c &= 1/2\sum_{k=0}^{\infty} D_k(\frac{r}{d})^k P_k(\cos\theta)\end{aligned} \tag{3.4}$$

where we introduce another coefficient $D_k$ for the compensation electrodes. With this form, $V$ can now be rewritten as $C_k = C_k^{(0)} + D_k\frac{V_c}{V_0}$. Thus, it can be seen that the proper selection

of $V_c$ for a value of $k$ can make $C_k = 0$.

The downside to performing this potential compensation alone means that the axial frequency will change for each selection of a different compensation voltage. However, one can chose to make an "orthogonalized trap" with physical dimensions for the trap compensation electrode that sets $D_2 = 0$ [83]. Then the trap can be compensated without changing the axial frequency.

### 3.1.3 Trap Dimensions and Construction

The trap consists of a stack of concentric annular electrodes. The central ring electrode is segmented four ways to allow for optical access and application of a "rotating wall" potential (see chapter 4 for details). On top and bottom of the ring electrodes are a set of four compensation electrodes, segmented similarly to the ring electrodes. They allow for compensation of the potential to make a more quadratic form near the trap center. The ring and compensation electrodes are designed to sit together so that the trapped ions do not have any line of sight out of the trap region other than through the optical viewports. The electrodes fit together like stacked puzzle pieces. On top and bottom of this entire assembly are the endcap electrodes.

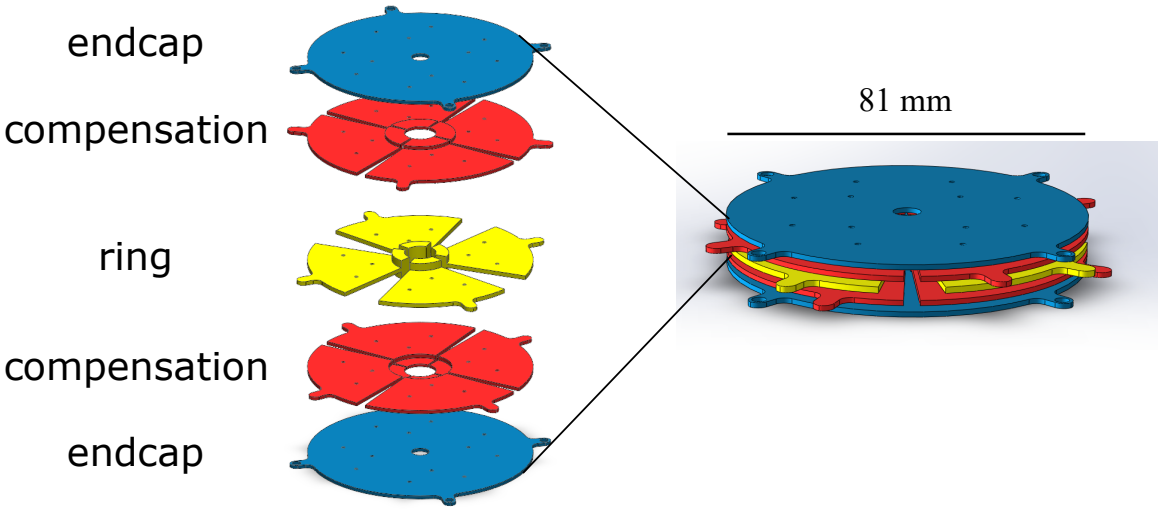


Figure 3.1: The electrode assembly on the right and the exploded view with labels on the left. They are color coded by function.

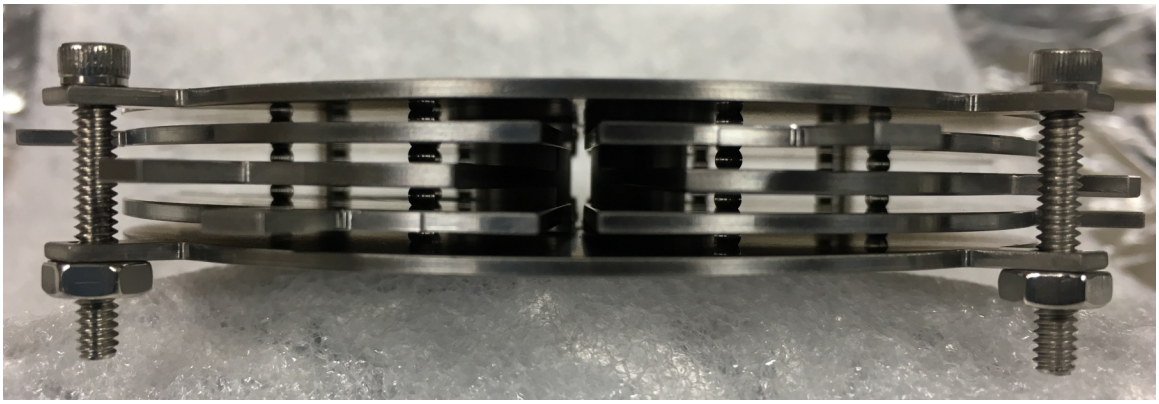

Figure 3.2: A picture of the trap in a temporary assembly with the sapphire ball spacers in place. The sapphire ring spacers are not included in this image.

Table 3.1: A table of the relevant trap electrode dimensions.

| Measurement | Distance | Description |
|---|---|---|
| $\rho_0$ | 5.72 mm | trap radius |
| $z_0$ | 5.1 mm | center-to-endcap distance |
| $z_g$ | 254 $\mu$m | electrode gaps |
| $z_c$ | 1.02 mm | compensation height |

Each endcap electrode is a planar electrode with a central hole radius smaller than the trap radial dimension, $\rho_0$. At the trap region boundary, each electrode layer is spaced by $254$ $\mu$m. There are three through holes in each electrode quadrant that define the layer spacing via 2 mm diameter sapphire ball spacers. The sapphire spheres sit in the holes for each consecutive electrode in the stack defining the electrode spacing, see Figure 3.2. The machining tolerance of the holes for the sapphire balls and each electrode's flatness was problematic for perfect referencing of the electrodes. Sapphire spacer rings were added around each ball to further reinforce the electrode spacing.

The size of the trap electrodes is altogether confined by the distance between the magnet pair and the size of the vacuum windows. We originally designed the electrodes under the assumption of an open endcap trap, because the endcaps included a hole for optical access.

Using the equations in [54], we chose the parameters tabulated in Table 3.1.

The values for the trap dimensions were used in the equations for the analytic fields to

find the ideal trap radius given the chosen electrode dimensions. The coefficients of the electrode potentials were plotted in order to find the optimal trap radius where $D_2 = 0$.

The trap dimensions were then used with the analytic form to solve for the potential value needed to null $C_4$ coefficients. However, this design was later changed, because the endcap electrode holes were covered with $88\%$ transmissive copper mesh. In the configuration with the mesh, the compensation electrode potential effectively changes the trap's axial frequency slightly, but they can still be used to tune out the fourth order electric field curvature.

Using SIMION software, the potential from each electrode was simulated and compiled. The software solves for the potential in a region of space given a set of electrodes and boundary conditions. By applying a potential difference between the endcaps and the ring electrodes, the field shape can be verified.

In a test case, $10$ V is applied to the endcap electrodes while the others are grounded. Then, the axial potential can be plotted by taking the potential along the axial line at the trap center. Within the $\pm 2$ mm from the trap center, a quadratic fit is performed to this region with a residual error along the sampled region $< 0.04\%$.

Each electrode has a tantalum wire welded to a tab that juts out of the circular body. Each wire has a push-on connector crimped to its end for connection to the vacuum chamber flange. The bottom endcap electrode sits in a Macor mount. The trap is assembled onto the endcap electrode in layers and is secured via eight 8-32 screws around the trap perimeter. At each of four locations on the trap perimeter is a pair of screws that connect to a central Macor standoff in order to electrically isolate the two endcaps. The lower screw of the pair also acts to fix the assembly to the Macor base. The assembled trap on the Macor riser with electrical connections is shown in Figure 3.3.

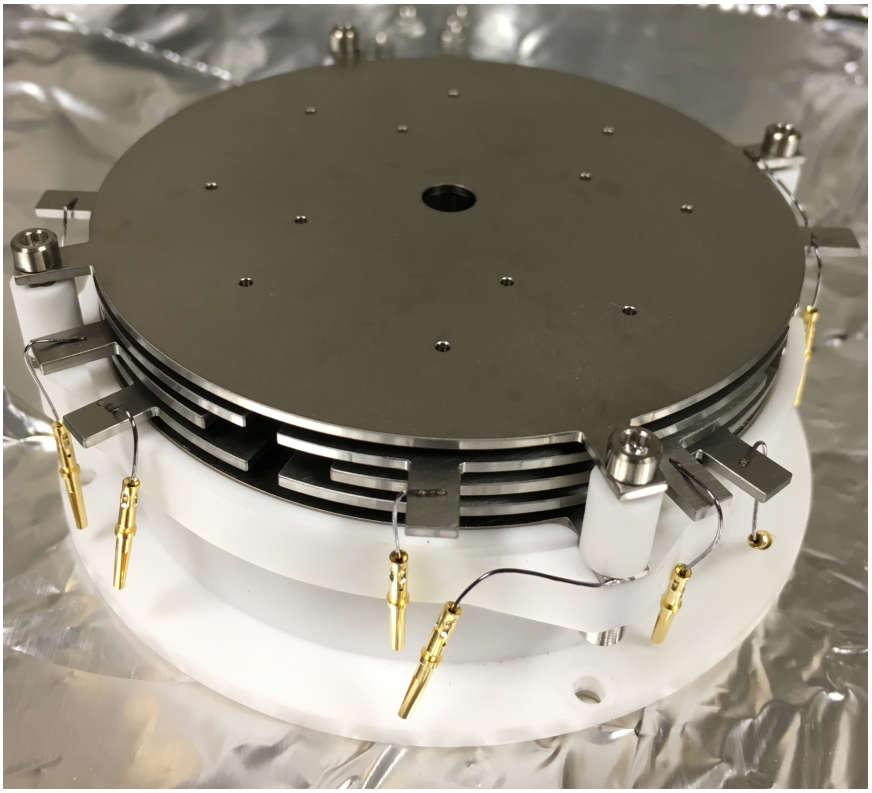

Figure 3.3: A picture of the trap assembled in the Macor base with the Macor standoffs, fixing screws, and spot welded wire connections with crimped push-on connectors.

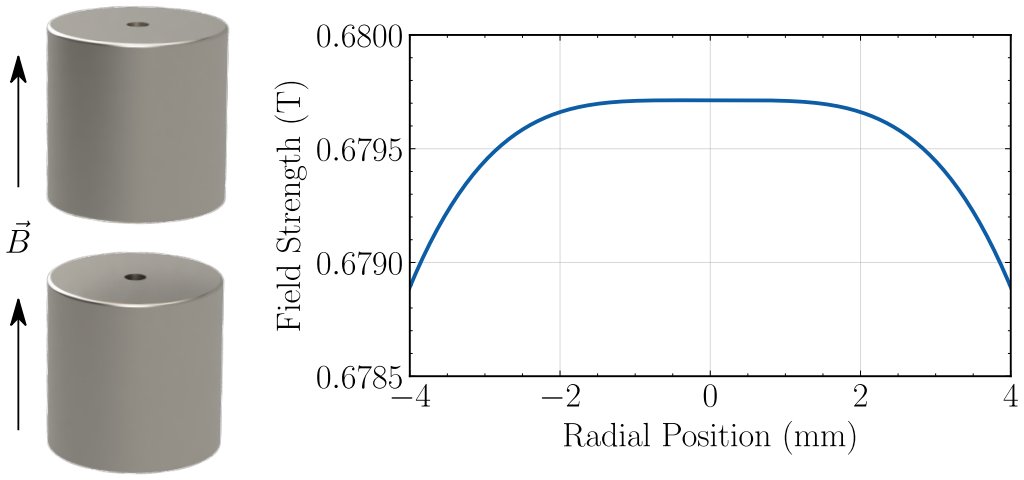


Figure 3.4: (Left)A rendered image of the 2” OD, 0.25” ID, 2” tall, rare earth permanent magnets at the magnet spacing configuration for highest uniform field between them. (Right) The magnetic field as a function of radial position.

## 3.2 Magnetic Field Source

Penning traps need a static axial magnetic field, about $> 0.5$ T, to perform trapping. Traditionally, this field is created using a superconducting magnet. They require liquid cryogens to keep the solenoid at superconducting temperatures and can take a day or more time to reach operating temperature from room temperature. The apparatus' size and form factor make optical access challenging. We created a different kind of Penning trap where the magnetic field is supplied by a pair of rare-earth permanent magnets (REM).

### 3.2.1 Rare-earth Permanent Magnets

The ideal magnetic field for a Penning trap is a uniform axial magnetic field. The magnet geometry needs to have space for trap electrodes, as well as radial and vertical optical access for Doppler laser cooling and imaging as well as introduction of microwave radiation.

While complex multi-magnet geometries can be used to create very uniform magnetic fields, the simplest scenario involves a pair of ring magnets with axial magnetization, see the left side of Figure 3.4. This geometry allows for the requirements mentioned above.

The details of our magnet design was guided by a paper authored by Frerichs et al. (1992) [84]. In their paper, they detail an analytic expressions for permanent ring magnets using a three-dimensional multipole model. Their model characterizes the field using the magnetic potential. With the assumption of azimuthal symmetry, they show that

$$\Phi_M = B_r \sum_{l=1}^{\infty} C_l r^l P_l(\cos\theta) \tag{3.5}$$

where $B_r = \mu_0 M_0$ is the remanence field with magnetization $M_0$ and permeability of free space $\mu_0$, arbitrary constants $C_l$, radial position $r$, the Legendre polynomials $P_l(x)$, and spherical coordinate $\theta$. The value of $C_l$ is given for a cylinder with radii $\rho_1$ and $\rho_2$ and endcaps at $z_1$ and $z_2$ by

$$C_l = \frac{1}{2}\int_{\rho_1}^{\rho_2} \rho' d\rho' \int_{z_1}^{z_2} dz' \left\{ \cos[\alpha(\rho', z')] \frac{\delta}{\delta z'} + \sin[\alpha(\rho', z')] \frac{\delta}{\delta \rho'} \right\} \frac{P_l(\cos\theta')}{r'^{l+1}} \tag{3.6}$$

where $\alpha$ is the local angle between the magnetization vector and the z-axis. This equation can be simplified further through recursion relations of the Legendre polynomials. The expression of the coefficients is then

$$C_l = \frac{1}{2}\int_{\rho_1}^{\rho_2} \rho' d\rho' \int_{z_1}^{z_2} dz' \frac{1}{r'^{l+2}} \left\{ -(l+1)\cos\alpha P_{l+1}(\cos\theta) + \sin\alpha P_{l+1}^1(\cos\theta') \right\} \tag{3.7}$$

but for an axially magnetized cylinder, $\alpha = 0$, the coefficients are

$$C_l = -\frac{l+1}{2}\int_{\rho_1}^{\rho_2} \rho' d\rho' \int_{z_1}^{z_2} dz' \frac{\cos\alpha}{r'^{l+2}} P_{l+1}(\cos\theta). \tag{3.8}$$

The Equation 3.5 and Equation 3.8 give an analytic form for the magnetic field from an axially magnetized cylinder. By duplicating this model and offsetting it in the axial direction by the desired gap, one can model the expected field for a ring magnet pair with a gap separation. By iterating on magnet spacing in the analytic field model and determining

the field curvature between the magnets at each step, one can solve for the optimal magnet spacing that removes the 2nd order field curvature.

For example, with N52-grade NdFeB ring magnets with an inner radius of $3.175$ mm, an outer radius of $50.8$ mm, and a height of $50.8$ mm, one calculates that the optimal magnet gap is $23.93$ mm. The magnetic field strength as a function of radial position is shown on the right in Figure 3.4. The average field in the uniform region of the plot is $0.6797$ T.

## 3.3 Vacuum System

A rendering of the vacuum system components assembly can be seen in Figure 3.5. At the center of the experiment vacuum package is a $6$" conflat (CF) flange octagon[1]. Of the eight $2.75$" CF mounting sides of the octagon, four sides have nonmagnetic viewports (shown by red window arrows in Figure 3.5), two have electrical feedthrus, one for a non-evaporable getter pump[2], and one for a CF nipple extending outwards to the ion pump and all-metal valve. One of the electrical feedthrus is used for the oven connections and the other for the trap electrical connections. The ion pump is electrically isolated from the chamber via a ceramic break, which is necessary to minimize any electrical noise from the pump's many kilovolt magnitude operating potential. The vacuum assembly and mount stands on 1.5" diameter, 7.5" tall posts in order to raise the system away from the magnetic optical table.

[1] Kimball Physics
[2] SAES Capacitorr D200

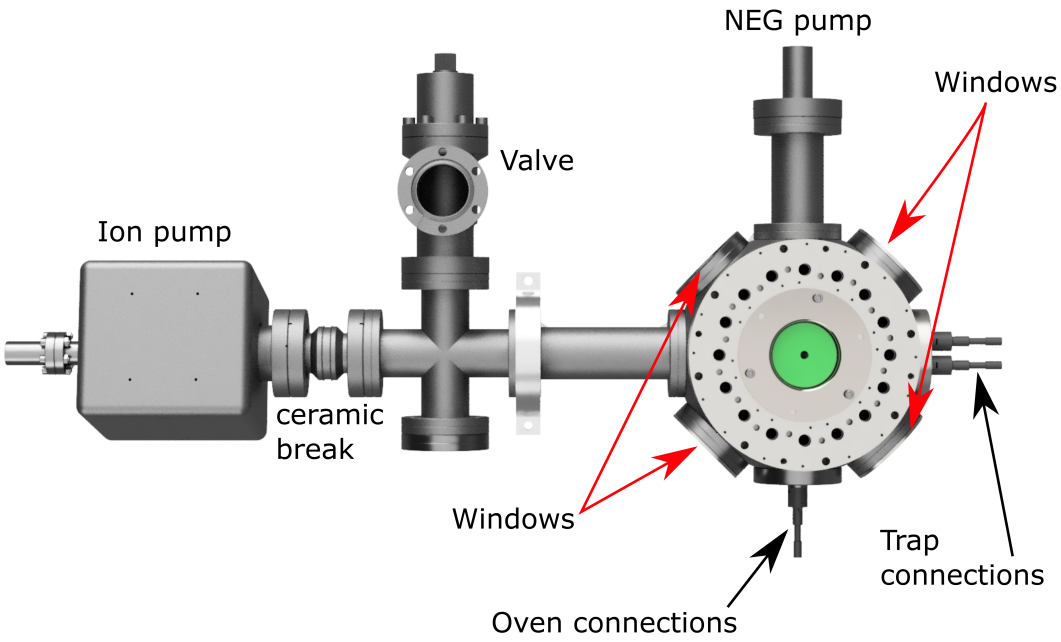


Figure 3.5: This is a CAD assembly top-down view of the vacuum system with the final reentrant windows installed with configuration D magnets.

### 3.3.1 Reentrant Flanges

On the top and bottom of the octagon are 6" CF flanges. In this design, the permanent magnets sit outside the vacuum chamber, but still near the trap via reentrant viewports on the top and bottom CF flanges. The reentrant viewports allow for adequate placement of the magnets nearest to the ions, and provide some optical access in their centers. The chamber was setup in four different configurations while working towards a final version with custom reentrant viewports. The rendered CAD model shown in Figure 3.5 shows the final configuration.

Configuration A used two custom reentrant viewports made from 316LN grade stainless steel and fused silica windows. Initial tests with the viewports on the chamber at room temperature held high vacuum ($10^{-7}$ Torr) without any issues. We were able to pump down the chamber successfully, however, as soon as we started to perform a bake-out process, the

window-to-metal braze failed and leaked, likely due to a coefficient of thermal expansion (CTE) mismatch. The viewports were sent back for evaluation and replacement.

Configuration B used two milled out CF blanks on the 6" ports. This had the disadvantage of keeping the magnets farther away from the ions. These magnets enabled some initial neutral atom spectroscopy in an intermediate field that was not quite strong enough to directly perform trapping. This configuration only created fields of $< 0.23$ T.

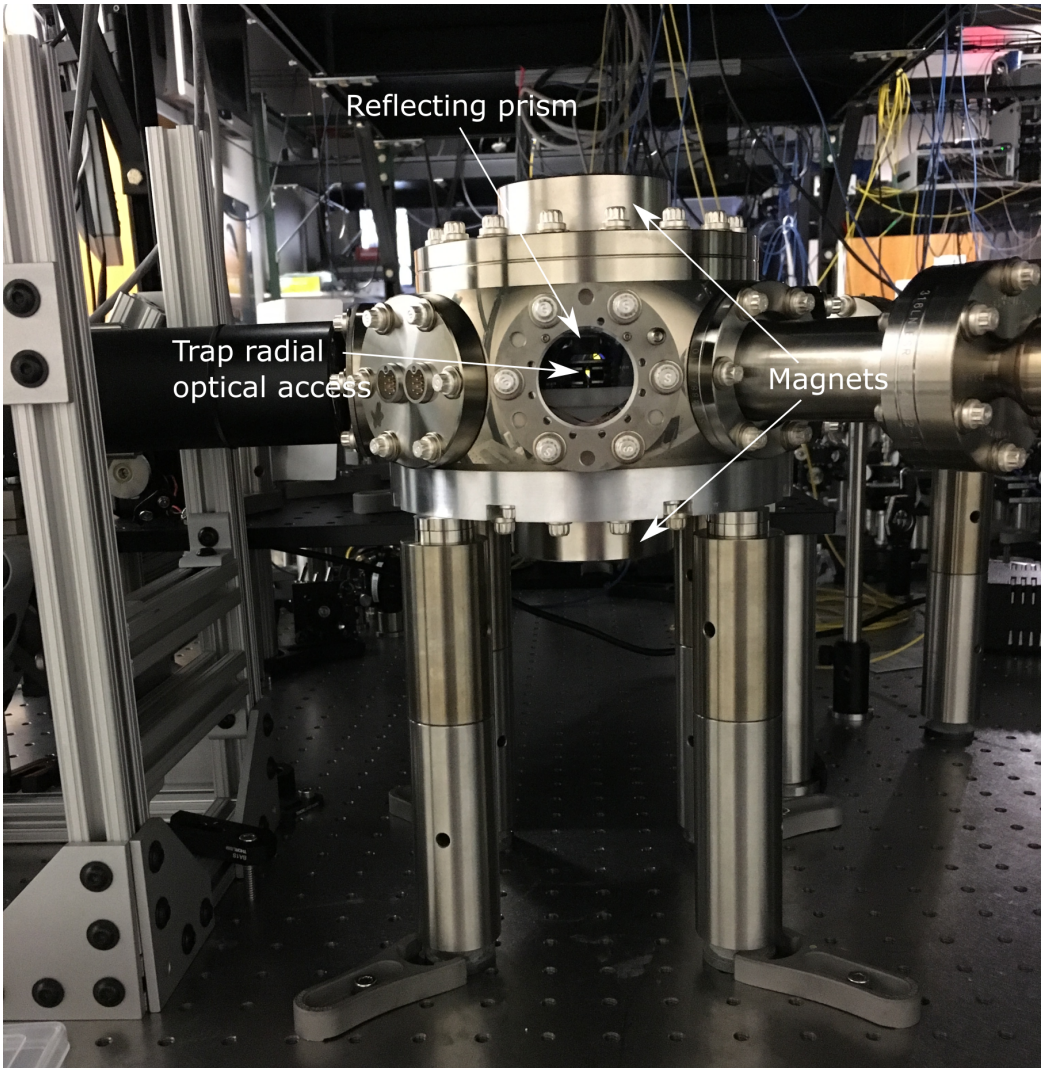


Figure 3.6: An image of the radial beam access through the viewport. The edges of the trap electrodes can be seen in the image. A pair of $76.2$ mm diameter magnets sit in the solid reentrant flanges on the top and bottom of the chamber.

While waiting for replacement viewports, 316L grade stainless reentrant flanges were

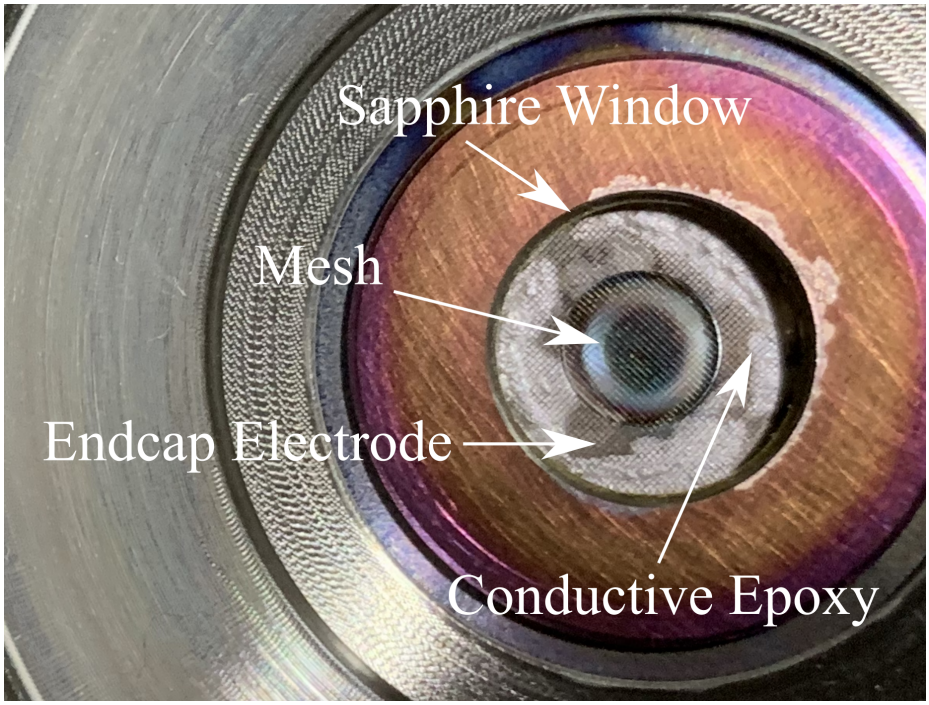


Figure 3.7: An image looking down at the trap's top endcap electrode through the sapphire window. The window's edge is brazed into the reentrant viewport. The fine copper mesh is epoxied to the electrode to shield the ions from potential window charging. The mesh and epoxy can be seen.

installed (configuration C). These flanges had the advantage of being more structurally sound without brazed glass. In order to gain axial optical access to the trap region, a prism was mounted on a cube of copper and then onto the flange's vacuum side face using ultra-high vacuum (UHV) safe epoxy. This allowed for vertical optical access into the chamber through the radial viewports. For this configuration, a pair of N52 NdFeB magnets were used with an inner diameter of $0.3125$", an outer diameter of $2.5$", and a $3$" height. The ions were not shielded from the reflecting prisms located just above/ below the endcap electrodes. Even though, the dielectric reflecting surface acted as a conductor in contact with the vacuum chamber, trapping was very difficult in this configuration. This was likely due to stray fields from the prisms.

In configuration D, the replacement reentrant viewports were installed. In this iteration of the viewports, an anti-reflection coating (AR) coated sapphire window was brazed into a titanium ring. The AR coating covers light at 313 nm and 397 nm for beryllium and

calcium's cooling transitions, respectively. This configuration was used to take most of the data collected in this thesis. Figure 3.8 shows a CAD model section analysis through the trap center of the assembled chamber, trap, magnets, and viewports. The cylindrical hollowed region shows the trap region where the ions are confined.

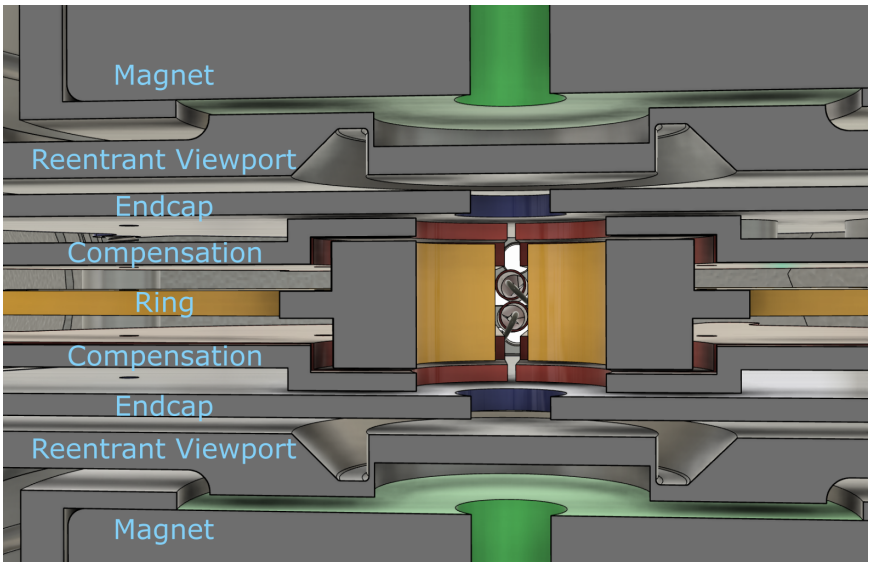


Figure 3.8: A false color cad rendering of the trap and chamber in a section view. The image shows the symmetric layout of the trap electrodes, the vacuum chamber boundary at the reentrant viewports, the magnet holders, and the magnets.

### 3.3.2 Oven designs

In order to produce a vapor of atoms for trapping, we rely on a resistivly heated oven design. The standard oven used at GTRI consists of a stainless steel (SS) tube about $25$ mm long. The tube is crimped shut on one end with a SS wire inside the end so that about $50$ mm of wire sticks out of the end of the crimped end. The crimped side is also spot welded to make sure that it is completely closed with the wire fixed in place. On the other end of the tube, another $50$ mm SS wire is wrapped around the end once and welded into place. The leftover wire is bent downwards towards the other wire end. Both remaining ends are bent at a $90^{\circ}$ angle and a small loop is added. The loop is only big enough to wrap around a screw and underneath a washer for connection to a mount/ electrical connection. The open end of the tube is filled with raw the desired element material. In order to make

a calcium oven, the tube is filled with either shavings of calcium or cut-up pieces. Then when a current is run through the wire leads, the tube is heated hot enough to sublimate the material inside to produce the atomic vapor.

This style oven is commonly referred to as a 'blunderbust' oven. Its single open end sprays atomic flux in a large cone with little directional selectivity. The stainless steel version works well for calcium given its melting temperature of $842^\circ$ C is below that of SS at $\sim 1450^\circ$ C [61]. Unfortunately, beryllium is pretty similar in melting temperature at $1287^\circ$ C. A titanium oven was constructed for testing with beryllium, because of its greater melting temperature at $1670^\circ$ C, and a tantalum oven was constructed with the similar design. The tantalum oven version was the only successful blunderbust style oven for beryllium given tantalum's high melting temperature, $2980^\circ$ C. The other oven material types melted before sublimated beryllium was observed.

The ovens were tested in a separate vacuum system than the trap. It was composed of a $4.5$ " octagon chamber mounted directly to a $4.5$" nipple and turbo pump. The vacuum chamber had a two pin electrical feedthru mounted to one of its radial $1.33$" CF ports, while the other radial ports were closed with blanks or viewports. The top $4.5$" flange of the octagon was sealed with a large viewport to allow for easy viewing of the test ovens as shown in Figure 3.9. One or two constructed ovens were inserted inside the vacuum chamber at a time and fixed to a custom mounting solution. This mount was designed for mounting ovens underneath planar microfabricated ion traps below a CPGA package. In order to test the ovens, they were heated enough to sublimate significant material. A glass microscope slide was inserted just above the opening of the oven. Upon heating of the oven to the sublimation temperature via resistive heating, the sublimated atoms will plate the glass slide leaving a visible thin film of metal in a pattern consistent with the solid angle of the oven aperture.

The ovens are filled with rocks of calcium or beryllium wire. Calcium reacts quickly with water forming calcium hydroxide and hydrogen gas. Calcium also reacts in air to form

calcium oxide and calcium nitride[3]. After reacting, the resultant calcium oxide and calcium nitride are white and very brittle. At this point, it is useless for experiments.

Fresh calcium rocks are usually cut into small pieces using wire cutters and inserted into the oven tube. After calcium is installed in an oven, it needs to be placed in vacuum quickly or else the reaction process will convert all of the atomic sample. The calcium filled ovens created remain in air for no more than $30-60$ minutes before they are installed in a vacuum system and the system evacuated. Beryllium however, is not quite as reactive in air and doesn't need special handling for avoiding chemical reactions[4]. The beryllium ovens made use beryllium wire instead[5]. The wire is cut into small pieces, shorter than the length of the oven tube and are packed into the oven.

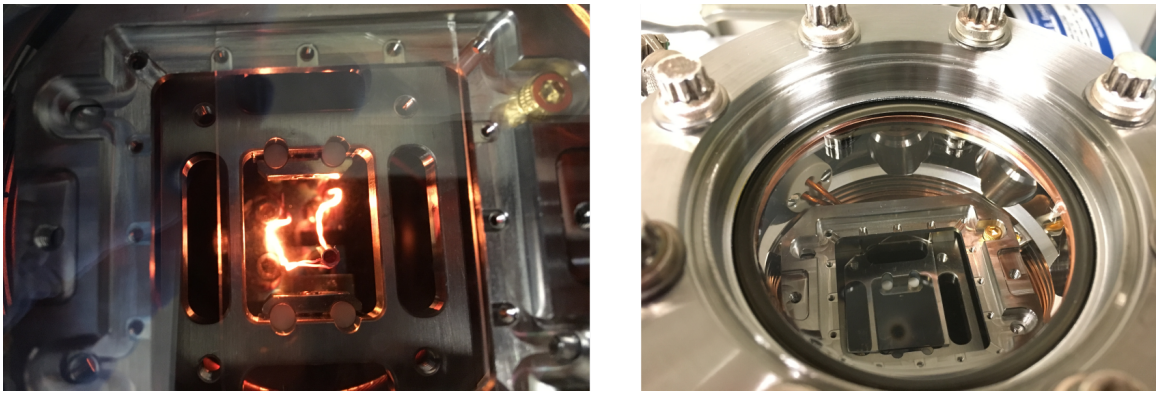

Figure 3.9: The image on the left shows a tantalum oven with double-stranded oven wires instead of thicker wire. The image on the right shows the result of successful plating after turning the oven current off.

In the first tests using a stainless steel oven with a beryllium sample, the SS tube promptly melted. In successive tests with a titanium oven, the wire leads melted before the oven reached the beryllium sublimation point. Before those points were reached, each of the ovens themselves began to sublimate as well. This can be seen on the two left-most slides of Figure 3.10.

[3]Calcium is reactive with water, but also can ignite in air and can cause a small rapid exothermic reaction in the form of an explosion if not handled properly.

[4]Although less reactive than calcium, beryllium is highly toxic.

[5]Thank you to the Ion Storage Group at NIST for letting us use one of their ovens.

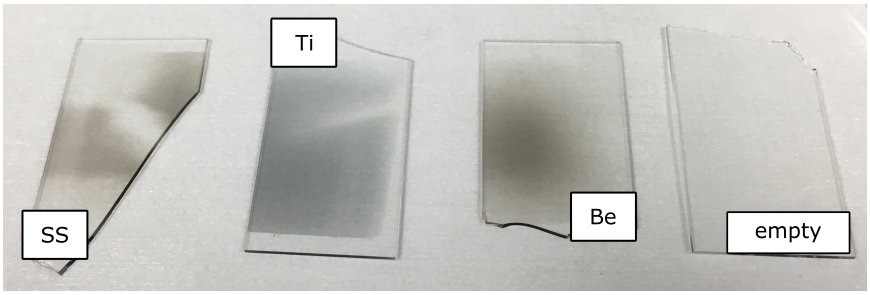


Figure 3.10: Image of glass slides for various plating tests. The SS and Ti slides show plating of the ovens instead of the containing material before oven failure. The Be slide shows beryllium plating from a tantalum oven. The empty slide shows the test plating from an empty tantalum oven for comparison.

However, once the tantalum ovens was created, we were able to see plating of calcium and beryllium. in these tests, plating occurred around $9$ A for beryllium and $4 - 5$ A for calcium. An image of the plating from the beryllium oven on a glass slide can be seen in Figure 3.10. For comparison, a plating test was also run with an empty tantalum oven, seen in the right-most slide of Figure 3.10.

In other tests, an ionizer grid of a residual gas analyser[6] (RGA) replaced the top viewport on the octagon with a distance about an inch from the oven aperture to directly measure atom production. Diaphragm roughing and turbo pumps [7] were used to pump the vacuum system down to $< 10^{-6}$ Torr before any tests were performed. The experiment was run with constant tracking of RGA partial pressures for nitrogen, beryllium, tantalum, calcium, and water. At discrete time steps, the oven current was turned up to $10$ A from 0 and then turned off. The plot in Figure 3.11 shows the data. The data shows that a partial pressure of $> 10^{-8}$ Torr was measured at the same current settings used to create plating in the experiments with the glass slides. As the oven heats up, the thermal conduction also seems to heat nearby areas in the chamber which may be the cause of the rising pressure of the background calcium gas pressure measured. In addition, the increase can also be attributed to the air that was absorbed into the chamber walls/ mounting materials. The test chamber was used for testing calcium ovens many times before these experiments, which explains

[6]SRS RGA, with continuous-dynode electron multiplier (CEM)
[7]Peiffer HiCube system

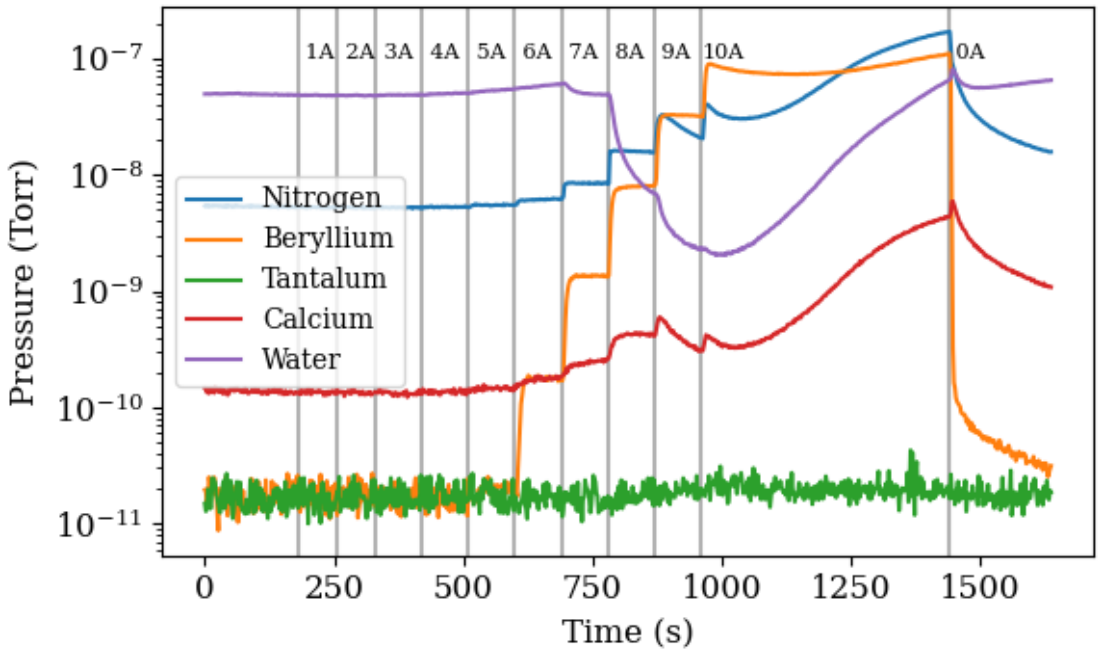


Figure 3.11: Data collected during a ramp up of the blunderbust style tantalum oven filled with beryllium wires. Several other atoms and molecules' partial pressures are also plotted for comparison. The times when the current were changed are denoted with gray vertical lines and labeled with the changed current value.

the background pressure of calcium that was measured when heating the ovens.

Later, it was found that the beryllium blunderbust style oven was problematic for trapping. When the oven was run for a beryllium loading attempt, the background pressure from other atoms/ molecules would increase, and the loading process would ionize them as well. In addition, the beryllium trapping lifetime was much lower than it should be for a reaction rate at the vacuum system's background gas pressure. See more discussion of this in subsection 6.3.1.

In order to circumvent the problems with the blunderbust style oven, it was decided to use the beryllium oven type used in the Ion Storage Group at National Institute for Standards and Technology (NIST) Boulder. The setup for creating this oven type involves co-wrapping thin beryllium wire around thin tungsten wire. The details to create these ovens can be found in many theses [85], but a particularly description can be found in Harrison

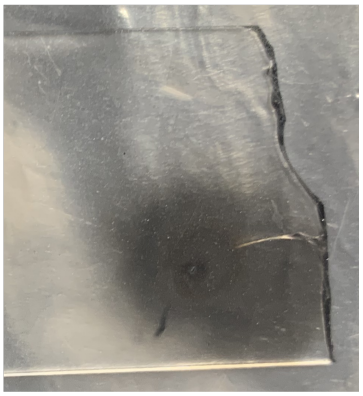

Figure 3.12: The picture on the left shows the GTRI oven mounted on the oven assembly for attaching to the chamber groove grabbers. The picture on the right shows the result of test plating of the oven on a glass slide.

Ball's thesis [86]. Luckily, the Ion Storage Group[8] had some extra ovens in storage that they were willing to share with us.

## 3.4 Laser Systems

A collection of laser systems were setup and utilized for production of ions, Doppler cooling, and state manipulation of calcium and beryllium ions.

### 3.4.1 Calcium Lasers

Each of the diode laser systems that were setup, are contained to their own breadboards. Each breadboard is 1' long by 2' wide and 60 mm thick with honeycomb support structure inside[9]. The breadboards sit on standard lab grade optics tables that are vibration isolated from the room via compressed-air-floated legs. Each breadboard hosts a laser head and optics to divide the laser power between fiber launches. A sample of each laser is coupled

[8]Special thank you to Dietrich Leibfried
[9]Thorlabs Nexus Breadboard

into a fiber and sent to a broadband optical switch which is coupled to a wavelength meter[10]. The rest of the light is then sent to acousto-optic modulators (AOMs)[11] for fast switching of the light ($< 1\mu s$ switch time) during an experiment.

One of the $397$ nm lasers used for cooling and the $729$ nm lasers, use a 'cateye' double passed configuration of their AOMs similar to what is described in [87]. The input beams are focused into the AOMs with $100$ mm focal length AR coated lenses so that the diffracted orders are parallel to the 0th order beam and collimated once they pass through the second lens after the AOM. The second lens is located a focal length away from the AOM diffraction point in order to provide this behavior. A retro-reflecting mirror sends the beam back along the same beam path where the second pass repeats the frequency shift from the first pass. A quarter waveplate after the AOM provides a total half-wave phase shift after two passes so that the output beam can be separated from the input beam with a polarizer. The focused beam in the AOM allows for faster AOM switching, because the beam size in the AOM is small.

Doppler cooling is performed with two separate 397 lasers tuned to the S-P $\sigma_-$ and $\sigma_+$ transitions. The $\sigma_-$ 397 nm laser is a External Cavity Diode Laser (ECDL)[12] (denoted 397Mog in diagrams) and the $\sigma_+$ 397 nm laser is a TA-SHG Pro laser[13] (denoted 397SHG in diagrams). The 397SHG system consists of an ECDL laser at $794$ nm which is amplified by a tapered amplifier (TA) before being frequency doubled inside a resonant bowtie cavity.

Repumping is achieved with a cateye laser[14] at 866 nm. The four different $866$ nm frequencies needed to repump from the $^2D_{3/2}$ state are provided with a high frequency fiber electro-optic modulator (EOM)[15]. The laser center wavelength is selected such that only the +1 and -1 orders of the each EOM modulation tone is necessary for driving the repumping transition. This scheme isn't perfectly resonant with the transitions because of

[10]HighFinesse WS8
[11]Brimrose Corp. and IntraAction
[12]Moglabs
[13]Toptica Photonics
[14]Moglabs (CEL)
[15]EO Space

the second order Zeeman shift asymmetrically moves the levels, by ($< 10$ MHz).

Shelving is achieved with a 729 nm laser, which was created either from a CW mode locked Ti:Sapphire Matisse laser[16] or a Ti:Sapphire SolsTiS[17]. In order to address the narrow $^2D_{5/2}$ transition, the lasers are locked via a Pound-Drever-Hall locking scheme to ultra-high finesse cavities[18] (finesses ranging from 40000-200000). The PDH locks were performed using electronics modules, Fast Analog Linewidth Control modules (FALC)[19]. The frequency correction of each laser is performed by feedback to a voltage controlled oscillator that drives an AOM. The laser output is directly sent into the AOM before being distributed to experiments, a wavelength meter, and the high finesse cavity.

Deshelving of the $^2D_{5/2}$ state is accomplished with a distributed Bragg reflector (DBR) laser[20] at 854 nm. Without an EOM scheme like described for the 866 nm laser, the 854 nm laser is nearby but not resonant with any transition. For this configuration, repumping requires many tens of milliseconds. However, the use of this laser for repumping during Doppler cooling does not require resonance due to the small rate that the ion falls into the metastable state.

### 3.4.2 Beryllium Lasers

The beryllium cooling laser is a $313$ nm laser generated via fourth harmonic generation. The laser exists as a commerical system[21]. The laser system consists of an ECDL laser at $1252$ nm, a tapered amplifier (TA) for the 1252 nm laser light, a second harmonic generating bowtie cavity for converting $1252$ nm to $626$ nm, and then finally a fourth harmonic generating bowtie cavity for generating $313$ nm. The output power in the UV is $200 - 300$ mW and is more then enough for experimental requirements.

At this wavelength (313 nm), the laser light cannot be transmitted through standard

[16] Spectra Physics
[17] M Squared Lasers
[18] Stable Laser Systems
[19] Toptica Photonics
[20] Photodigm
[21] Toptica Photonics

fiber. Recent work has shown that hydrogen treated PCF can transmit single mode light without the solarization that plagues other fibers [88, 89]. Unfortunately, commercial versions of these hydrogen-treated fibers are not yet available. For the work in this thesis, $313$ nm light was sent along the optics table in free-space or through PCF at powers low enough to delay solarization for years[22].

The output of the $313$ nm laser is first sent to a mode cleanup apparatus. This apparatus is simply a one-to-one telescope made up of short focal length lenses with an aperture placed at the focus between them. By focusing the beam through a hole $25\mu$m in diameter, stray light not part of the Gaussian beam is removed from the propagating beam.

The output of the mode cleaner is then sent to a double-passed AOM setup in the cateye configuration; the setup is similar to the one described in [87]. The incoming and outgoing light is separated with a Wollaston polarizer in order to achieve a high extinction ratio. This frequency shifted light is then sent to an EOM[23] for creation of the additional laser frequencies needed to prepare the ion in one of the clock states. From here, the light is sent to a breadboard for combination and splitting with the other lasers before entering the chamber, as is shown in Figure 3.13.

### 3.4.3 Laser Frequency Stabilization

On each laser board, a fraction of the total laser light is coupled to an optical fiber and sent to a fiber switch and finally to a wavelength meter[24]. The wavemeter is actively recalibrated every $10$ minutes to a $852$ nm DBR laser[25] that is locked to an cesium-based vapor cell[26]. This enables a wavemeter precision of $< 1$ MHz and an accuracy of $< 2$ MHz. The wavemeter measurements are retrieved by a locking GUI, implemented in Igor Pro. A dedicated computer runs the locking experiment where the wavemeter values are compared

[22] The radial PCF was mostly solarized after more than two years of use
[23] Qubig
[24] WS8 Toptica/ High Finesse
[25] D2-100-DBR Vescent Photonics
[26] D2-210 saturated absorption spectroscopy module

to a setpoint for each laser. The program calculates a error signal with a given PID loop and sets a DAC[27] analog output voltage. The feedback voltages are sent back to the laser piezos for external cavity length correction. The lasers with narrower linewidth requirements are locked to high finesse cavities using a PDH locking method as mentioned above. A diagram of the controls for this scheme are included in Figure 3.15.

### 3.4.4 Optics at Chamber

After the lasers used are frequency stabilized and switch enabled via AOMs, the light is sent to a 2' x 2' breadboard at the chamber. The light for many of the channels is picked off and monitored with photodiode (PD). The laser powers of all the UV radial lasers are stabilized using PD signals. The feedback loops are implemented with either NIST PID controller [90] or LB1005s[28]. The feedback signal is sent to the IF port of a frequency mixer which is in line with the RF frequency source before being sent to the laser's AOM. This acts to modulate the amplitude of the RF signal to correct for amplitude fluctuations.

The 397 nm lasers are combined on a Wollaston polarizer with crossed polarizations. The polarizations are rotated by $45^\circ$ so that they are both at $45^\circ$ to the following Glan laser polarizer axes. This combines the 397 lasers with similar frequencies together and separates them equally along two paths with the same polarization.

The other lasers on the board are combined along two main paths with an array of dichroic mirrors. The 313 nm beam and the 423 nm beams are each split by two so that there is light from each in both paths. This beam setup at the optic table height can be seen in Figure 3.13.

One of the combined beam paths is directed to a reflective collimator which couples the light into a PCF[29]. The other path is sent in free space underneath the chamber where it is bounced up through the magnet bores and the trap assembly. On the radial side of

[27] NI PXI-6733
[28] Newport
[29] LMA-PM-10 from NKT Photonics

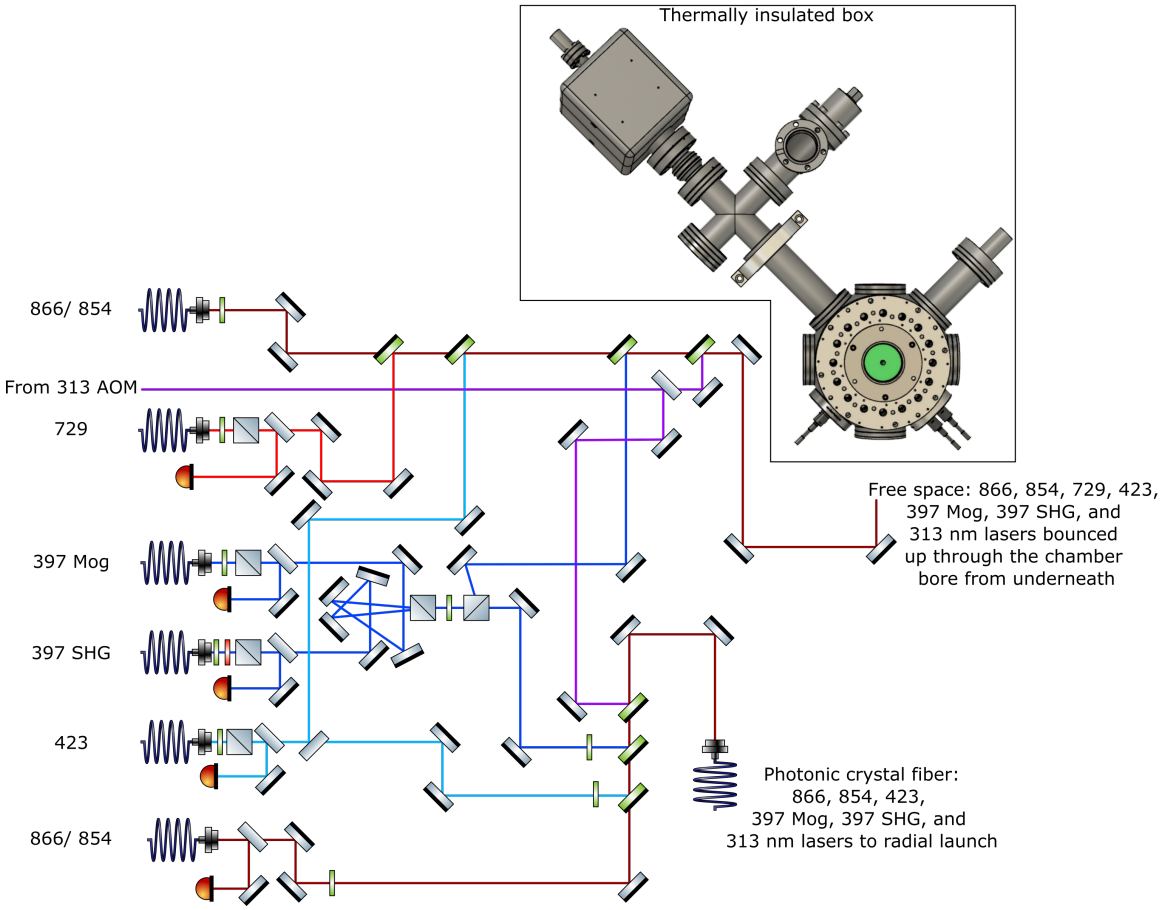


Figure 3.13: A diagram of the optics setup used to combine all the laser beams before entering the chamber. The beams are all combined with dichroic mirrors in two separate paths. One path is coupled into a PCF and will be sent into the chamber radially. The other path is combined and sent in free space underneath the chamber where it is reflected axially up through the chamber bore.

the chamber at the chamber height, another reflective fiber launch sends the output of the PCF to another dichroic mirror. It is combined with a free space 266 nm pulse laser before being focused into the chamber with a parabolic mirror. The optics at the chamber height are shown in Figure 3.14.

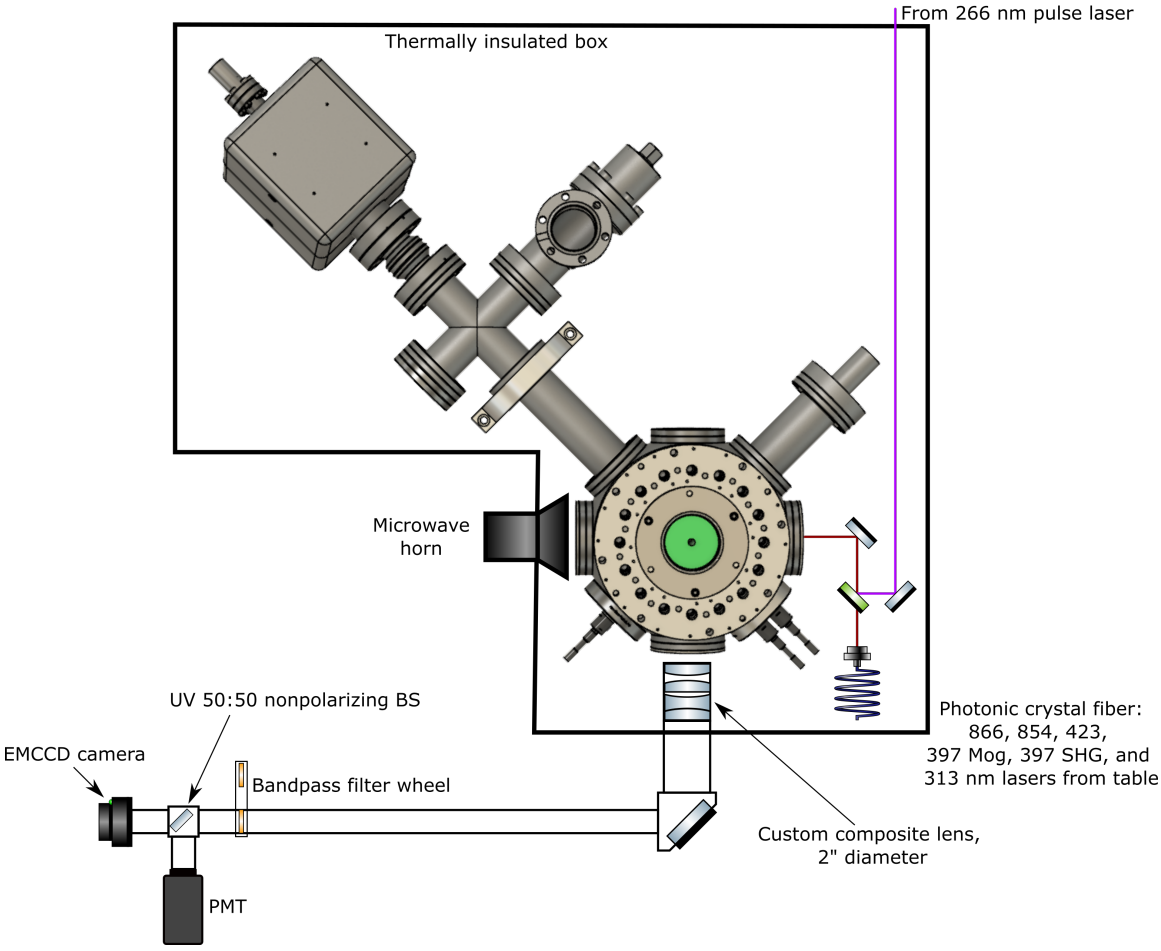


Figure 3.14: A diagram of the radial beam path at the chamber height. The radial imaging objective and beam path for the objective is shown.

The radial viewport between the electrical feedthrus conflat ports is used for imaging of the ions. A custom 2" diameter objective[30] was built to provide 8x magnification with a 4.42" distance to the ions. The objective has a back focal distance of 701 mm and was created with stock lenses[31], that were AR coated for 313 and 397 nm. The objective is mounted

[30] designed by Curtis Volin
[31] Thorlabs

to a rigid lens tube and a right angle mirror. This lens tube assembly is mounted to a 3-axis translation stage for precise translation of the objective for imaging of the ions. The mirror after the objective sends the image down to a camera and photon multiplier tube (PMT). A 50:50 beamsplitter directs half the light to an electron multiplying charge-coupled device (EMCCD) camera and half to the PMT. A filter wheel before the beamsplitter selects a bandpass filters around the ion fluorescence wavelengths.

## 3.5 Experiment Control

Figure 3.15 shows the schematic of the electrical and optical signals for controlling the experiment. In Figure 3.15, the RF signals can be seen as the red traces, the blue traces are analog voltage signals, the black are digital communications, and the green are optical signals sent via single mode fibers (fibers going to the experiment are polarization maintaining). The optical signals going to the chamber from each laser are omitted to clarify the diagram.

### 3.5.1 Control Software

The experiment is controlled via Igor Pro software. A framework was originally written by Kenton Brown, Jason Amini, and others for experimental control at GTRI. The system named 'IgorDAQGui' contains a list of core routines common to all experiments that setup and perform experiments. In order to perform the experiments the routines also include code to communicate with external hardware such as NI-DAQ hardware, arbitrary waveform generators, voltage sources, and GTRI-developed pulsers. The system is designed for deterministic timing alignment ($< 1ns$) between all the timing sensitive hardware for synchronous controls during experiments.

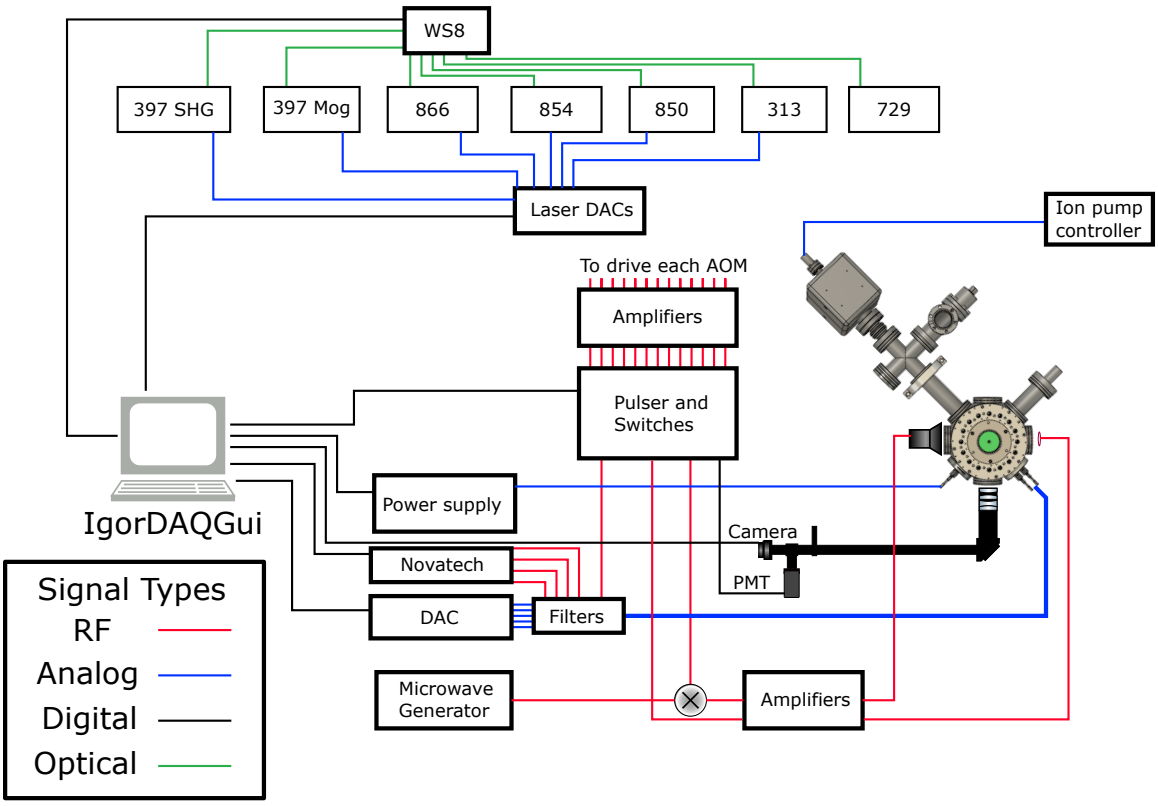


Figure 3.15: A diagram of the radial beam path at the ions height. The radial imaging objective and beam path for the objective is shown.

### 3.5.2 Clock Distribution and Pulsers

A GTRI-developed clock distribution box manages the timing for each 'pulser' in the system. The clock distribution box contains its own FPGA controller and dedicated circuit board. It takes in an 800 MHz clock and distributes the signal to a collection of front panel SMAs for connection to pulsers. It also has a bank of female RJ45 connectors for a connection to each pulser.

Each pulser contains a Kintex-7 FPGA[32] that programs a set of four AD9910 direct digitial synthesizer (DDS) chips and 12 transistor-transistor logic (TTL). Eight of the TTL are used for triggering external hardware, and four are dedicated to trigger internal RF switches for each of the DDS channels. On the back of each pulser box is six digital inputs for counting photons via digital pulses or for reading a clock signal to start triggering an experiment. Each pulser box requires a 800 MHz clock input SMA connection for a reference oscillator and a RJ45 connection for communication with the clock distribution box. One of the pulsers in a system is defined as the primary pulser in the Igor configuration code, the others are secondary. When a pulse program is started, a copy of the program is sent to each pulser configured and an experiment start trigger is sent from the primary pulser to the clock distribution box via the RJ45 connector. Then the clock distribution box sends out a synchronous trigger to all the pulsers telling them to execute their pre-programmed pulse programs.

### 3.5.3 DACs

The Penning trap system is paired with a set of three DAC PXI cards[33] mounted in half rack NI-DAQ chassis. Each card contains eight analog output channels. A custom breakout board attaches to the face of the chassis and breaks out the 24 analog output channels and an analog ground to a single DB25 connector. The breakout PCB also has an input

[32] Xilinx
[33] National Instruments PXI-6733

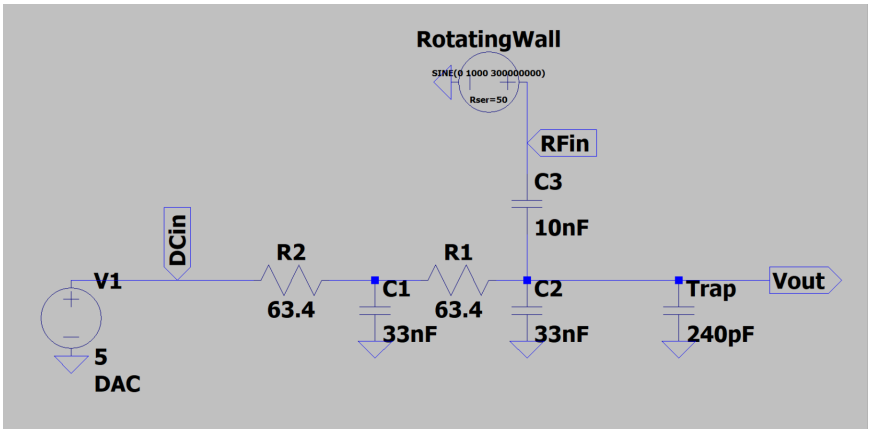


Figure 3.16: The schematic of a single DAC channel's filter circuit and included capacitively coupled RF signal.

for a waveform playback trigger which is sent TTL. Before a pulse program is run, the waveforms are calculated and uploaded into the memory on the DAC cards. Then, the TTL waveform trigger starts the play of the waveform at the appropriate moment once the pulse program is playing.

The output of the breakout board for the DAC channels is connected to a filter board. The filter board consists of a double poled RC filter for each of the 25 channels. For the experiments described in this thesis, most data was collected with filters of a frequency cutoff, $15.5$ kHz. This was created with resistors at $63.4\ \Omega$ and capacitors at $33$ nF. The trap electrodes have a capacitance to ground of $\sim 240$ pF.

Additionally, the board includes connections of apply capacitively coupled RF signals onto select channels. Signals are coupled via a $10$ nF capacitor. With this value, the signals are only attenuated by about $1/4.3$ due to the voltage divider formed by the added capacitor.

### 3.5.4 RF Controls

A microwave waveguide[34] is mounted on the radial viewport opposite the radial beam entry. It is pressed up to the conflat flange as close as possible for maximal transmission into the chamber. The frequency is generated by mixing a DDS channel output with a static

[34] Pasternack, WR-51, 15 to 22 GHz

microwave frequency synthesizer. This mixed signal is sent to a 3W amplifier before being sent to the waveguide for injection into the chamber. Due to cable losses at the high frequencies used ($16 - 19$ GHz), the power sent to the microwave horn was $< 2$ W.

The output of the each DDS from the pulsers are sent to digital switches, mixers for power locking, and finally RF amplifiers in order to saturate the AOM for maximal diffraction efficiency. Four phase synchronous DDS[35] output channels are sent directly to the capacitive couplers on the filter board for adding to each of the four ring electrode channels. This enables application of a rotating wall potential or an axialization potential for crystal manipulation. Additionally, one of the DDS channels is mixed down with a RF source[36] to generate low frequency RF signal for exciting the motional modes in a 'tickle' experiment. These techniques will be discussed in chapter 5.

[35]Novatech 409B
[36]SRS DS345

# CHAPTER 4

# ION TRAPPING IN A PERMANENT MAGNET PENNING TRAP

In this chapter, I detail the configuration for our calcium-40 ion loading procedure. Initial trapping faced a few problems which needed to be solved. I describe the laser parameters needed for stable trapping as well as the theory for the dynamics describing non-neutral plasmas. Two techniques, axialization and a rotating wall potential, are discussed and implemented in many of the experiments throughout the thesis. Finally, an upper bound on the radial ion temperature is measured using the electric quadrupole transition from the $^2S_{1/2}$ to $^2D_{5/2}$ state.

## 4.1 Calcium Loading procedure

In order to load calcium ions in the trap, the resistive oven is heated using $2.4$ A. After $\sim 3$ minutes, the oven has heated to the point of sublimating atoms. Then, the resonant $423$ nm laser is turned on with a power between $< 1\mu W$ to $1$ mW depending on the desired number of atoms loaded. The laser is stabilized to the cesium calibrated wavemeter so that it sits on resonance for the neutral calcium transition.

A second photon with wavelength $< 390$ nm then drives the excited electrons to an unbound state. Several different sources were used for this second photon, including a 375 nm laser[1], the 313 nm laser also used for beryllium Doppler cooling, a 355 nm picosecond ND:YVO laser[2] with $120$ MHz repetition rate, a 266 nm picosecond laser[3] at $50$ Hz repetition rate set to $\sim 60$ $\mu$J, and a multimode fiber coupled LED source at 385 nm[4]. One of these sources is overlapped at the trap location with the laser cooling beams and the 423

[1]Coherent OBIS
[2]Coherent Paladin
[3]Ekspla PL2231
[4]Thorlabs M385FP1

nm, first-photon ionization laser.

Loading a selective number of ions is achieved by tuning the power of the 423 nm laser and the second step beam using the DDS amplitude control or optical attenuators. Loading small numbers of ions is challenging and requires turning on the photoionization lasers for just the right amount of time, usually $\sim$ 1s with very low powers. This is done with a trial and error routine. If the wrong number of ions is loaded in the trap, then all ions are forcibly ejected and the process is repeated again. This ion removal process is performed by setting one of the endcap electrodes to $10$ V and the other to $-10$ V to create a potential ramp making the ions' axial motion unconfined. This potential is held for $\sim$ 1 s before returning to the normal quadrupole trapping potential. We have never seen this ramping technique fail to eject ions.

The trapped ions are detected by running an 'ion monitor' continuous experiment routine. In this experiment, the ions are Doppler cooled and a few simple measurements are taken. A 'dark' background measurement is collected by turning off the 866 nm repumping laser while detecting scattered photons. Then a 'bright' measurement is made by collecting scattered photons with all the Doppler cooling lasers tuned to resonance during a counting period of $500$ $\mu$s to $10$ ms. The number of ions in the trap can be determined with the camera image and/or via total PMT counts.

The loading procedure is commonly performed with the ion monitor experiment constantly running for observation of newly trapped ions. Usually ions do not appear in the trap for $10$ s up to $10$ minutes. When the sublimated atoms are initially created they can have temperatures closer to the melting temperature of calcium. The trap depth is of order several electron volts which is large enough to trap any of these hot ions, however they may be created with very large magnetron orbits. At temperatures approaching the calcium

melting temperature, the Doppler shift is very large

$$\begin{aligned} v &= \sqrt{2k_B T/m} > 600 \text{ m/s} \\ \mathbf{k} \cdot \mathbf{v} &= \frac{2\pi}{397 \times 10^{-9}} 600 > 2\pi \times 1.5 \text{ GHz} \end{aligned} \tag{4.1}$$

where $\mathbf{v}$ is the velocity of the ion, $k_B$ is Boltzmann's constant, $T$ is the temperature, $m$ is the mass of a calcium atom, and $\mathbf{k}$ is the wavevector of the 397 nm photon.

Additionally, the cooling resonance is broadened due to the temperature distribution of the ions. The FWHM of the broadened resonance is

$$\Delta f_{FWHM} = \sqrt{\frac{8k_B T \ln 2}{mc^2}} f_0 \tag{4.2}$$

where $c$ is the speed of light and $f_0$ is the transition frequency. For the parameters of the hot ions mentioned above, $\Delta f_{FWHM} = 2.8$ GHz. However, the ions are rotating in and out of the laser beam, so the angle between $\mathbf{k}$ and $\mathbf{v}$ is constantly changing which changes the magnitude of the shift. In practice, the changing Doppler shift causes the cooling to be very inefficient after initial loading. Thus, it can take several minutes for the ions to cool and crystallize into the trap center. This process can be sped up by moving the cooling laser radially away from the trap center and slowly walking it back to the center, by repeatedly sweeping the cooling frequency down by the estimated magnitude of the Doppler broadening, and/or application of an axialization drive.

## 4.2 Initial Ion Trapping

The first trapping attempts to trap in a Penning trap weren't immediately successful. Several challenges hindered the attempts which weren't initially realized. The first was a short between trap electrodes which pulled the trapping location much lower than the physical center of the trap. In addition, multiple dark resonances exist in the cooling scheme which complicate laser cooling. The laser frequencies have to be tuned to ideal positions in order

to avoid dark resonances in the cooling. The high field environment makes the cooling profile more complicated [91, 92].

In order to simplify initial trapping of calcium ions, we first trapped in a Paul trap. The RF potential was created using a resonant circuit built onto a perforated circuit board. The circuit was attached at the chamber flange, where the circuit resonance allowed for a $2.71$ MHz sinusoidal drive with a peak-to-peak potential of $500$ V. Trapping was first observed in this configuration at $\sim 3$ G by placing a $25$ mm diameter ring magnet near the vacuum chamber.

The field was then increased by moving the magnet closer to the trap center until the fluorescence decreased. At this point, the cooling was reoptimized for the new field strength. This procedure was repeated several times until the magnet could not be moved any closer.

At several points during the field strength walk, the resonance of the magnetic field-sensitive neutral calcium frequency was measured using neutral spectroscopy. The resonance and values for the cooling laser parameters at that magnet position were recorded. This effectively builds a look-up table (LUT) for the laser frequencies at each magnetic field strength.

In order to trap with a new magnet, its position is adjusted to maximize neutral calcium fluorescence which tunes the field strength to match the LUT entry. Then the trapping parameters for the lasers can be reused for that LUT point.

The process is continued with two magnets until the field strength matches the desired Penning trap field strength. The radial cooling laser beam is spatially offset by about one beam waist to apply the necessary torque for Penning trap cooling [93]. At this point, the RF amplitude can be ramped down for trapping in a Penning trap similar to [28].

### 4.2.1 Laser parameters

In order to cool the ions in the Penning trap, energy needs to be removed from the cyclotron mode, but added to the magnetron mode. This can be achieved by offsetting the radial

cooling beam from the trap center so that it travels along the same direction as the ion magnetron rotation [93, 94]. This creates the necessary laser intensity gradient at the trap center to cool the cyclotron mode and heat the magnetron mode.

### 4.2.2 Plasma Dynamics and Cloud Shape

The ion cloud is a non-neutral plasma so plasma dynamics can be used for estimates of the density and cloud shape. After reaching thermal equilibrium, the ions rotate in a rigid configuration with rotation frequency, $\omega_r$. In the limit of low temperature/ small Debye length, the density is approximately uniform. The Debye length is defined as

$$\lambda_D = \sqrt{\frac{\epsilon_0 k_B T}{n_0 q^2}} \tag{4.3}$$

where $\epsilon_0$ is the permittivity of free space, $k_B$ is Boltzmann's constant, $T$ is the ion temperature, and $n_0$ is the density [95]. The density of the ion cloud depends on the rotation frequency,

$$n_0 = \frac{2\epsilon_0 m\omega_r(\omega_c - \omega_r)}{q^2} \tag{4.4}$$

where $\epsilon_0$ is the permittivity of free space, $m$ is the mass of of the ion, $\omega_c = qB/m$ is the cyclotron frequency, and $q$ is the ion's charge [96].

The plasma frequency is defined by [95]

$$\omega_p^2 = \frac{q^2 n_0}{\epsilon_0 m} = 2\omega_r(\omega_c - \omega_r). \tag{4.5}$$

The shape of the ion cloud is determined by the square of the ratio of the axial frequency to the plasma frequency. The cloud forms spheroidal shapes with an aspect ratio $\alpha = z_0/r_0$. For $\alpha > 1$, the cloud is a prolate spheroid. The cloud is stretched in the axial direction

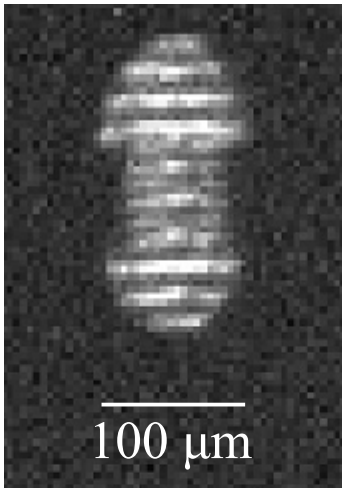


Figure 4.1: A picture of $^9Be^+$ trapped in an prolate spheroid shape. The dark discontinuities around the middle section are impurity ions with larger charge-to-mass ratios.

making a cigar shaped form. The prolate spheroid form is described by

$$\frac{\omega_z^2}{\omega_p^2} = \frac{1}{\alpha^2 - 1}\left[\frac{u_p}{2}\ln\left[\frac{u_p + 1}{u_p - 1}\right] - 1\right] \tag{4.6}$$

where $u_p = \alpha/(\alpha^2 - 1)^{1/2}$ [96]. An image of a beryllium crystal in a prolate spheroid shape is shown in Figure 4.1.

In the other limit $\alpha < 1$, the cloud forms an oblate spheroid. The cloud is stretched in the radial direction forming more of a pancake shape. It can be described by

$$\frac{\omega_z^2}{\omega_p^2} = \frac{1}{\alpha^2 - 1}\left[u_p \tan^{-1}\left[\frac{1}{u_0}\right] - 1\right] \tag{4.7}$$

where $u_0 = \alpha/(1 - \alpha^2)^{1/2}$ [96].

At the maximum aspect ratio, $\alpha$, the cloud hits the Brillouin limit [97, 95, 98]. This occurs at $\omega_r = \omega_c/2$ with a maximum density of $n_B = \epsilon_0 m\omega_c^2/2q^2$. At this limit, it is possible to have a 1D axial string of ions [99].

The Coulomb-coupling parameter is used to describe the plasma ion interactions [95].

$$\Gamma = \frac{q^2}{4\pi\epsilon_0 a_s k_B T} \tag{4.8}$$

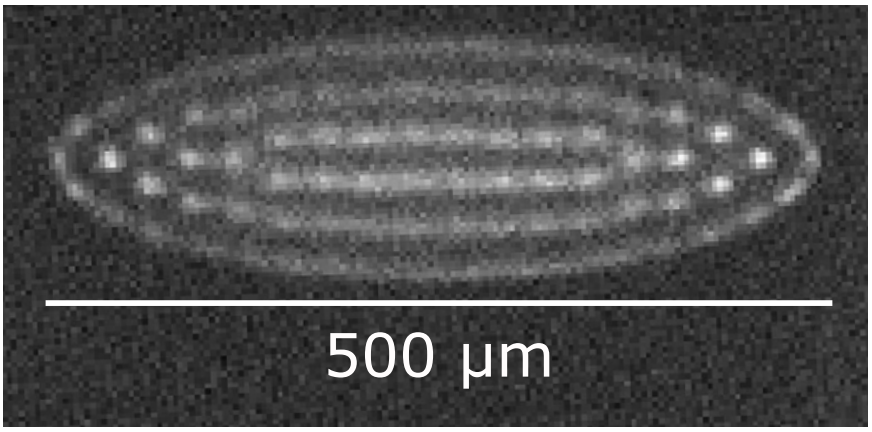


Figure 4.2: A side view camera image of a crystallized 3D $^{40}Ca^{+}$ crystal in an oblate spheroid shape.

where $a_s$ is the Wigner-Seitz radius. The Wigner-Seitz radius is determined by the plasma density $a_s^3 = 3/4\pi n_0$. For values of $\Gamma < 1$, the plasma is in the weak coupling regime (gas-like). For values of $\Gamma > 2$, the plasma is strongly coupled and behaves like a liquid. A phase transition occurs at $\Gamma \sim 175$, where the plasma becomes solid-like forming a Coulomb crystal [100]. An example of such a crystal is shown in Figure 4.2. In order to form this crystal, the axial beam alignment needs to be perfectly perpendicular to the radial direction.

### 4.3 Axialization and Rotating Wall

Axialization was used in many of the experiments performed in this thesis. The technique involves the application of a weak radial quadrupole drive to the ring electrodes which couples the magnetron and modified cyclotron modes [101, 102, 101]. One electrode and its mirror opposite across the trap center are driven with a phase, $0°$. The other pair of electrodes are driven with a phase at $180°$. The RF drive is applied at the sum of the magnetron and modified cyclotron frequencies, which is the bare cyclotron frequency. The coupling of the two modes creates a periodic energy exchange and provides a means for simultaneously reducing the energy of both modes with Doppler cooling. This can be seen directly by the increase in fluorescence and the shrinking of the spatial extent of the ion

cloud. An analytic treatment of laser cooling with an axializing field can be found in [103]. The technique was applied to a Penning trap with calcium ions and the damping rate of the magnetron motion was measured in [104].

Commonly, the ions in a Penning trap are stabilized by application of the offset laser beam. The beam is typically offset by a distance equal to the beam waist. For most of our experiments, this amounts to $15 - 30$ $\mu$m. The laser provides the necessary torque to keep the ions in stable orbits. Another way to apply torque to keep the trapped ions stable is to use a 'rotating wall' potential [105, 106, 107, 108, 109]. Similar to the axialization potential, a RF drive is applied to the ring electrodes with varying phases for the different ring segments. A quadrupolar potential is applied to the ring electrodes to generate the rotating wall. The asymmetry of the potential breaks the symmetry of the crystal and forces the crystal to rotate at the same frequency.

A radial cooling laser beam is usually used to stabilize the ion rotation. The laser beam balances the torques due to static field errors, asymmetries, and collisions. However, the result is a higher in-plane temperature for equilibrium. An applied rotating wall potential provides a sink for the energy added by the laser beam which can lower the overall in-plane temperature [105]. In Torrisi et al. (2016), they characterize the in-plane equilibrium temperature for various cooling beam parameters with the applied rotating wall [105]. They found that the optimal laser detuning for cooling the ions depends on the ion crystal rotation frequency and beam waist. However, the Doppler cooling limit can be reached for a range of laser beam parameters and crystal rotation frequencies.

## 4.4 Calcium Ion Temperatures

In order to characterize the radial temperature of the ions, a narrow linewidth optical transition was used. The 729 nm electric quadrupole transition drives the transition from the $S_{1/2}$ to the $D_{5/2}$. By scanning the laser frequency using an AOM, we can measure the Doppler broadened linewidth. In the axial direction, the ion motion is determined by the

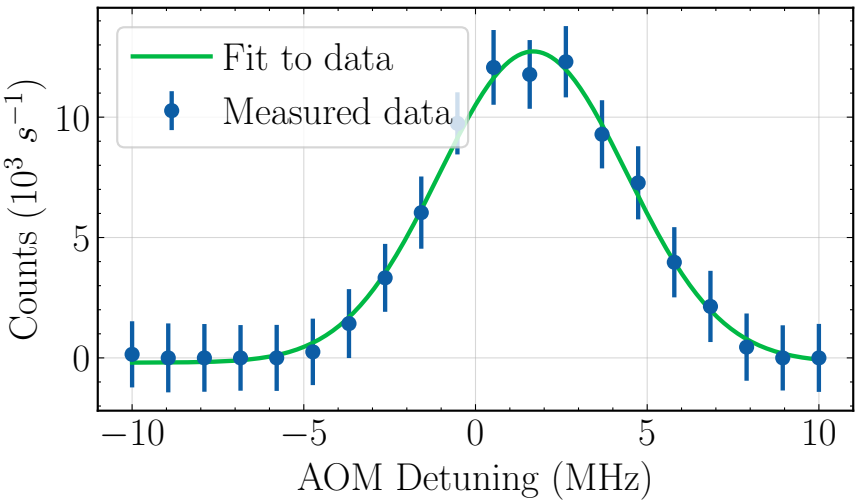


Figure 4.3: Early frequency scan over the 729 nm transition and a fit to the data. The 729 entered the chamber radially for this measurement. A Gaussian was fit to the data because the peak width is thermally limited. The fit returns a FWHM of $6.3(1)$ MHz.

harmonic trap potential. Thus, we should see sidebands of the motion determined by the ion's temperature. In the radial direction, the motion from the magnetron and modified cyclotron will also appear as sidebands on the carrier. Given the Doppler limit for Calcium is $\sim 0.5$ mK, the motional occupancy of each mode can be calculated. For each mode with a frequency, $\omega$,

$$\bar{n}\hbar\omega = \frac{1}{2}k_B T \tag{4.9}$$

where $\bar{n}$ is the average motional occupancy, $k_B$ is Boltzmann's constant, and $T$ is the temperature. For these parameters in our trap with about $6500$ G field, calcium ions have motional occupancies of $> 100$ quanta. The magnetron motion cannot be treated the same way because of its negative contribution to the total energy.

Initial measurements of 729 nm transition were performed radially and enabled an upper bound to be placed on the in plane temperature. The measurement is not an exact measure of the ion temperature due to two effects. First, the magnet positions were not entirely compensated, so any magnetic field gradient across the cloud would appear as a broadening and decoherence mechanism. The second is due to the large Doppler shift from the rotational motion. Therefore, the radial transition width can be used as an upper bound

for the temperature.

A Gaussian was fit to the data because the peak width is not Fourier transform limited by the pulse time, but limited by the ion temperature. The fit returns a FWHM of $6.3(1)$ MHz. The Doppler broadened FWHM is described by

$$\Delta_{\text{FWHM}} = \sqrt{\frac{8k_B T \ln 2}{mc^2}} f_0. \tag{4.10}$$

where $k_B$ is Boltzmann's constant, $T$ is the temperature, $m$ is the mass of calcium ion, $c$ is the speed of light, and $f_0$ is the transition frequency. The FWHM corresponds to a temperature of $3.3(1)$ mK. Therefore, the radial ion temperature is $< 3.3(1)$ mK.

# CHAPTER 5

# MAGNETIC FIELD CHARACTERIZATION

In order to verify the stability and trap characteristics for precision quantum control, the permanent magnet's field needed to be studied. The first magnetic field measurements were performed using neutral atom spectroscopy. After initial trapping, the mode frequencies were measured and used to calibrate the magnetic field. We detected the spatial magnetic field gradient by transporting small crystals of trapped ions in the trap region and interrogated the ground state microwave transition. Finally, long term temporal field measurements were made using the microwave transition. This chapter details each of the magnetic field characterizations performed.

## 5.1 Neutral Spectroscopy

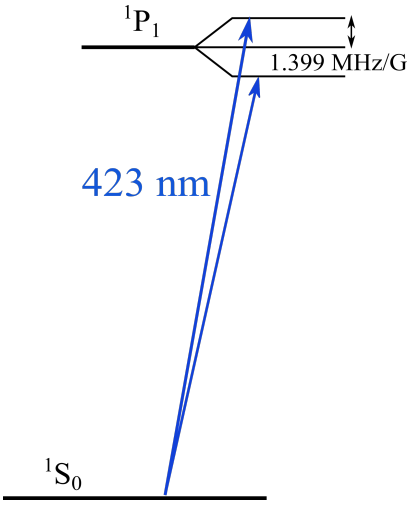


Figure 5.1: A diagram of the neutral transitions used for performing magnetic field measurements.

Neutral spectroscopy was first used in each trap configuration to calibrate the magnetic field. The calcium oven current is set to $\sim 3$ A, which is slightly higher than the normal

current used for loading, $\sim 2.4$ A. This increases the neutral atom flux through the trap region. Along the same axis as the neutral flux, the camera objective collects photons around the neutral calcium wavelength. A radial 423 nm laser beam resonant with the neutral $^{40}$Ca S-to-P transition is sent perpendicular to the flux axis. Thus, the Doppler broadening of the hot thermal atoms can be minimized due to the mostly perpendicular velocity vector. Additional filtering of the atoms with parallel velocity components is done by using spatial filtering of the image to select the atoms in the center of the trap region (i.e. where their velocity components are most perpendicular to the laser's k vector).

There are three transitions due to the Zeeman splitting of the P state: a magnetic field insensitive transition and two field sensitive ones with opposite field strength as seen in Figure 2.4. If a frequency scan is performed over each of the field sensitive transitions, the centers values can be fit. Any Doppler shift due to the parallel component of the atom's velocity will appear as an identical frequency shift for each of the S-to-P transitions. Thus, we can subtract the frequency measurements of the $m_J = +1$ and the $m_J = -1$ to remove the Doppler shift. The resulting frequency is twice the magnetic field spacing for one of the states, $f_{+1} - f_{-1} = 2g_J\mu_B B/h$.

In order to perform these measurements, the laser was frequency stabilized to a WS8 wavemeter which is calibrated to a cesium atomic reference. The frequency scans were performed using a DDS controlled AOM with stabilized total power. The accuracy of this wavemeter is 2 MHz, and is the dominant error source for these measurements.

This technique was also used to make a magnetic field profile. The 423 nm laser beam fiber collimator is mounted to a translation stage, and the camera is mounted to its own translation stage. They can be translated together up and down by a known amount. The field measurement experiment then can be performed at each location to create a map along the trap's z-axis.

Figure 5.2 shows the plot of the magnetic field along the z-axis for magnet configuration C using this technique. A fit was performed to the data which returned a magnet spacing of

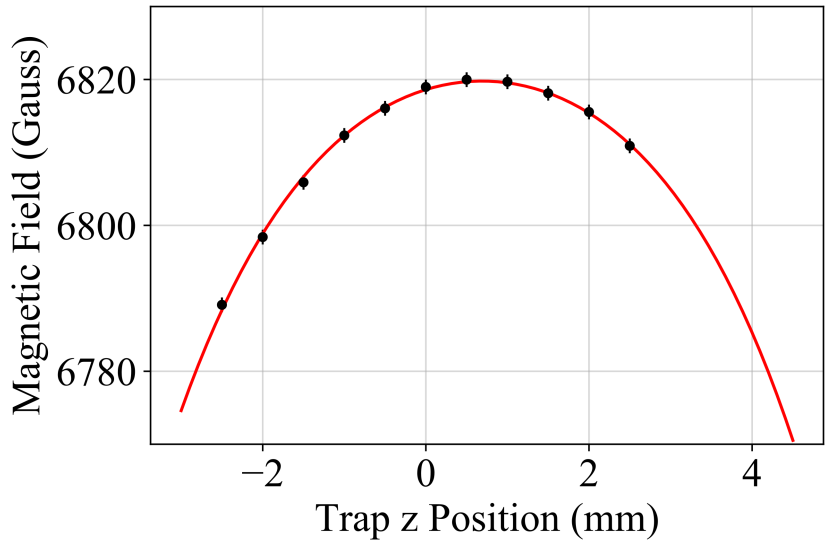


Figure 5.2: A field map of the magnetic field using the neutral spectroscopy technique. Black points show the data and error bars, while the red line shows the fit result.

$26.9(1)$ mm. The magnets spacing was then corrected using non-magnetic shim stock and then the data was recollected; shown by the points in Figure 5.3. The data was fit which returned a value of $30.0(1)$ mm, which is within error of the optimal spacing, $30$ mm.

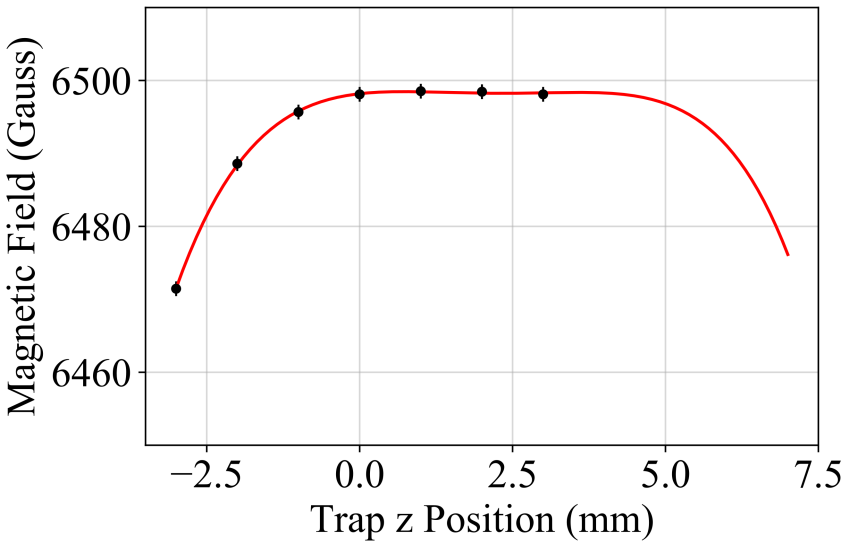


Figure 5.3: A field map of the magnetic field using the neutral spectroscopy technique. Data taken after shimming the magnet spacing.

## 5.2 Field Calibration from Motional Frequencies

The magnetic field can also be obtained from the bare cyclotron frequency, $\omega_c = qB/m$. In a Penning trap, the cyclotron frequency isn't one of the motional frequencies, but it is related to the measurable motional frequencies through the BGIT. The theorem states that the sum of the squares of the motional frequencies is the square of the cyclotron frequency, $\omega_m^2 + \omega_+^2 + \omega_z^2 = \omega_c^2$. Thus, a measurement of these frequencies is a measure of the magnetic field.

The frequencies can be measured by applying a RF drive to one of the trap electrodes. When the frequency of the applied drive is resonant with the motional frequency, energy is added to the system in that mode. The hot ions have energy that is much higher than the equilibrium Doppler temperature. The resonant heating of the trapped ions can be directly detected as a decrease of fluorescence. If too much energy is added to the ions motion, they can be driven out of the trap region.

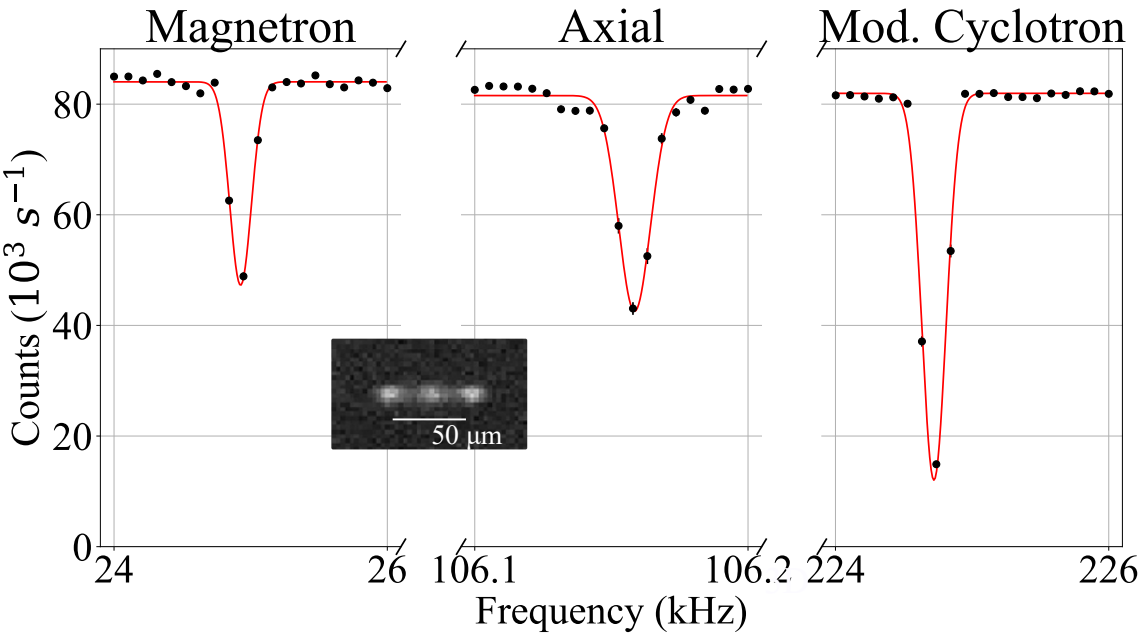


Figure 5.4: Measurements of the three motional frequencies. The inset image is of the ions used for these measurements [1].

Figure 5.4 shows fluorescence measurements of the ions after applying the scanned RF

drive frequency. Each scan was fit to a Gaussian whose center values returned the mode frequencies: a magnetron frequency of 24.926(28) kHz, an axial frequency of 106.159(3) kHz, and a modified cyclotron frequency of 224.721(24) kHz. Application of the BGIT calculates a cyclotron frequency of 249.781(2) kHz, or equivalently, a magnetic field of 6500.27(6) G. This agrees with the data taken for the z=0 trap position in Figure 5.3 within 2 Gauss. Given the temperature sensitivity of the NdFeB material, $0.12\%$ $K^{-1}$, a field shift of this magnitude could be caused by a magnet temperature drift of $260$ mK. A shift of this magnitude is reasonable, because the data was taken on different days. Temperature effects are discussed further in section 7.3.1.

## 5.3 Field Calibration from Zeeman Spin Flip

Another method for field measurement is to measure the Zeeman splitting in the ground state of the calcium ion. However, these states are still part of the Doppler cooling transition, so a method of state dependent detection is needed. Because of the large motional occupancy of the ions at the Doppler limit, they are not in the Lamb-Dicke regime. Thus, coherent high fidelity 729 nm transitions are not possible due to temperature limitations. Instead, a 393 nm Doppler cooling technique was implemented to enable state detection without shelving.

### 5.3.1 393 Laser Cooling

The 393 nm laser cooling scheme uses a single 393 nm laser to perform Doppler cooling from the $m_J = -1/2$ in the $S_{1/2}$ state to the $m_J = -3/2$ in the $^2P_{3/2}$ state. This transition is closed other than the decay to the metastable D-states so it only uses a single UV laser. However, selection rules for the $^2P_{3/2}$ state decay show that the ion can fall into any of 5 metastable levels in the D-states, in particular the states shown with repump laser tones drawn in red of Figure 5.5.

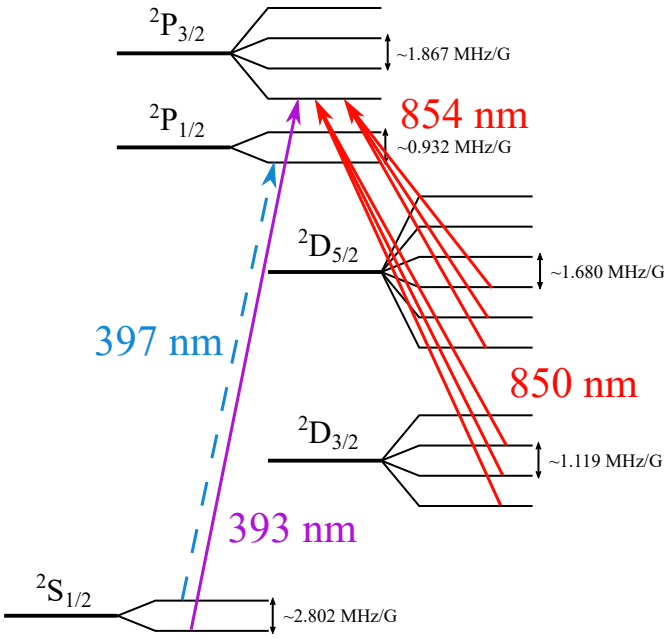


Figure 5.5: A level drawing of the relevant states and lasers used for 393 nm laser cooling.

These states are repumped directly back into the cycling transition. Only two repump lasers are used, at 850 nm and 854 nm. Each laser has a fiber EOM for generation of the necessary spectral components to keep the ion in the cycling transition.

Unfortunately, each repump laser requires $\pi$-polarized light in order to keep the ions in the cycling states. Those repump tones must enter the trap in the radial direction in order to have a polarization parallel to the magnetic field direction. This spatial requirement reduces the cooling efficiency because of the narrow radial region where these beams propagate. In addition, each of the repump tones can form dark resonances with the 393 nm laser. This complicates the Doppler cooling profile and reduces the overall cooling performance.

By scattering photons from only one of the ground Zeeman states, we can perform state detection without the need for a shelving laser. This scheme does result in an imbalance of ground state population in steady state but is somewhat tunable via the location and configuration of the repump laser tones.

The use of EOMs for the repump laser tones also generates higher order frequency components. All the EOM spectral components have a probability of off-resonant scatter-

ing into one of the other Zeeman states in the $^2P_{3/2}$ level. Some of these components move populations into undesired excited levels which then decay into the dark ground state. We also implement a 397 nm state preparation and repump laser for the transition between $m_J = +1/2$ in the $^2S_{1/2}$ state and $m_J = -1/2$ in the $^2P_{1/2}$ state. This laser is not strictly necessary for cooling, however, it clears the population falling into the dark ground state from off-resonant scatter of the IR repump tones. This laser can also be used to populate the ground state, $m_J = -1/2$ when used with the repump lasers. However, only an imbalance of the ground state populations is necessary to be able to perform a detectable transition between them.

The ground state transition can be driven directly via application of microwaves into the vacuum chamber. A waveguide with mounted horn is directed into the chamber via the viewport opposite the radial cooling beam. At our given field strength, the transition frequency is about $18$ GHz. At this wavelength ($\sim 17$ mm), the trap electrodes effectively shield the ions from the microwave radiation, massively attenuating the transmitted signal. Simulations of microwave propagation through the trap region agree with this prediction.

### 5.3.2 Transport Enabled Zeeman Measurements for Field Mapping

Because of the use of static trap fields, the trap center is defined by the electric quadrupole field center in the magnetic field. This trap center can be easily moved around by changing the potential applied to the electrodes. In our trap configuration, the four ring electrodes can be biased to push the trap well to arbitrary positions in the x-y plane. The endcap electrodes can be biased to push the trap center along the z-axis of the trap. This allows for transport of the ions to arbitrary trap positions without any sort of RF driven heating. Transport is possible to a large accessible volume around the geometric trap center is $\sim 10$ mm$^3$. Although each transport operations used in this experiment occurred over $1$ ms, the transport could be made much faster, order of $< 100$ $\mu$s. The potential applied to the electrodes is converted to a trap position by a measured scale factor. To calibrate the scale

factor, the ions are transported in the y-direction (in the plane of the camera focus) by a given amount. The distance traveled is measured using the cameras pixels. The pixel size and magnification ratio are known, so the transport scale factor can be calculated.

This transport operation was used to perform magnetic field mapping between the magnets. In this scheme, a spin flip transition is measured at different trap positions to measure a spatial field profile. In this experiment, the ions are first Doppler cooled and state prepared. Then they are transported to the field measurement location in the trap using 100 waveform steps with a step duration of 10 $\mu$s. This breaks up the total travel distance into 100 steps. A microwave pulse is gated and then the ions are transported back to the nominal trapping location for state detection.

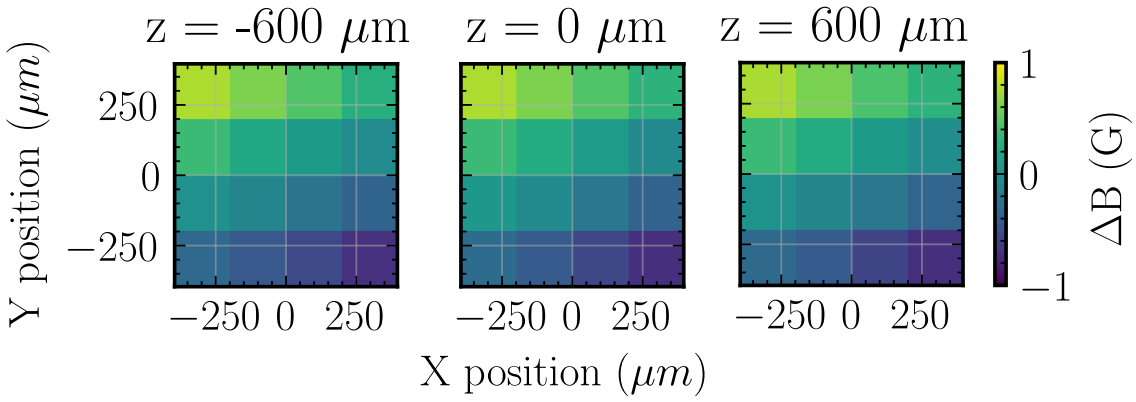


Figure 5.6: Color map images of magnetic field measurements for points in the x-y plane at three different z positions.

Using transport, 2D field gradient maps were generated for three different z positions, $z = 0, \pm 600$ mm, as seen in Figure 5.6. In order to perform the measurements, the transport protocol described above is used to measure the field at each location. Between each successive data point, the magnetic field was recalibrated at the nominal trapping location. This location corresponds to the center of the middle plot in Figure 5.6, coordinate $(x = 0, y = 0, z = 0)$. A diagonal gradient of $< 2$ G can be observed in the data. A gradient of this magnitude is likely due to a mismatch in the concentricity of the magnet pair, which is an error that can be corrected for by translation of one magnet with respect to the other.

This data was taken with magnet configuration D.

In order to find the magnetic field center of magnet configuration D, frequency scans of the magnetic field were collected for y positions and then for a collection of x positions. When the scans were taken, the magnets were believed to be too close together. Thus, the theoretical field at the magnetic field center should be at a local minima. The local minima was found, and a final frequency scan was performed at this location to calibrate the field and estimate the field inhomogeneity, as shown in Figure 5.7.

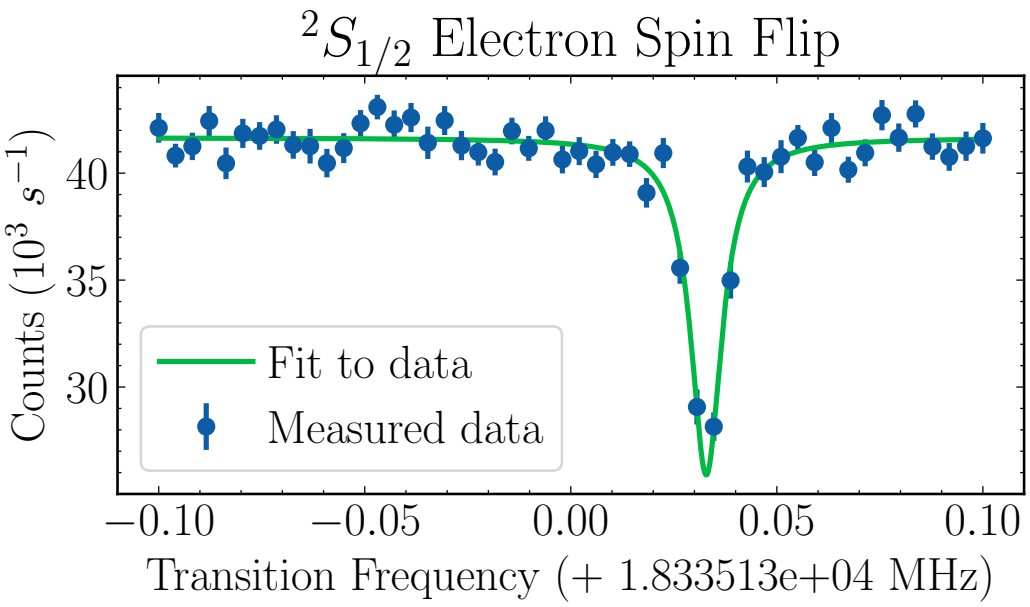


Figure 5.7: Measurement of the Zeeman spin flip in the ground state of $^{40}Ca^+$ at the found magnetic field center.

A Lorentzian fit to the dataset shows a frequency measurement of $18335.1677(2)$ MHz. The magnetic field is related to the transition frequency by

$$B = \frac{h\nu}{\mu_B \Delta m_J g_J} \tag{5.1}$$

where $h$ is Planck's constant, $\nu$ is the transition frequency, $\mu_B$ is the Bohr magneton, $\Delta m_J = 1$ is the change in total angular momentum's z-projection, and $g_J$ is the Lande g-factor for the $^2S_{1/2}$ state. Using the current best measured value for the calcium ground

state g-factor, $g_J = 2.00225664(9)$ [74], the calculated magnetic field is $0.65426488(3)$ T. The error from the Lorentzian fit to the data in Figure 5.7 is $12$ ppb, which is $\sim 4$x smaller than the error for the best precision measurement of the g-factor, $45$ ppb [74]. Thus, the total standard deviation reported for the field measurement is dominated by the tabulated constant instead of the experiment, at $47$ ppb.

### 5.3.3 Temporal Stability

The magnetic field temporal stability was also measured using the Zeeman transition. Over a period of two days, the ions were constantly interrogated and the field measured. The values were recorded and saved. Post-processing was implemented on the dataset to calculate the Allan deviation and Hadamard deviation[1]. The plots are shown in Figure 5.8.

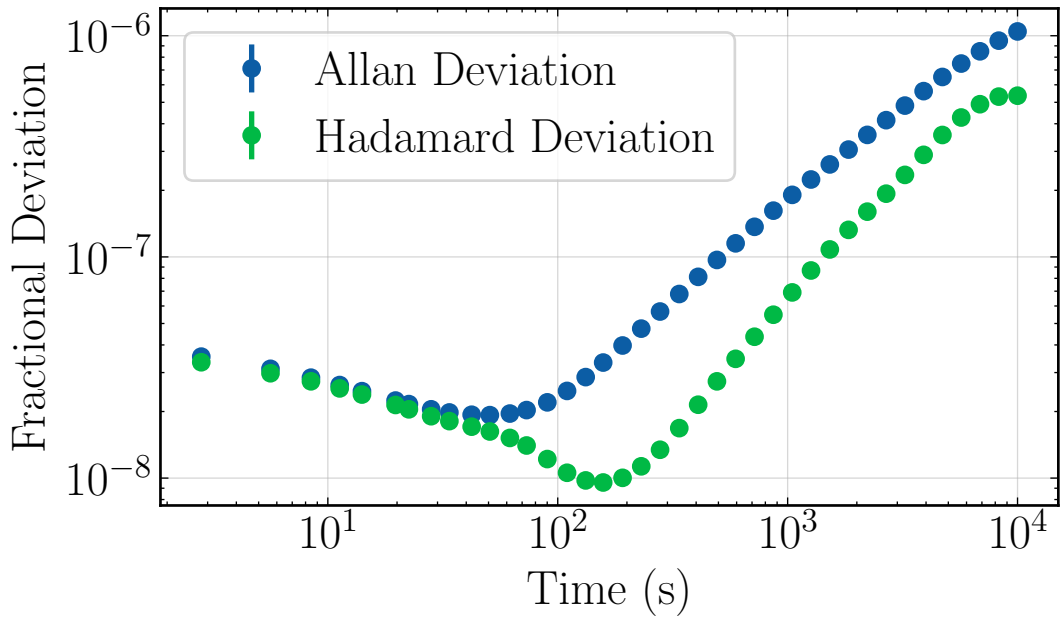


Figure 5.8: A plot of overlapping Allan and Hadamard deviations for data from the magnetic field measurement of the Zeeman spin flip in the ground state of $^{40}Ca^{+}$.

The Hadamard deviation is a useful measure of the stability because it is insensitive to linear drift. The data shows a minimum fractional deviation, $< 10$ ppb, of the magnetic field measured at an averaging time of $150$ s. These measurements were made using only

[1]The overlapping forms of these deviations were used.

passive thermal insulating foam surrounding the vacuum chamber; no magnetic shielding was used.

## 5.4 Summary

This chapter demonstrates the characterization of the trap's magnetic field. Initially, we characterized the magnetic field using mode frequency measurements. For magnet configuration C, the field curvature was measured using neutral spectroscopy and then corrected based on the predicted gap error from a fit to the data. With magnet configuration D, we were able to measure spatial gradients by probing the ground state Zeeman splitting. The trap center is defined by the trap electrode voltages, thus the ions can be transported to any arbitrary location in 3D space achievable by the DAC output voltage range. The magnetic field center was found by minimizing the width of the ground state transition. The measured ground state splitting at this location was found at the $12$ ppb level for a small crystal, $< 100$ $\mu$m in diameter. The stability of the magnetic field over time was evaluated by measuring the transition frequency repeatedly over two days. A lowest Hadamard fractional deviation of $< 10$ ppb was found for averaging times of $\sim 150$ s. These measurements validate the technology as an apparatus well suited for precision quantum experiments. Further improvements to the system will be discussed at the end of chapter 8.

# CHAPTER 6
# BERYLLIUM ION TRAPPING

In this chapter, I detail the first trapping of beryllium ions in our system using our oven design and ovens from NIST. The beryllium ions can be co-trapped and sympathetically cooled with pre-trapped calcium ions. Alternatively, they can be directly Doppler cooled alone in the trap. Finally, I discuss the reaction rate problem of beryllium ions in comparison to calcium ions.

## 6.1 $^{9}Be^{+}$ Loading

The procedure for loading beryllium ions in the trap is similar to the procedure used for loading calcium. A resistively heated oven is turned on by conducting a current through the oven. The GTRI blunderbust style oven was activated with $9$ A, while the NIST oven is heated to sublimation with only $0.9$ A. After a period of about $10 - 20$ s, the oven is heated sufficiently for a loading attempt. At this point, the $266$ nm picosecond pulse laser ($50$ Hz), co-aligned with the radial cooling beam, is manually gated into the vacuum chamber using Ekspla's computer control interface. The near resonance of two $266$ nm photons with the ionization threshold, makes the process reasonably efficient [81]. The pulse energy was measured for this loading configuration at about $20 - 30$ $\mu$J. The beam size was measured at the ions using a pick-off optic placed right before the chamber vacuum window. This allows the laser beam sizes in the co-aligned beam to be measured and the overlap verified at the ion position. A beam waist of $\sim 50$ $\mu$m was measured for the laser.

The beryllium ions are created throughout the trap diameter along the beam path. They start with large kinetic energies due to the large sublimation temperature of beryllium. Thus, the newly created ions start with large orbits and are not localized or cold. Using the same analysis for the kinetic energy that was performed for hot calcium we can calculate

the Doppler shift and broadening. If we assume a hot beryllium ion temperature slightly below its melting temperature, $1560$ K [110], and all its kinetic energy directed parallel to the cooling laser direction, then the velocity and Doppler shift are

$$\begin{aligned} v &= \sqrt{2k_B T/m} > 1600 \text{ m/s} \\ \mathbf{k}\cdot\mathbf{v} &= \frac{2\pi}{313\times 10^{-9}} 1600 > 2\pi \times 5 \text{ GHz} \end{aligned} \tag{6.1}$$

The FWHM of the broadened resonance at this temperature could be as broad as $9.1$ GHz. However, the trapped ions will have a range of kinetic energies due to the Boltzmann distribution and are likely much colder due to sublimation at lower sample temperatures. In practice, the very slow cooling process is aided by the small background gas pressure at room temperature. The ions are able to be collected after about $10-20$ minutes. The collection and cooling process, referred to as a modified 'spin-up', is performed by moving the radial cooling beam radially outward towards the edge of the trap by $> 0.5$ mm. Then, the beam is slowly moved radially back towards the center of the trap cooling the ions as they are collected. This collection procedure can only be performed after the ions have sufficiently cooled enough to have significant interaction with the cooling laser.

Empirically, we have seen that the ions can be collected immediately after performing the loading procedure by detuning the cooling laser by $-600$ MHz before turning the pulse laser on. After turning off the oven and pulse laser, the cooling laser is returned to the optimal cooling detuning, $\sim -10$ MHz from the Doppler resonance. At this point, the ions rapidly cool and coalesce into the trap center. We typically observe that only a small number of ions from all the ions in the trap needs to be cooled and collected for the process to rapidly cool all others. The Coulomb coupling to the other ions helps cool the others within a matter of seconds. The -600 MHz detuning used corresponds to $\sim 7^\circ$ angle between the ion velocity and laser k-vector, under the assumption that the ions are near the beryllium melting temperature.

## 6.2 Beryllium Co-trapping

One other scheme was used for quickly cooling and collecting the beryllium ions. This involved using the calcium ions as a sympathetic coolant species. In this process, calcium ions were loaded into the trap and continuously cooled. Then, the beryllium loading process was performed. The calcium ions act as an infinite heat sink for the hot beryllium ions as they are created in the trap, because the Doppler cooling lasers constantly remove excess energy from the system. The Coulomb force between the species acts to cool the ions rapidly to meet an equilibrium with the trapped calcium. Thus, the beryllium ions coalesce to the trap center without the need for a spin-up procedure.

Because of the lighter mass of beryllium ions, the ions have larger motional frequencies than calcium and collect in the center with the heavier calcium surrounding the beryllium. Due to this effect, smaller charge-to-mass ratio ions will always move to larger radii compared to a larger charge-to-mass ratio species.

The imaging system utilizes bandpass filters around the scattered wavelengths for detection for each of the trapped species. Thus, only a single species can be detected at a time. The wavelength dependence of the index of refraction (313 nm for beryllium ions and 397 nm for calcium ions) of the fused silica objective lenses requires different positions for imaging each species of trapped ions. The beryllium ions are imaged $4.12$ mm closer to the chamber than the calcium ions imaging position. So swapping detection between the two species simply requires rotation of a filter wheel to select the proper filter and translation of the objective to properly image the ions. Figure 6.1 shows the images of a co-trapped $^{9}Be^{+}$-$^{40}Ca^{+}$ ion crystal with the camera imaging the calcium and beryllium separately.

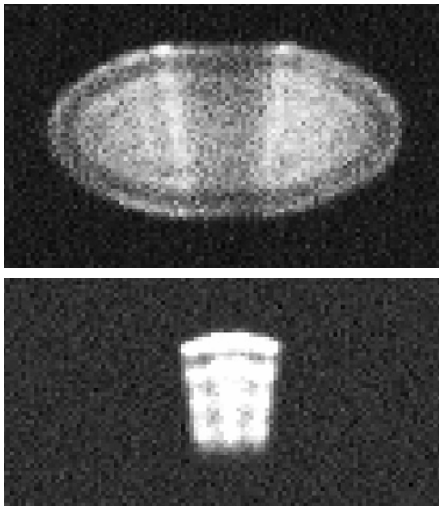


Figure 6.1: Camera images of co-trapped calcium and beryllium ions in the same crystal. Each image was taken by swapping the filters in the image path and translating the objective position to match the chromatic shift of the focus.

## 6.3 Beryllium Ovens

### 6.3.1 GTRI Beryllium Oven

The first attempts for beryllium ion trapping were performed with a GTRI blunderbust style resistive oven as described earlier in the thesis. The first trapped beryllium ions were observed using this oven. However, this process quickly became unstable. The oven was only able to load a single ring of beryllium ions before collection of dark ions poisoned the trap. After loading a small quantity of beryllium ions, we observed the beryllium ion orbits grow more and more unstable in time. This decay of stability was observed in the few minutes following the end of the loading procedure. The behaviour became worse with repeated loading attempts before eventually we were not able to load beryllium at all.

The picosecond nonresonant multiphoton ionization procedure is not isotope selective. The peak power of the pulses is large enough to photoionize many other atoms or molecules. The high temperature of the blunderbust beryllium oven needed for sublimating beryllium atoms likely could evaporate or sublimate other materials out of the oven body or surrounding mount. The background pressure of the chamber increases when this load-

ing procedure is performed from below the pressure gauge readout resolution, $< 3 \times 10^{-11}$ Torr, and climbs by orders of magnitude; this observation agrees with the prediction of oven heated outgassing. These atoms then freely traverse the trap region where they are ionized by the picosecond laser pulses and remain trapped with the Doppler cooled calcium and/ or beryllium. The growth of the dark region inside the calcium ion ring determines that the trapped ions of lower charge-to-mass ratio have been cooled into the trap. Lack of 313 nm fluorescence verifies that the trapped ions are not beryllium. Thus, the instability of trapped beryllium from the beryllium blunderbust oven could be the result of cotrapping with larger numbers of dark ions.

In addition, the existence of a background gas loading rate from the pulse laser was measured. Starting with a sample of trapped calcium ions, the pulse laser was gated into the chamber with energies from $5 - 50$ $\mu$J for a duration of $10 - 20$ s without heating of either oven. Ions with lighter charge-to-mass ratio than calcium were observed to cool into the center of the trap pushing the calcium outwards. However, for the lower pulse energies approximately equal to the energies used for beryllium ionization, the dark ion production rate was lower than the beryllium ionization rate. Therefore, the pulse laser can be used for loading small numbers of beryllium ions before the background gas ionization process begins to fill the trap.

### 6.3.2 NIST Beryllium Oven

After observation of the failed blunderbust style oven, we replaced the oven with one from the NIST Ion Storage Group as described in subsection 3.3.2. This oven implementation uses significantly less material for the oven and outgasses much less when operated. Most of the beryllium data collected in this thesis used this oven. With this implementation, initial trapping became much more stable. Dark ions from loading appeared only in the trap due to the background gas loading rate.

## 6.4 Beryllium Reactions

Like the other species used for ion trapping, beryllium ions readily react with many atoms and molecules. At this point, the ion no longer has the same internal structure and no longer will be cooled with the same laser systems. In a clean, baked vacuum system the dominant background pressure of the chamber is hydrogen. Unfortunately, diatomic hydrogen reacts with beryllium and calcium ions to form hydrides. Coincidentally, the vibrational lines of $CaH^+$ overlap with the Doppler cooling wavelength, $397$ nm [111]. Therefore, whenever $CaH^+$ is produced via reaction with background gas, it is immediately dissociated with the Doppler cooling laser beams.

The beryllium hydride ion however has a vibrational structure that puts its lowest energy transition ($\sim 255$ nm) well below its Doppler cooling wavelength. Thus, $BeH^+$ isn't dissociated and further reacts to a stable molecule, $BeOH^+$. The reaction rate of the trapped ions happens readily when the electron is in the P-state, which means that it happens when the beryllium ions are scattering $313$ nm photons. The reaction process limits the stability of longer term measurements as the number of dark ions grows and the signal-to-noise ratio of the remaining ions decreases. If $BeH^+$ can be dissociated before it reacts, then the reaction loss mechanism can be mitigated [112]. Perhaps application of the proper lasers to the ions could remove this problem altogether so that the beryllium ions trap lifetime is significantly longer, like it is for calcium ions. This is technically demanding, because the photodissociation wavelength is in the deep-UV, and requires an expensive frequency doubled laser system to implement.

## 6.5 Doppler Cooling Beryllium

To Doppler cool beryllium, a single laser cooling scheme is used. Frequency scans of the $313$ nm laser over the cooling resonance reveal ion temperatures near the Doppler limit. The frequency scan shown in Figure 6.2 shows the data taken from an axial 313 nm cooling

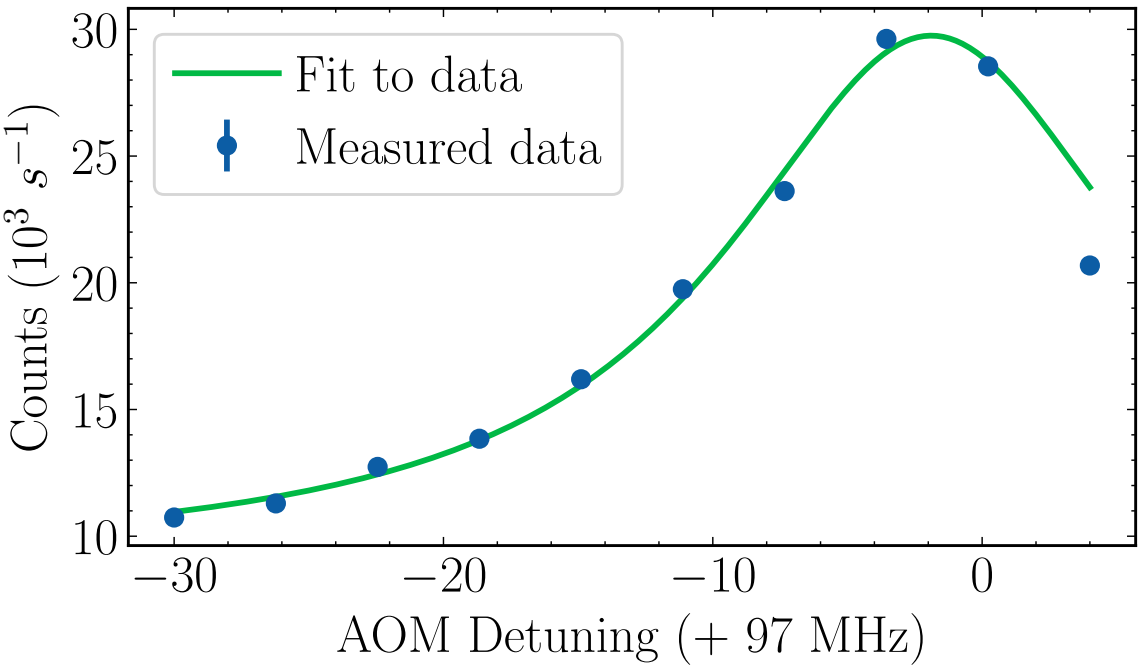


Figure 6.2: A frequency scan of the 313 nm laser over the Doppler resonance while being sympathetically cooled with calcium ions.

beam with sympathetic cooling from calcium ions. A fit to the data shows a FWHM of $18.6(7)$ MHz, which is about equal to the standard Doppler limit for beryllium at $19.6(2)$ MHz [82]. The points on the right-hand side of the resonance show an asymmetric decrease in population due to the heating that occurs from the blue-detuned detection. Thus, the fit does not use the last data point.

## 6.6 Summary

In summary, we have trapped beryllium ions and co-trapped them with calcium ions. Co-trapping allows for potentially less reactions of the beryllium ions with background gas, because Doppler cooling can be delegated to the co-trapped species. However, the efficiency of cooling is not ideal due to the large mass difference between the two species. Despite a sympathetic coolant, the reaction process is still a problem.

# CHAPTER 7

# MEASURING THE BERYLLIUM ION GROUND STATE TRANSITIONS

The final chamber iteration, configuration D, was used for most of the data taken with beryllium ions. At the nominal trapping location, the field was approximately $0.6540$ T. The same microwave horn described for calcium spectroscopy was used to send microwaves into the trap region. In order to address the beryllium nuclear spin transitions ($\Delta m_J = 0,\ \Delta m_I = 1$), a single loop of coil was created with $\sim 2$ cm diameter to use as an RF emitter for frequencies near $300$ MHz. A tunable resonant circuit was made[1] for optimal impedance matching to the resonant coil loop. In other experiments, the RF signal was directly applied to one of the trap electrodes (not impedance matched to a resonant circuit).

For convenience, each of the hyperfine structure states of the S-manifold are renamed with a number starting from 0 for the lowest energy state and continuing successively upwards. This naming convention is used in this chapter for brevity and clarity. A diagram of the states and their corresponding labels is shown in Figure 7.1.

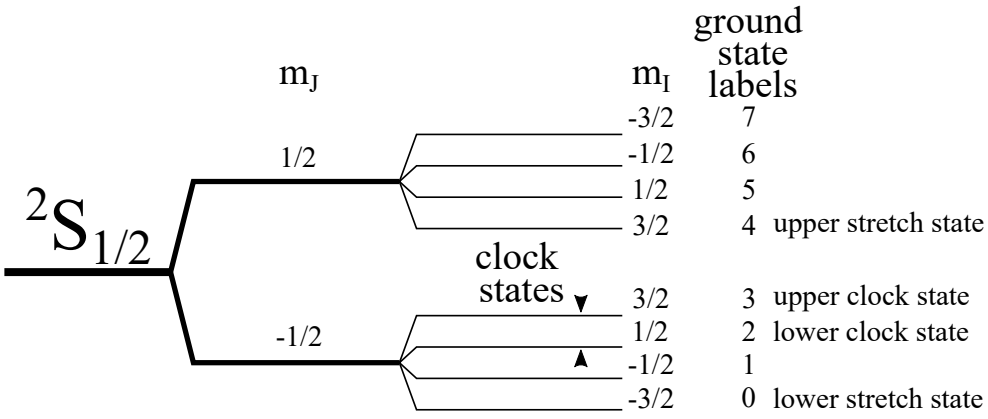


Figure 7.1: A diagram of the ground state hyperfine structure relabeled by increasing energy using integers starting from 0. Thus, the levels can be denoted "GS#" where GS is short for ground state and # is the number of the state. The two stretch states used for Doppler cooling and the two clock states are shown.

[1] by Brian Sawyer

In the S-manifold of the beryllium ion, there are the two stretch states which can be used for Doppler cooling, GS0 and GS4. The hyperfine clock transition nearest to our current field value is the transition between GS2 and GS3. Thus, in order to reach one of the clock states, the ion needs to be prepared. We identify three techniques for performing this state prep.

1. Using a coherent microwave pi transition to move the population to state 3 from the cooling state 4.

2. Make two, pi transitions from the lower stretch state, state 0, in order to climb the ladder of levels and reach the lower clock state.

3. Population can be prepared by an electric dipole allowed state preparation laser tuned to the $m_J = 1/2$ state of the $P_{3/2}$ manifold from the Doppler cooling ground state 4. An electron excited by this laser can decay its starting position in the ground state GS4 or to the upper clock state, GS3. The upper clock state is detuned from the state preparation laser by the microwave ground state splitting, so the population will build up in the upper clock level in steady state. This technique is shown in Figure 7.2.

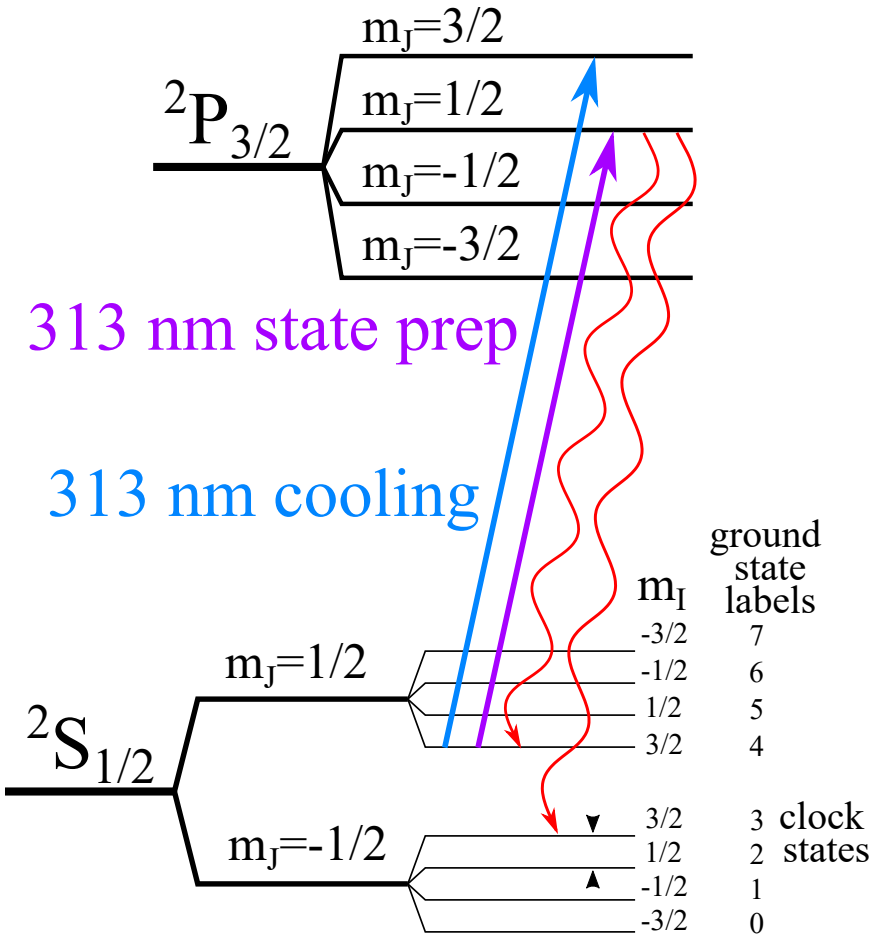


Figure 7.2: A diagram showing the states and optical transition used to prepare the upper clock state (GS3). The red lines show the two possible decay paths.

### 7.1 Beryllium Microwave Transitions

In order to prepare GS4, the microwave transition was measured. In order to calibrate the transition frequency, the beryllium ions are first Doppler cooled. Because beryllium Doppler cooling only involves two levels, the process naturally provides state preparation. Then, a microwave pulse is performed for a given gate time, frequency, and power. Finally, a detection event is performed during which the Doppler cooling laser is tuned to the resonant transition and the number of photons scattered during this time are counted. Due to the large detuning of the laser light from depopulating GS3, detection can be performed for a few milliseconds without significant off-resonant repumping of the population in the

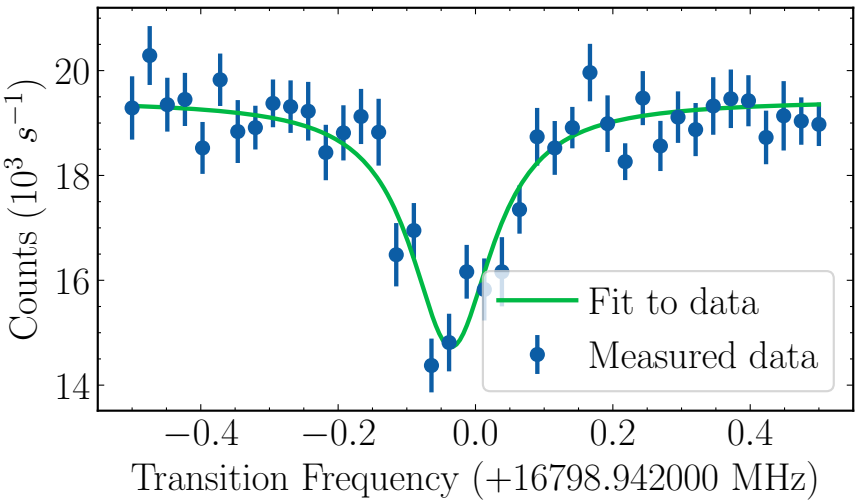


Figure 7.3: A microwave transition from the upper stretch state (GS4) to the upper clock state (GS3). The Lorentzian fit to the data reveals a transition frequency of $16798.907(6)$ MHz with a transition width of $70(10)$ kHz.

dark state. Thus, only the population left in GS4 will fluoresce upon detection measurement. After detection, GS3 is repumped by leaving the cooling light on for $\geq 10$ ms. If this experiment is repeated for various values of microwave frequency, the transition can be mapped. Figure 7.3 shows a microwave frequency scan over the transition resonance between GS4 and GS3.

In order to determine the repumping time from GS3, the repumping duration is varied after performing a microwave pulse to maximize GS3 population. Then, the ions are detected for a shorter amount of time. Figure 7.4 shows this time scan for population left in GS3. The dataset is shifted right by $2$ ms in order to represent the $2$ ms detection's effect on the repumping. For the parameters of the system in this experiment, a $2$ ms detection time is reasonable to minimize off-resonant repumping and $10$ ms is long enough to repump a significant fraction of the population. An exponential fit to the dataset reveals a time constant of $4(1)$ ms.

The quality of the microwave spin flips are degraded by a couple of factors. The effective aperture of the trap electrodes at the narrowest point is $2$ mm in the radial direction and $> 6$ mm in the vertical direction. If we treat the aperture cutoff the same as for a

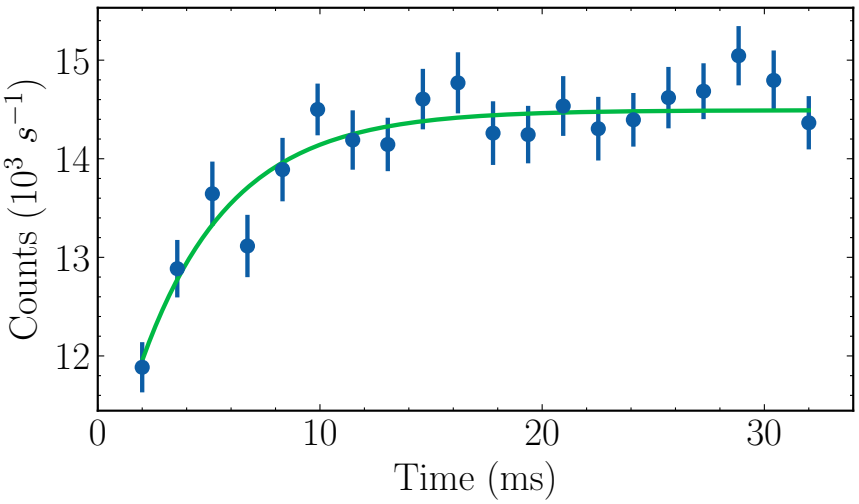


Figure 7.4: The bright population (GS4) after performing a microwave pulse (to GS3) and repumping for varied times. An exponential fit to the dataset reveals a time constant of $4(1)$ ms.

cylindrical waveguide, then the cutoff wavelength can be calculated, $f_c = c/(2d)$, where $c$ is the speed of light, and $d$ is the dimension. The narrow dimension of the trap aperture corresponds to a cutoff wavelength of $> 74$ GHz and the taller dimension corresponds to a cutoff wavelength of $\sim 30$ GHz. Luckily, the aperture of the trap is not a waveguide, however, all of the microwaves used for spanning the ground state spin flip in calcium and beryllium ($f < 20$ GHz) are heavily attenuated ($> 30$ dB).

The diffraction from the aperture can be characterized in either the far or near field regime. The far field regime for the radiation is determined by distances $> 2D^2/\lambda$, where $D$ is the larger dimension of the waveguide and $\lambda$ is the wavelength [113]. The trap radius is an order of magnitude greater than the regime boundary, so the diffracted microwaves are in the far field regime. However, the cylindrical diameter of the trap region is only slightly bigger than a half wavelength. This might predict some sort of standing wave structure. In the experiment, we find that the amount of radiation that the ions see is highly dependent on the horn position. Some variation of microwave field strength was also measured across the trap region; the Rabi rate varied by factors of $2 - 3$x.

Additionally, the fidelity of the spin flips in the beryllium ions are degraded due to the

magnetic field gradient as shown in earlier chapters. By sitting at the magnetic field center, most of the first order gradient can be removed. Nonetheless, some residual magnetic gradient remains. The larger the crystal used for the experiment, the larger the inhomogeneity that will be sampled. Each ring within the ion crystal will then have a different Rabi frequency. For large crystals, the average over all the ions during detection will appear as a exponentially decaying sine wave.

Unless otherwise noted, the data shown in this chapter was taken at the magnetic field center as found with the narrowest microwave transition in calcium (Figure 5.7). In order to access this trap region the ions must be transported to this location before any gates are performed. At this translated position ($r > 1$ mm), the co-trapped calcium will no longer be Doppler cooled and thus the beryllium no longer sympathetically cooled. Imbalanced torques and background gas collisions will begin to spin the cloud down (cloud expands). Due to the weakened microwave strength, longer gate times are needed to observe population transfer, but longer times also allow for more ion expansion. This is another mechanism for sampling a magnetic field gradient. For a typical microwave pulse of length $5-10$ ms and a cloud rotation frequency of $70$ kHz, the ions complete $350-700$ orbits about the trap center. If the field the ions sample is varying during each rotation due to static magnetic field inhomogenity and a changing ion radius, then decoherence is expected.

## 7.2 Beryllium Hyperfine Transitions

In order to characterize the nuclear transitions, the nearest transitions to the stretch states were probed. This includes the transition between GS4 and GS5 for the upper stretch state, and the transition between GS0 and GS1 for the lower stretch state. The transition frequencies are all calculated at the given field strength by diagonalizing the matrix describing the Hamiltonian contributions of similar magnitude (See chapter 2 for details section 2.4). This allows us to create a look-up table for all the ground state transitions. Thus, by measuring one of the transitions (for example one of the microwave transitions), the field strength can

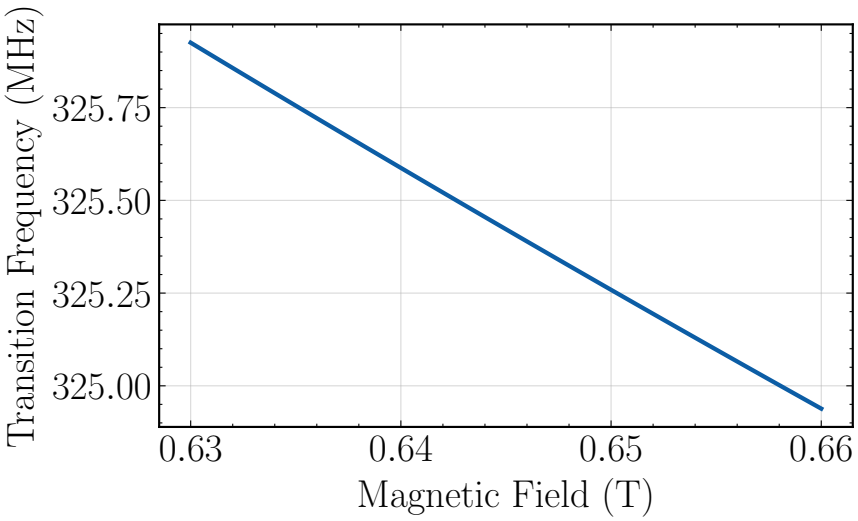


Figure 7.5: A plot of the nuclear transition frequency from GS4 to GS5 for magnetic field strengths around the trap field.

be found and the locations of the other transitions predicted. Additionally, this characterization also provides the information to calculate the sensitivities of each state at a given field strength. An estimate of the transition's center frequency drift can be estimated for the magnetic field strength change. For our trap magnetic field magnitude, the transition from GS4 to GS5 has a sensitivity of $-320$ kHz/G. Figure 7.5 shows a plot of the transitions frequency near the trap's magnetic field.

Most of the data that was taken used the coil loop circuit created by Brian Sawyer. The coil loop was placed in one of the vacuum windows such that optical access was not occluded. However, the signal strength seen by the ions varied greatly for different coil positions. This is likely the result of either signal pickup on the chamber electrical connections or changes to the heat dissipating off the coil and circuit components. We empirically found that better Rabi rates were obtained when the coil loop was in contact with the chamber. By placing the circuit in contact with the chamber, the coil loop had a large heat sink (the chamber itself). However, when the loop wasn't effectively dissipating the heat, large temperature spikes of the components pulled their values away from the intended design. This lowered the q-factor and ultimately shifted the narrow circuit resonance, which effec-

tively attenuating the emitted signal.

We also tried to directly connect the RF to one of the trap electrodes. Using a capactively coupled circuit identical to the tickle drive connection, the amplified RF output was connected after the filter board to an electrode. This resulted in similar Rabi rates for the nuclear transitions as for the resonant coil, albeit with most of the power reflected back to the amplifier. The capactively coupled design reflected most of its power due to poor impedance matching. However, the closer proximity to the ions, apparently compensated for this fact resulting in similar interaction strength. With these two methods, nuclear transition pi times were observed to be $2.5 - 5$ ms.

The nuclear transitions were driven directly using a DDS channel that was amplified by a 50 W amplifier[2]. The amplifier output was then connected to either the coil loop or the trap electrode circuitry. For some cable positions of the signal line, other electronics in the lab picked-up noise from the signal. Most notably, the control pulser box was picking up noise and causing experiments to crash when the timing alignment circuits between pulsers became too noisy to maintain synchronicity. Other experiments in the lab also noticed noise on feedback lines for stabilizing lasers. Thus, care was taken to minimize the amount of ambient signal in the lab by adding layers of shielding to the cables and optimally placing the cables away from other electrical signals.

[2]Minicircuits ZHL-50W-52-S+

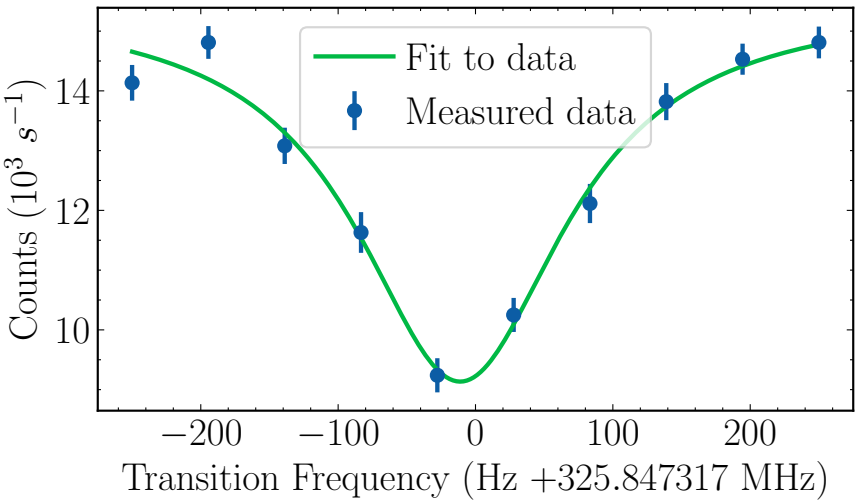


Figure 7.6: The Doppler fluorescence after performing a RF pulse for various frequency on the coil loop. This scan measures the transition between GS4 to GS5. The Lorentzian fit to the data calculates the resonant transition frequency at 325.847306(5) MHz with a fit width of 180(30) Hz. This agrees with the Fourier limit of the pulse time, 5 ms.

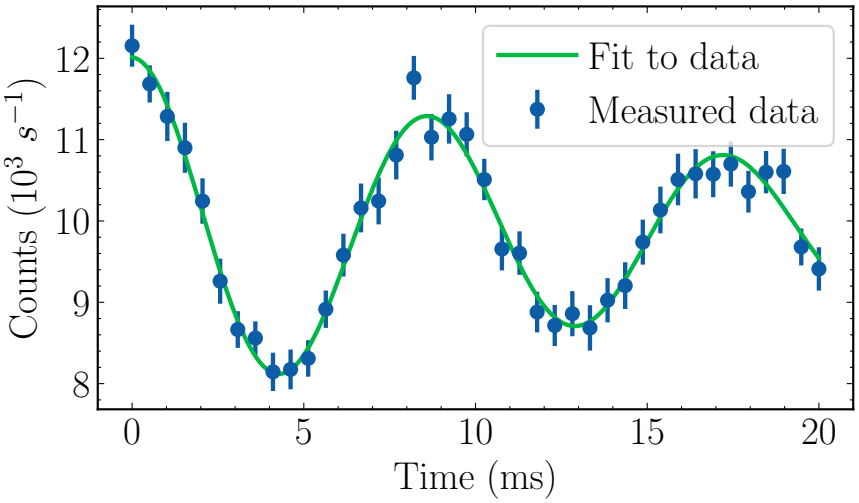


Figure 7.7: The Doppler fluorescence after performing a RF pulse for various durations on the coil loop. This scan measures the transition between GS4 to GS5. Data is fit to a decaying sinusoid, and the fit values calculate a pi time of 4.33(2) ms with a decay rate of 48(6) $s^{-1}$.

The experiments addressing the hyperfine structure transitions involving only change of the nuclear spin required significantly longer repumping times than are needed for repumping states with the same nuclear spin. Additionally, the Doppler laser needs to scatter photons changing the nuclear state and decay to the correct ground state. This multiple-step

process has a lower probability of occurring, and thus takes longer to occur. The combination of these effects result in measurements like shown in Figure 7.8. The experiment procedure used for the data in Figure 7.8 is the same as the repump scan shown (Figure 7.4) except for the use of the RF coil instead of the horn for the gate transition. An exponential fit to the data in Figure 7.8 gives a repump time constant of $36(6)$ ms. Most experiments using the non-clock state nuclear states used a repumping time of $50$ ms in order to balance signal and experiment duty cycle.

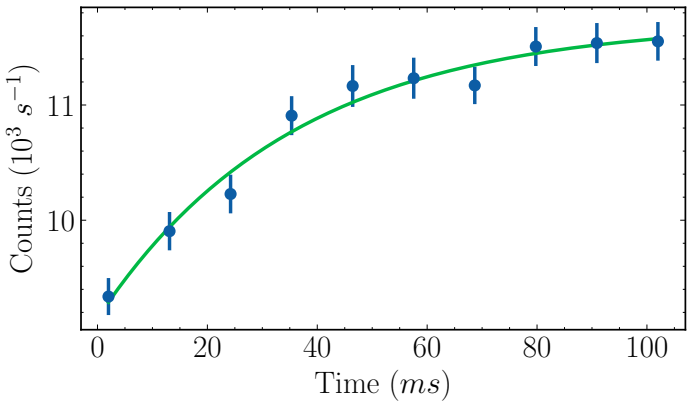


Figure 7.8: A scan of the ion fluorescence after repumping the ions out of the dark GS5 for a scanned repumping duration. The ions were prepared by performing a resonant pi pulse as calibrated from the frequency fit from Figure 7.6. The gate time was $4$ ms. An exponential fit determined a time constant of $36(6)$ ms.

The long repump time also gives an advantage. It allows for implementation of a cooling step after the gate but before detection in order to recollect any ions that have begun to spin out. The Doppler cooling laser beams are the same that are used for repumping. Thus, if the population of the ions isn't entirely in the dark state, some cooling can be performed for a shorter duration than the repump time. This is a significant help to recycle as much signal as possible after any heating/ spin-out from the long gate time and transport duration where no sympathetic cooling is taking place. This cooling collapses the superposition state created by the resonant RF transition, but this is unimportant if the populations of the two states are ready to be measured. We refer to this post-gate, pre-detection cooling as recooling.

### 7.2.1 Clock State Measurements

Climbing a ladder of states to reach the clock states was technically difficult with magnetic field fluctuations due to varying magnetization from magnet temperature fluctuations and external field noise. Calibrations for the most field sensitive transitions would drift between experiments. These lead to imperfect nuclear and microwave transitions; specifically leaving population at each level along the way. Thus, we needed multiple high fidelity RF population transfers in order to reach the clock state. In order to circumvent these problems, a state preparation laser tone was produced via the second sideband from an EOM[3] on the cooling laser. The excited state for this transition in the $P_{3/2}$ is the $m_J = 1/2$ level. Thus, the state preparation light needed to be pi polarized to induce a transition where $\Delta m_F = 0$. This means that only the fraction of the radial 313 nm laser beam with polarization components parallel to the magnetic field can perform the state preparation. This level can then decay back to the same state or to the upper clock state, GS3. The decay pathways are the red curved lines shown in Figure 7.2 and the state preparation laser tone is denoted with a purple arrow. Due to the inefficient repumping out of the clock state, the population there should buildup quickly without significant off-resonant scatter from the cooling laser. Simple rate equation simulations for this process agree that it should provide state preparation.

Clock state measurement experiments involve only one additional step than the experiments used for the other nuclear transitions. First, both ion species are Doppler cooled in the trap, and the beryllium ions are automatically prepared into their stretch state. Then the state preparation EOM is turned on for an adequate amount of time ($300\ \mu$s) to prepare the ions in the upper clock state. The ions are transported to the magnetic field center to minimize field inhomogenity. The RF clock pulse is performed for the designated power and duration. Then the ions are returned to the nominal trapping location where they are recooled for a duration long enough to recollect after any spin-out ($10 - 20$ ms for the clock),

[3] Qubig EOM, 6.1 GHz resonance, AR coated for 313 nm

but short enough to avoid repumping back to the cycling transition. Finally, detection is performed ($2.5-5$ ms) before the ions are repumped with the cooling laser light ($100-200$ ms) to prepare for the next experiment.

In order to verify the state preparation of the upper clock state, an experiment was performed where state preparation was implemented for various times and laser frequencies. Then, the nuclear transition between the GS4 and GS5 was measured. Any residual population left in the upper stretch state will make a transition to GS5 when the nuclear transition frequency is resonant with the GS4 to GS5 transition. Using this technique, the state preparation was optimized to the extent of the hardware capability. Unfortunately, the frequency of the resonant modulator was slightly off from the value that was needed for the state preparation. We attempted to use the double-passed AOM to try to bridge the gap, but were not able to completely get to the frequency. In addition, the state preparation beam is already spatially constrained. All the lasers radially enter the chamber from the same PCF. Their position is predetermined by the optimal cooling of the calcium ions in the nominal trapping location, which is spatially offset from the beryllium. This poor overlap with the beryllium ions may be an additional cause to poor state preparation. As a result, state preparation populations of $> 40\%$ were inaccessible. Nonetheless, this was still enough signal to make measurements of the clock.

The clock state frequency was calibrated using Rabi style frequency scans over resonance, such as shown in Figure 7.9. A Lorentzian fit to the scan obtains the clock frequency at the current trapping field, $321.172702(6)$ MHz. At this frequency, the corresponding first order magnetic field sensitivity is $-37$ Hz/G. The repumping time was calibrated like the other nuclear transition scan described before. The exponential fit to the data in Figure 7.10 shows a repump decay time constant of $190(40)$ ms. Many experiments utilized a repump time of $200$ ms in order to keep the total experiment time from being too long.

Using the calibrated frequency scan and repump time, a Rabi time scan was performed to observe the coherence of the ions. Scans were taken for several different pulse times

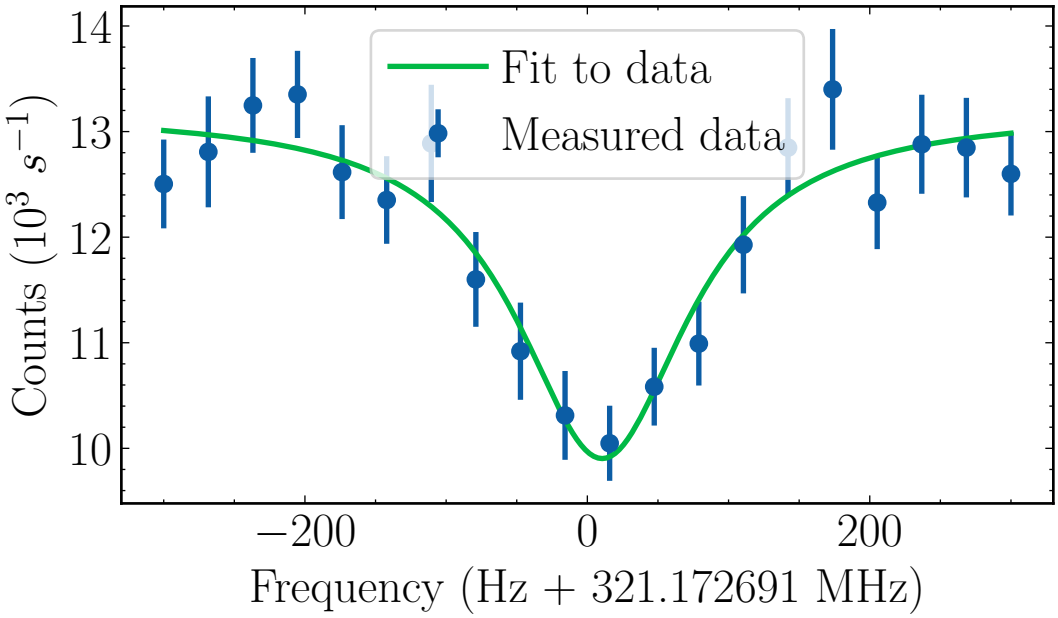


Figure 7.9: A frequency scan over the hyperfine clock frequency. This scan used 5 ms gate time, 10 ms recooling, and 5 ms of state preparation. A Lorentzian fit to the scan obtains the clock frequency at the current trapping field, 321.172702(6) MHz, with a FWHM of 150(30) Hz.

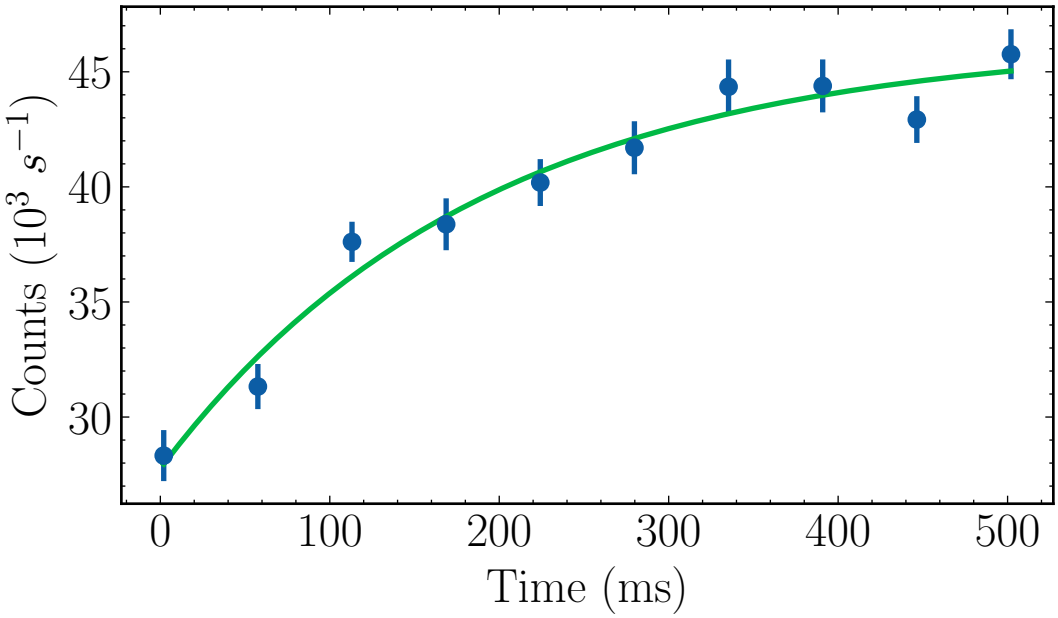


Figure 7.10: Repump scan after performing a pi transition between the clock states GS3 and GS2. The state was prepared by optical pumping. This scan uses 300 $\mu$s of state prep, 10 ms of recooling, and a gate time of 2.976 ms. The green line fit reveals a repump decay time constant of 190(40) ms.

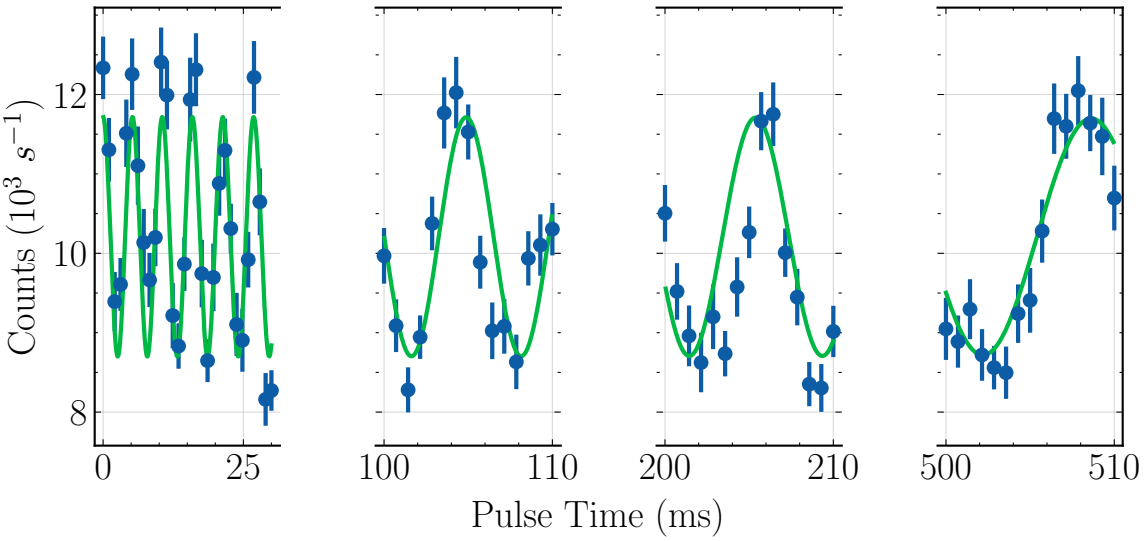


Figure 7.11: Rabi flopping on the nuclear clock ground state transition, GS3 to GS2. The fit to the dataset reveals a linearly chirped Rabi decay constant of $2.944(8)$ kHz.

with offsets to highlight the coherence maintained out to the longest scan times. These scans are shown in Figure 7.11. They show virtually no observable decoherence of the transition out to a gate time of $0.5$ s. Measurements beyond this gate time were not taken due to the long time needed for averaging a number of experiments. A decaying sinusoid was fit to the dataset, but revealed a decay time constant consistent with 0. The fit function also includes a linear decaying rabi frequency due to the observed Rabi frequency chirp. The transition's Rabi rate decreases for each of the successive scans. This is likely due to thermal effects in the resonant coil circuit used. The large currents traveling through the circuit board components heat themselves which shifts their values from the designed room temperature values. This effect appears with increasing strength for longer pulse times.

*Ramsey Sequences*

In order to measure the clock coherence, Ramsey scans were also performed. The experiments used for this data involve the same experiment described above, but the RF pulse is replaced with a pair of clock pulses separated by a variable delay. If the DDS clock remains in sync with the frequency corresponding to the energy of the ion's level spacing, then the

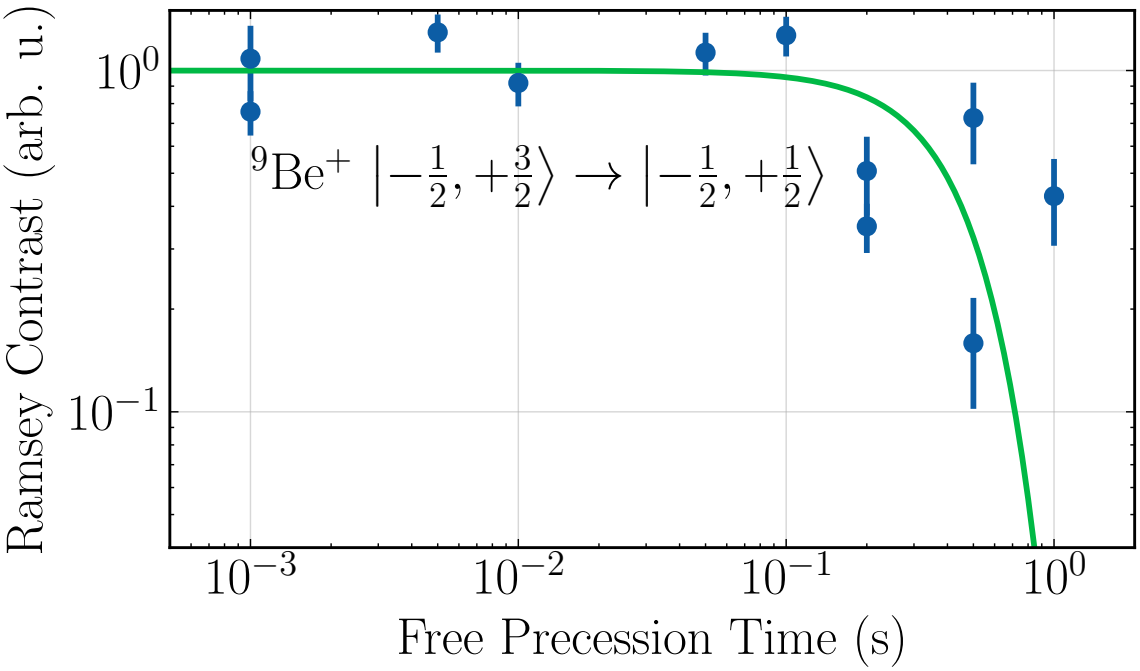


Figure 7.12: Ramsey contrast on the nuclear clock ground state transition, GS3 to GS2.

second pulse after the delay will be coherent with the first. If they are not, then the pulses will change the population of the expected output state.

For the Ramsey scans taken with this experiment, the phase of the second pulse is scanned from 0 to $2\pi$. Thus, one full sinusoidal cycle is measured. A fit to the data reveals the amplitude of the population change from the second pulse phase. The measurement is performed at multiple Ramsey times and compared to the contrast seen for a scan with no Ramsey delay. The data in Figure 7.12 is fit to a Gaussian distribution, $e^{-(t/\tau)^2}$. The fit gives a decay time constant of $0.5(1)$, but this does not agree with the amplitude for the Rabi flop observed in Figure 7.11. The decay is likely due to a fluctuating magnetic field over the longest measurement times of $\sim 30$ minutes. We can expect a frequency drift of the ions due to a change in the magnet temperature. The $0.5$ s decay time is consistent with a fractional magnetic field fluctuation of $4 \times 10^{-6}$, which is roughly consistent with the measurements in Figure 5.8.

## 7.3 Error Budget

With the given parameters of the demonstrated apparatus, we can calculate what the dominant sources of uncertainty are. This enables us to create and error budget with bounded uncertainties.

### 7.3.1 Uncertainty

When performing Ramsey spectroscopy for an atomic clock, the fundamental performance is limited by uncertainty of the systematic perturbations and the ensemble characteristics. A summary of these uncertainty contributions is seen in Table 7.1.

The number of particles and the Ramsey time of the sequence gives rise to the fundamental quantum projection noise limit. This uncertainty is given by

$$\Delta\nu/\nu_0 = \frac{1}{2\pi\nu_0\sqrt{Nt_R\tau}} \tag{7.1}$$

where $\nu_0$ is the clock transition frequency, $N$ is the number of ions, $t_R$ is the Ramsey phase integration time, and $\tau$ is the averaging time. Given $N = 10^6$ and $t_R = 1$ s, we should expect a clock's fractional uncertainty limited to $5 \times 10^{-13}/\sqrt{\tau}$ by the quantum projection noise.

Table 7.1: This table shows the uncertainty contributions to the clock performance. See text for details regarding the calculations of each error source.

| Error Budget for $Be^+$ Clock at $0.6540$ T (clock field is $0.6774$ T) | | |
|---|---|---|
| Type | Fractional Uncertainty | $\Delta\nu/\nu_0$ |
| Quantum projection noise limit | $\frac{1}{2\pi\nu_0\sqrt{Nt_R\tau}}$ | $5 \times 10^{-13}/\sqrt{\tau}$ |
| 2nd-order Doppler shift [21] | $\left(\frac{\omega_z}{\omega_c}\right)^2 \left(\frac{3N\omega_z q^2}{mc^3}\right)^{\frac{2}{3}} \left[0.186 + 0.15(\frac{\Delta r_s}{r_{so}})^2\right]$ | $< 3 \times 10^{-19}$ |
| Rotating Wall, AC Zeeman Shift | $\left(\frac{\mu_N V_{wall}}{d_{trap} ch\nu_0}\right)^2 \frac{\Delta V_{wall}}{V_{wall}}$ | $2 \times 10^{-20}$ |
| 1st Order Magnet Temperature Drift | $\frac{1}{\nu_0}\frac{d\nu}{dB}\alpha_B^{(1)} B\Delta T_{mag}$ | $2 \times 10^{-11}$ |
| Blackbody AC Zeeman Shift [114] | $2.6 \times 10^{-17}(\frac{T}{300K})(\frac{\Delta T}{300K})$ | $< 10^{-21}$ |
| Ion Crystal Heating | $\frac{k_B}{mc^2}\left(\frac{dT_{ion}}{dt}\right) t_R$ | $2 \times 10^{-16}$ |

*Second-order Doppler Shift*

The second order Doppler shift is a result of time dilation in the rotating cloud. A calculation of this shift can be found in reference [21]. They determine that the shift is

$$\frac{\Delta\nu}{\nu_0} = \left(\frac{\omega_z}{\omega_c}\right)^2 \left(\frac{3N\omega_z q^2}{mc^3}\right)^{\frac{2}{3}} \left[0.186 + 0.15(\frac{\Delta r_s}{r_{so}})^2\right]. \tag{7.2}$$

The shift depends upon the axial trap frequency $\omega_z$, the bare cyclotron frequency $\omega_c$, the number of ions $N$, the ion cloud radius instability $\Delta r_s/r_{so}$, and constants like the mass $m$ and ion charge $q$. Given an axial frequency of $2\pi \times 232$ kHz, a cyclotron frequency of $2\pi \times 1.114$ MHz, $10^6$ ions, and a fractional radial instability of $0.01$ we should expect a fractional shift of $-3 \times 10^{-19}$. Tan et al. (1995) determines that jitter of this shift at the $1\%$ level should be achievable [21]. The uncertainty will be a fraction of the shift value, so the overall fractional uncertainty is $< 3 \times 10^{-19}$.

*Rotating Wall, AC Zeeman Shift*

When the ion cloud rotation rate is stabilized with the "rotating wall," the oscillating potential causes an AC Zeeman shift to the clock states. The fractional frequency shift is shown in Table 7.1,

$$\frac{\Delta\nu}{\nu_0} = \left(\frac{\mu_N V_{wall}}{d_{trap} ch\nu_0}\right)^2 \frac{\Delta V_{wall}}{V_{wall}} \tag{7.3}$$

where $\mu_N$ is the nuclear magneton, $V = 0.5$ V is the magnitude of the voltage on the ring electrodes, $d \sim 6$mm is the ion cloud-ring electrode distance, $\nu_0 = 321$ MHz is the clock frequency at our trap field, and $\Delta V_{wall}/V_{wall}$ is the fractional voltage error. If we choose common parameters for our trap: a voltage error at the bit depth of a 16-bit DAC, $\Delta V_{wall} = 300 \times 10^{-6}$, a trap dimension of $\sim 5.7$ mm, and a wall voltage of $0.5$ V, we should see $\Delta\nu/\nu_0 = 3 \times 10^{-20}$.

*Magnet Temperature Drift*

Permanent magnets have field fluctuations which are a function of their temperature fluctuations. The magnetization of the magnets is temperature dependent. But our clock transition is first order insensitive to magnetic field fluctuations at the clock field. Thus, the theoretical fractional frequency shift due to the magnet temperature is,

$$\frac{\Delta\nu}{\nu_0} = \frac{1}{\nu_0}\frac{d^2\nu}{dB^2}(\alpha_B^{(1)} B \Delta T_{mag})^2 \tag{7.4}$$

where the $d^2\nu/dB^2$ is the second order dependence, $\alpha_B^{(1)}$ is the magnet temperature sensitivity, $B$ is the overall trapping field strength, and $\Delta T_{mag}$ is the magnitude of temperature fluctuations. However, for the final data taken at the magnetic field center, we are not at the clock field, so the first order sensitivity dominates.

$$\frac{\Delta\nu}{\nu_0} = \frac{1}{\nu_0}\frac{d\nu}{dB}\alpha_B^{(1)} B \Delta T_{mag} \tag{7.5}$$

For this trap, the field sensitivity of NdFeB is $0.12\%$ per degree Kelvin, the clock transition dependence at our magnetic field strength is $d\nu/dB = -37$ Hz/G, and the trapping field is $B = 0.6540$ Tesla. We can use the magnetic field stability given by the fractional Allan deviation of Figure 5.8, at 20 ppb. We assume $\Delta T_{mag}$ is 20 $\mu$K, we should expect magnetic field variations $\Delta B = 2 \times 10^{-8}$ Tesla. These parameters give a fractional frequency uncertainty of $2 \times 10^{-11}$.

*Blackbody, AC Zeeman Shift*

Blackbody radiation from the experiment's surrounding vacuum chamber and electrodes will cause another frequency shift. A shift of this kind on the hyperfine structure of hydrogen and alkali atoms is discussed in Ref. [114]. The result in Itano's work describes the shift by the formula in Table 7.1, where $T$ is the temperature of the blackbody, and $\Delta T$ is

the magnitude of the temperature fluctuations. If we assume, a room temperature blackbody, and a temperature fluctuation like mentioned above, we should expect a fractional frequency shift of $< 10^{-21}$.

*Ion Crystal Heating*

Another error source for trapped ion clocks is the crystal heating rate. The expression for this error source is shown in the last row of Table 7.1, where $k_B$ is Boltzmann's constant, $dT_{ion}/dt$ is the crystal's heating rate, $t_R$ is the Ramsey integration time, $m$ is the ion mass, and $c$ is the speed of light in vacuum. For a $1$ second Ramsey time and a heating rate of $20$ mK/s, we should expect a fractional frequency uncertainty of $2 \times 10^{-16}$.

## 7.4 Summary

Using our permanent magnet Penning trap, we performed spectroscopy of many of the transitions in the ground state of beryllium. Even at a trap magnetic field strength hundreds of gauss from the clock field, the transition still retains some of its insensitivity. This is exemplified by the coherence measured in the Ramsey experiments and the undetectable decay of the Rabi flop amplitude out to $0.5$ s. The error budget is calculated and the contributions to the fractional uncertainty are calculated for our trap parameters. This chapter demonstrates a major step towards a compact Penning trap atomic clock.

# CHAPTER 8

# LIMITS OF THE CURRENT SYSTEM AND THE FATE OF BERYLLIUM

While working towards the clock transition measurement in beryllium, several challenges were encountered which can be solved by making some changes to the system. Sympathetic cooling of calcium-beryllium is not very efficient. The first trap design had an inhomogenous magnetic field due to the complexity of shimming the magnets and correctly orienting the magnet positions. The temperature sensitivity of the N52 NdFeB permanent magnets is large enough to cause a problem for measuring weak transitions. The reaction rate of beryllium constantly depletes the clock signal.

Co-trapping of two ion species is advantageous for trapped ion clock operation. With sufficient Coulomb coupling between the trapped species and given enough time, the ions should find an equilibrium where the two species reach the cooling limit of the single species being cooled. The sympathetic cooling between calcium and beryllium was limited due to the fact that the calcium ions are roughly 4x heavier than the beryllium ions.

The co-trapped ions separate radially which makes efficient cooling with a single radial beamline with two laser frequencies difficult. The optimal beam placement of a single beam (output from the same fiber) is slightly different for the two species, though it may be possible to get the ideal torques for a singular position by detuning the laser frequency to the right value. Alternatively, this problem can be circumvented by using separated laser beam paths.

The magnetic field gradient that exists in our trap places a limit on how well pulses can be carried out. If the length of an RF or microwave pulse isn't much shorter than a rotation period of $\ll 20\ \mu$s, the ions will traverse a magnetic field gradient. This problem also applies to Ramsey sequences, where the spins of each ion will precess at different rates during the Ramsey free precession time, causing decoherence. This problem can be avoided

in an inhomogeneous field environment if the transition sensitivity is low enough that the field variation is a small effect to the transition resonance, as shown for the beryllium clock transition measurements of the previous chapter. In our experiments, the ions were transported to the magnetic field center to minimize the gradient sampled. However, this transport also meant that the Doppler cooling lasers were no longer aligned to the ions. In order to get higher performance gates, the sympathetic cooling from the calcium ions during the experiment was sacrificed. The alternate solution to produce high fidelity pulses is to implement the pulses fast enough that the ions do not have time to sample different magnetic fields. In our trap with rotation rates up to $100$ kHz, this would mean gates times much faster than the single cycle rotation period, $10$ $\mu$s. Transition rates approaching gates times of this magnitude could be accessible with a trap designed for integrated RF electronics or apertures with minimal shielding. A new trap design with precompensated magnetic field homogeneity would also help alleviate these concerns.

Because the trap magnetic field is not at the clock field value for the GS2 to GS3, there is still first order magnetic field sensitivity. Thus, the 'clock' frequency will vary due to the magnet's temperature drift. As shown in the error budget calculation, this is by far the dominate uncertainty contribution. We can avoid this problem entirely by designing new magnets with a better expectation of the field strength guided by magnet measurements. The N52 grade magnets from some companies appear to have a magnetization more similar to N42. In addition, we can use a temperature compensated magnetic material such as a proprietary SmCo alloy with 100x less magnetic sensitivity.

The largest problem encountered when working with beryllium in this trap is the reaction rate with background $H_2$. When Doppler cooling $^9Be^+$, the ions readily reacts with background hydrogen gas in the vacuum system to form $BeH^+$. The Doppler cooling lasers help cause this problem, but do not photoionize the resultant molecule. Without breaking the molecule, it can react further to form $BeOH^+$ at which point there is no hope for retrieving the beryllium ions again. A deep-UV photoionization laser could be used to directly

break the $BeH^+$ molecules as they form, but would be required to be almost constantly running [112]. The continual loss of $Be^+$ would be detrimental to clock operation, because the signal-to-noise ratio (SNR) would constantly declining. Using sympathetic cooling instead of direct Doppler cooling helps to mitigate this problem most effectively for masses similar to that of $Be^+$. In this situation, the ions would be at risk to reaction only during a detection period. Alternatively, the background gas pressure, and thus the reaction rate, can be reduced further if the vacuum system is cooled with a cryostat [115]. However, this would greatly increase the size of the apparatus and defeat the purpose of working with permanent magnets as opposed to a cryogenically cooled superconductor.

The issues mentioned above can be corrected with a new trap design, ion species, and/or clock scheme. A new trap could be designed with fixed magnets inside the vacuum chamber. A temperature insensitive magnetic alloy could be used that is vacuum compatible. The magnet construction could be shimmed before insertion into the vacuum system for optimal field uniformity. Additionally, we could move to another ion whose hydride formation could be dissociated easily with a diode laser or LED. Ideally, this ion species would have another ion of similar mass that could be used for sympathetic cooling.

## REFERENCES


[1] B. J. McMahon, C. Volin, W. G. Rellergert, and B. C. Sawyer, "Doppler-cooled ions in a compact reconfigurable Penning trap," *Physical Review A*, vol. 101, no. 1, p. 013 408, Jan. 2020.

[2] P. Toschek, "Hans Dehmelt (1922–2017)," *Nature*, vol. 545, no. 7654, pp. 290–290, May 2017.

[3] *Wolfgang Paul*, Aug. 2017. [Online]. Available: https://physicstoday.scitation.org/do/10.1063/PT.6.6.20170810a/abs/ (visited on 07/10/2021).

[4] *The traps of Paul and Dehmelt*. [Online]. Available: https://www.nobelprize.org/prizes/physics/1989/9747-the-traps-of-paul-and-dehmelt/ (visited on 07/05/2021).

[5] R. X. Schüssler, H. Bekker, M. Braß, H. Cakir, J. R. Crespo López-Urrutia, M. Door, P. Filianin, Z. Harman, M. W. Haverkort, W. J. Huang, P. Indelicato, C. H. Keitel, C. M. König, K. Kromer, M. Müller, Y. N. Novikov, A. Rischka, C. Schweiger, S. Sturm, S. Ulmer, S. Eliseev, and K. Blaum, "Detection of metastable electronic states by Penning trap mass spectrometry," *Nature*, vol. 581, no. 7806, pp. 42–46, May 2020.

[6] S. Rau, F. Heiße, F. Köhler-Langes, S. Sasidharan, R. Haas, D. Renisch, C. E. Düllmann, W. Quint, S. Sturm, and K. Blaum, "Penning trap mass measurements of the deuteron and the HD + molecular ion," *Nature*, vol. 585, no. 7823, pp. 43–47, Sep. 2020.

[7] M. P. Bradley, J. V. Porto, S. Rainville, J. K. Thompson, and D. E. Pritchard, "Penning Trap Measurements of the Masses of $^{133}Cs$, $^{87,85}Rb$, and $^{23}Na$ with Uncertainties $\ensuremath{\le}0.2$ ppb," *Physical Review Letters*, vol. 83, no. 22, pp. 4510–4513, Nov. 1999.

[8] C. Smorra, S. Sellner, M. J. Borchert, J. A. Harrington, T. Higuchi, H. Nagahama, T. Tanaka, A. Mooser, G. Schneider, M. Bohman, K. Blaum, Y. Matsuda, C. Ospelkaus, W. Quint, J. Walz, Y. Yamazaki, and S. Ulmer, "A parts-per-billion measurement of the antiproton magnetic moment," *Nature*, vol. 550, no. 7676, pp. 371–374, Oct. 2017.

[9] S. Stahl, F. Galve, J. Alonso, S. Djekic, W. Quint, T. Valenzuela, J. Verdú, M. Vogel, and G. Werth, "A planar Penning trap," *European Physical Journal D*, 2005.

[10] D. R. Crick, S. Donnellan, S. Ananthamurthy, R. C. Thompson, and D. M. Segal, "Fast shuttling of ions in a scalable Penning trap array," *Review of Scientific Instruments*, vol. 81, no. 1, p. 013 111, Jan. 2010.

[11] M. J. Biercuk, H. Uys, A. P. Vandevender, N. Shiga, W. M. Itano, and J. J. Bollinger, "HIGH-FIDELITY QUANTUM CONTROL USING ION CRYSTALS IN A PENNING TRAP," *Quantum Information and Computation*, Jun. 2003.

[12] J. G. Bohnet, B. C. Sawyer, J. W. Britton, M. L. Wall, A. M. Rey, M. Foss-Feig, and J. J. Bollinger, "Quantum spin dynamics and entanglement generation with hundreds of trapped ions," *Science*, vol. 352, no. 6291, pp. 1297–1301, Jun. 2016.

[13] E. Jordan, K. A. Gilmore, A. Shankar, A. Safavi-Naini, J. G. Bohnet, M. J. Holland, and J. J. Bollinger, "Near Ground-State Cooling of Two-Dimensional Trapped-Ion Crystals with More than 100 Ions," *Physical Review Letters*, vol. 122, no. 5, p. 053 603, Feb. 2019.

[14] B. C. Sawyer, J. W. Britton, A. C. Keith, C.-C. J. Wang, J. K. Freericks, H. Uys, M. J. Biercuk, and J. J. Bollinger, "Spectroscopy and Thermometry of Drumhead Modes in a Mesoscopic Trapped-Ion Crystal Using Entanglement," *Physical Review Letters*, vol. 108, no. 21, p. 213 003, May 2012.

[15] A. Safavi-Naini, R. J. Lewis-Swan, J. G. Bohnet, M. Gärttner, K. A. Gilmore, J. E. Jordan, J. Cohn, J. K. Freericks, A. M. Rey, and J. J. Bollinger, "Verification of a Many-Ion Simulator of the Dicke Model Through Slow Quenches across a Phase Transition," *Physical Review Letters*, vol. 121, no. 4, p. 040 503, Jul. 2018.

[16] J. F. Goodwin, G. Stutter, R. C. Thompson, and D. M. Segal, "Resolved-Sideband Laser Cooling in a Penning Trap," *Physical Review Letters*, vol. 116, no. 14, p. 143 002, Apr. 2016.

[17] S. Jain, J. Alonso, M. Grau, and J. P. Home, "Scalable Arrays of Micro-Penning Traps for Quantum Computing and Simulation," *Physical Review X*, vol. 10, no. 3, p. 031 027, Aug. 2020.

[18] G. Stutter, P. Hrmo, V. Jarlaud, M. K. Joshi, J. F. Goodwin, and R. C. Thompson, "Sideband cooling of small ion Coulomb crystals in a Penning trap," *Journal of Modern Optics*, vol. 65, no. 5-6, pp. 549–559, Mar. 2018.

[19] J. J. Bollinger, D. J. Heinzen, W. M. Itano, S. L. Gilbert, and D. J. Wineland, "A 303-mhz frequency standard based on trapped be+ ions," *IEEE Transactions on Instrumentation and Measurement*, vol. 40, no. 2, pp. 126–128, Apr. 1991.

[20] K. A. Gilmore, J. G. Bohnet, B. C. Sawyer, J. W. Britton, and J. J. Bollinger, "Amplitude Sensing below the Zero-Point Fluctuations with a Two-Dimensional Trapped-Ion Mechanical Oscillator," *Physical Review Letters*, vol. 118, no. 26, p. 263 602, Jun. 2017.

[21] J. N. Tan, J. J. Bollinger, and D. J. Wineland, "Minimizing the time-dilation shift in penning trap atomic clocks," *IEEE Transactions on Instrumentation and Measurement*, vol. 44, no. 2, pp. 144–147, Apr. 1995.

[22] K. Arnold, E. Hajiyev, E. Paez, C. H. Lee, M. D. Barrett, and J. Bollinger, "Prospects for atomic clocks based on large ion crystals," *Physical Review A - Atomic, Molecular, and Optical Physics*, vol. 92, no. 3, 2015.

[23] M. Bohman, A. Mooser, G. Schneider, N. Schön, M. Wiesinger, J. Harrington, T. Higuchi, H. Nagahama, C. Smorra, S. Sellner, K. Blaum, Y. Matsuda, W. Quint, J. Walz, and S. Ulmer, "Sympathetic cooling of protons and antiprotons with a common endcap Penning trap," *Journal of Modern Optics*, vol. 65, no. 5-6, pp. 568–576, Mar. 2018.

[24] C. Smorra, K. Blaum, L. Bojtar, M. Borchert, K. Franke, T. Higuchi, N. Leefer, H. Nagahama, Y. Matsuda, A. Mooser, M. Niemann, C. Ospelkaus, W. Quint, G. Schneider, S. Sellner, T. Tanaka, S. Van Gorp, J. Walz, Y. Yamazaki, and S. Ulmer, "BASE – The Baryon Antibaryon Symmetry Experiment," *The European Physical Journal Special Topics*, vol. 224, no. 16, pp. 3055–3108, Nov. 2015.

[25] G. Schneider, A. Mooser, M. Bohman, N. Schön, J. Harrington, T. Higuchi, H. Nagahama, S. Sellner, C. Smorra, K. Blaum, Y. Matsuda, W. Quint, J. Walz, and S. Ulmer, "Double-trap measurement of the proton magnetic moment at 0.3 parts per billion precision," *Science*, vol. 358, no. 6366, pp. 1081–1084, Nov. 2017.

[26] J. W. Britton, B. C. Sawyer, A. C. Keith, C.-C. J. Wang, J. K. Freericks, H. Uys, M. J. Biercuk, and J. J. Bollinger, "Engineered two-dimensional Ising interactions in a trapped-ion quantum simulator with hundreds of spins," *Nature*, vol. 484, no. 7395, pp. 489–492, Apr. 2012.

[27] R. J. Lewis-Swan, A. Safavi-Naini, J. J. Bollinger, and A. M. Rey, "Unifying scrambling, thermalization and entanglement through measurement of fidelity out-of-time-order correlators in the Dicke model," *Nature Communications*, vol. 10, no. 1, p. 1581, Apr. 2019.

[28] K. Koo, J. Sudbery, D. M. Segal, and R. C. Thompson, "Doppler cooling of Ca + ions in a Penning trap," *Physical Review A*, vol. 69, no. 4, p. 043 402, Apr. 2004.

[29] P. Hrmo, M. K. Joshi, V. Jarlaud, O. Corfield, and R. C. Thompson, "Sideband cooling of the radial modes of motion of a single ion in a Penning trap," *arXiv:1907.02406 [physics, physics:quant-ph]*, Jul. 2019.

[30] F. Köhler, K. Blaum, M. Block, S. Chenmarev, S. Eliseev, D. A. Glazov, M. Goncharov, J. Hou, A. Kracke, D. A. Nesterenko, Y. N. Novikov, W. Quint, E. Minaya Ramirez, V. M. Shabaev, S. Sturm, A. V. Volotka, and G. Werth, "Isotope de-

pendence of the Zeeman effect in lithium-like calcium," *Nature Communications*, vol. 7, no. 1, p. 10 246, Jan. 2016.

[31] *BIPM - SI Brochure*, 2019. [Online]. Available: https : / / www . bipm . org / en / publications/si-brochure/ (visited on 12/09/2019).

[32] A. D. Ludlow, M. M. Boyd, J. Ye, E. Peik, and P. O. Schmidt, "Optical Atomic Clocks," *Preprint at arxiv.org/abs/1407.3493 (to appear on Rev. Mod. Phys.)*, pp. 1–86, 2015.

[33] N. Huntemann, B. Lipphardt, C. Tamm, V. Gerginov, S. Weyers, and E. Peik, "Improved Limit on a Temporal Variation of m p / m e from Comparisons of Yb + and Cs Atomic Clocks," *Physical Review Letters*, vol. 113, no. 21, p. 210 802, Nov. 2014.

[34] T. Rosenband, D. B. Hume, P. O. Schmidt, C. W. Chou, A. Brusch, L. Lorini, W. H. Oskay, R. E. Drullinger, T. M. Fortier, J. E. Stalnaker, S. A. Diddams, W. C. Swann, N. R. Newbury, W. M. Itano, D. J. Wineland, and J. C. Bergquist, "Frequency Ratio of Al+ and Hg+ Single-Ion Optical Clocks; Metrology at the 17th Decimal Place," *Science*, vol. 319, no. 5871, pp. 1808–1812, Mar. 2008.

[35] J. Kitching, "Time for a Better Receiver," *GPS World*, p. 6, Nov. 2007.

[36] Sickle, Jan Van, *Lesson 1: The GPS Signal — GEOG 862: GPS and GNSS for Geospatial Professionals*. [Online]. Available: https://www.e-education.psu.edu/geog862/node/1407 (visited on 12/04/2019).

[37] T. Nicholson, S. Campbell, R. Hutson, G. Marti, B. Bloom, R. McNally, W. Zhang, M. Safronova, G. Strouse, W. Tew, and J. Ye, "Systematic evaluation of an atomic clock at 2 × 10-18 total uncertainty," *Nature Communications*, vol. 6, 2015.

[38] S. M. Brewer, J.-S. Chen, A. M. Hankin, E. R. Clements, C. W. Chou, D. J. Wineland, D. B. Hume, and D. R. Leibrandt, "Al + 27 Quantum-Logic Clock with a Systematic Uncertainty below 10 - 18," *Physical Review Letters*, vol. 123, no. 3, p. 033 201, Jul. 2019.

[39] N. Hinkley, J. A. Sherman, N. B. Phillips, M. Schioppo, N. D. Lemke, K. Beloy, M. Pizzocaro, C. W. Oates, and A. D. Ludlow, "An atomic clock with 10(-18) instability.," *Science (New York, N.Y.)*, vol. 341, no. 6151, pp. 1215–8, Sep. 2013.

[40] C. Chou, D. Hume, J. Koelemeij, D. Wineland, and T. Rosenband, "Frequency Comparison of Two High-Accuracy Al + Optical Clocks," *Physical Review Letters*, vol. 104, no. 7, p. 070 802, Feb. 2010.

[41] J. Kitching, "Chip-scale atomic devices," *Applied Physics Reviews*, 2018.

[42] J. A. Barnes, A. R. Chi, L. S. Cutler, D. J. Healey, D. B. Leeson, E. T. McGunigal, J. A. Mullen, W. L. Smith, R. L. Sydnor, R. F. C. Vessot, and G. M. R. Winkler, "Characterization of Frequency Stability," *IEEE Transactions on Instrumentation and Measurement*, 1971.

[43] *5071A — Microsemi*, 2019. [Online]. Available: https://www.microsemi.com/product-directory/cesium-frequency-references/4115-5071a-cesium-primary-frequency-standard (visited on 07/28/2019).

[44] *Low Noise CSAC (LN-CSAC) — Microsemi*, 2019. [Online]. Available: https://www.microsemi.com/product-directory/embedded-clocks-frequency-references/4518-low-noise-csac-ln-csac (visited on 07/28/2019).

[45] *Rubidium Frequency Standard - FS725*, 2015. [Online]. Available: https://www.thinksrs.com/products/fs725.html (visited on 07/28/2019).

[46] P. D. D. Schwindt, Y. Jau, H. L. Partner, D. K. Serkland, A. Ison, A. McCants, E. Winrow, J. Prestage, J. Kellogg, N. Yu, C. D. Boschen, I. Kosvin, D. Mailloux, D. Scherer, C. Nelson, A. Hati, and D. A. Howe, "Miniature trapped-ion frequency standard with171Yb+," in *2015 Joint Conference of the IEEE International Frequency Control Symposium the European Frequency and Time Forum*, Apr. 2015, pp. 752–757.

[47] H. L. Partner, "Development and Characterization of a 171Yb+ Miniature Ion Trap Frequency Standard," Ph.D. dissertation, University of New Mexico, Aug. 2012.

[48] P. Phoonthong, M. Mizuno, K. Kido, and N. Shiga, "Determination of the absolute microwave frequency of laser-cooled $$ˆ{171}\hbox {Yb}ˆ+$$ 171 Yb +," *Applied Physics B*, vol. 117, no. 2, pp. 673–680, Nov. 2014.

[49] E. A. Burt, J. D. Prestage, R. L. Tjoelker, D. G. Enzer, D. Kuang, D. W. Murphy, D. E. Robison, J. M. Seubert, R. T. Wang, and T. A. Ely, "Demonstration of a trapped-ion atomic clock in space," *Nature*, vol. 595, no. 7865, pp. 43–47, Jul. 2021.

[50] J. .-S. Chen, S. M. Brewer, D. B. Hume, C. W. Chou, D. J. Wineland, and D. R. Leibrandt, "Sympathetic ground state cooling and time-dilation shifts in an $ˆ{27}\text{Al}ˆ+$ optical clock," 2016.

[51] V. Gomer, H. Strauss, and D. Meschede, "A compact Penning trap for light ions," *Applied Physics B*, vol. 60, no. 2-3, pp. 89–94, 1995.

[52] J. N. Tan, S. M. Brewer, and N. D. Guise, "Penning traps with unitary architecture for storage of highly charged ions," *Review of Scientific Instruments*, vol. 83, no. 2, p. 023 103, Feb. 2012.

[53] L. Suess, C. D. Finch, R. Parthasarathy, S. B. Hill, and F. B. Dunning, "Permanent magnet Penning trap for heavy ion storage," *Review of Scientific Instruments*, vol. 73, no. 8, pp. 2861–2866, Aug. 2002.

[54] G. Gabrielse, L. Haarsma, and S. L. Rolston, "Open-Endcap Penning Traps for High-Precision Experiments," *International Journal of Mass Spectrometry and Ion Processes*, vol. 88, 319–332 ST – Open–Endcap Penning Traps for High–P, 1989.

[55] L. S. Brown and G. Gabrielse, "Precision spectroscopy of a charged particle in an imperfect Penning trap," *Physical Review A*, vol. 25, no. 4, pp. 2423–2425, Apr. 1982.

[56] G. Gabrielse, "The true cyclotron frequency for particles and ions in a Penning trap," *International Journal of Mass Spectrometry*, vol. 279, no. 2, pp. 107–112, Jan. 2009.

[57] A. Shankar, C. Tang, M. Affolter, K. Gilmore, D. H. E. Dubin, S. Parker, M. J. Holland, and J. J. Bollinger, "Broadening of the drumhead-mode spectrum due to in-plane thermal fluctuations of two-dimensional trapped ion crystals in a Penning trap," *Physical Review A*, vol. 102, no. 5, p. 053 106, Nov. 2020, Publisher: American Physical Society.

[58] C. J. Foot, *Atomic physics*, ser. Oxford master series in physics 7. Atomic, Optical, and laser physics. Oxford ; New York: Oxford University Press, 2005, OCLC: ocm57478010, ISBN: 978-0-19-850695-9 978-0-19-850696-6.

[59] J. J. Sakurai and S. F. Tuan, *Modern quantum mechanics*, Rev. ed. Reading, Mass: Addison-Wesley Pub. Co, 1994, ISBN: 978-0-201-53929-5.

[60] B. H. Bransden and C. J. Joachain, *Physics of atoms and molecules*, 2nd ed. Harlow, England ; New York: Prentice Hall, 2003, ISBN: 978-0-582-35692-4.

[61] *Atomic Data for Beryllium (Be)*. [Online]. Available: https://physics.nist.gov/PhysRefData/Handbook/Tables/berylliumtable1.htm (visited on 03/14/2021).

[62] E. J. Salumbides, V. Maslinskas, I. M. Dildar, A. L. Wolf, E.-J. van Duijn, K. S. E. Eikema, and W. Ubachs, "High-precision frequency measurement of the 423-nm Ca i line," *Physical Review A*, vol. 83, no. 1, p. 012 502, Jan. 2011.

[63] D. M. Lucas, A. Ramos, J. P. Home, M. J. McDonnell, S. Nakayama, J.-P. Stacey, S. C. Webster, D. N. Stacey, and A. M. Steane, "Isotope-selective photoionization for calcium ion trapping," *Physical Review A*, vol. 69, no. 1, p. 012 711, Jan. 2004, Publisher: American Physical Society.

[64] C. Shi, F. Gebert, C. Gorges, S. Kaufmann, W. Nörtershäuser, B. K. Sahoo, A. Surzhykov, V. A. Yerokhin, J. C. Berengut, F. Wolf, J. C. Heip, and P. O. Schmidt, "Unexpectedly large difference of the electron density at the nucleus in the 4p $^2$P$_{1/2,3/2}$ fine-structure doublet of Ca$^+$," *Applied Physics B*, vol. 123, no. 1, p. 2, Jan. 2017.

[65] R. Gerritsma, G. Kirchmair, F. Zaehringer, J. Benhelm, R. Blatt, and C. F. Roos, "Precision measurement of the branching fractions of the 4P3/2 decay of Ca II," *The European Physical Journal D*, vol. 50, no. 1, pp. 13–19, Nov. 2008.

[66] J. Fuhr and W. Wiese, *NIST Atomic Transition Probability Tables*, 77th, D. Lide, Ed. Boca Raton, FL: CRC Handbook of Chemistry & Physics, 1996.

[67] Y. Wan, F. Gebert, J. B. Wübbena, N. Scharnhorst, S. Amairi, I. D. Leroux, B. Hemmerling, N. Lörch, K. Hammerer, and P. O. Schmidt, "Precision spectroscopy by photon-recoil signal amplification," *Nature Communications*, vol. 5, no. 1, p. 3096, Jan. 2014.

[68] M. Ramm, T. Pruttivarasin, M. Kokish, I. Talukdar, and H. Häffner, "Precision Measurement Method for Branching Fractions of Excited P 1 / 2 States Applied to Ca + 40," *Physical Review Letters*, vol. 111, no. 2, p. 023 004, Jul. 2013.

[69] M. Chwalla, J. Benhelm, K. Kim, G. Kirchmair, T. Monz, M. Riebe, P. Schindler, A. S. Villar, W. Hänsel, C. F. Roos, R. Blatt, M. Abgrall, G. Santarelli, G. D. Rovera, and P. Laurent, "Absolute Frequency Measurement of the Ca + 40 4 s S 1 / 2 2 - 3 d D 5 / 2 2 Clock Transition," *Physical Review Letters*, vol. 102, no. 2, p. 023 002, Jan. 2009.

[70] P. A. Barton, C. J. S. Donald, D. M. Lucas, D. A. Stevens, A. M. Steane, and D. N. Stacey, "Measurement of the lifetime of the $3d
^{2}{D}_{5/2}$ state in $
^{40}{\mathrm{Ca}}^{+}$," *Physical Review A*, vol. 62, no. 3, p. 032 503, Aug. 2000.

[71] A. Kramida, "Isotope shifts in neutral and singly-ionized calcium," *Atomic Data and Nuclear Data Tables*, vol. 133-134, p. 101 322, May 2020.

[72] H. Shao, Y. Huang, H. Guan, Y. Qian, and K. Gao, "Precision measurement of the 3 d D 3 / 2 2 –state lifetime in a single trapped Ca + 40," *Physical Review A*, vol. 94, no. 4, p. 042 507, Oct. 2016.

[73] F. Gebert, Y. Wan, F. Wolf, C. N. Angstmann, J. C. Berengut, and P. O. Schmidt, "Precision Isotope Shift Measurements in Calcium Ions Using Quantum Logic Detection Schemes," *Physical Review Letters*, vol. 115, no. 5, p. 053 003, Jul. 2015.

[74] G. Tommaseo, T. Pfeil, G. Revalde, G. Werth, P. Indelicato, and J. P. Desclaux, "The gJ-factor in the ground state of Ca+," *The European Physical Journal D*, vol. 25, no. 2, pp. 113–121, Aug. 2003.

[75] J. Jin and D. A. Church, "Precision lifetimes for the Ca + 4 $p$ 2 $P$ levels: Experiment challenges theory at the 1% level," *Physical Review Letters*, vol. 70, no. 21, pp. 3213–3216, May 1993.

[76] D. R. Crick, "Manipulation of Ca+ Ions in Penning Traps," May 2009, Accepted: 2010-05-19T15:30:52Z Publisher: Imperial College London.

[77] *Atomic Data for Calcium (Ca)*. [Online]. Available: https://physics.nist.gov/PhysRefData/Handbook/Tables/calciumtable1.htm (visited on 02/06/2021).

[78] A. C. Wilson, ·. C. Ospelkaus, A. P. Vandevender, J. A. Mlynek, K. R. Brown, D. Leibfried, D. J. Wineland, and C. Ospelkaus, "A 750-mW, continuous-wave, solid-state laser source at 313 nm for cooling and manipulating trapped 9 Be + ions," *Appl Phys B*, vol. 105, pp. 741–748, 2011.

[79] N. Ohmae and H. Katori, "626-nm single-frequency semiconductor laser system operated near room temperature for mW-level second-harmonic generation at 313 nm," *Review of Scientific Instruments*, vol. 90, no. 6, p. 063 201, Jun. 2019.

[80] H. Ball, M. W. Lee, S. D. Gensemer, and M. J. Biercuk, "A high-power 626 nm diode laser system for Beryllium ion trapping," *Review of Scientific Instruments*, vol. 84, no. 6, p. 063 107, Jun. 2013.

[81] S. Wolf, D. Studer, K. Wendt, and F. Schmidt-Kaler, "Efficient and robust photo-ionization loading of beryllium ions," *Applied Physics B*, vol. 124, no. 2, p. 30, Jan. 2018.

[82] T. Andersen, K. A. Jessen, and G. Sørensen, "Mean-Life Measurements of Excited Electronic States in Neutral and Ionic Species of Beryllium and Boron," *Physical Review*, vol. 188, no. 1, pp. 76–81, Dec. 1969.

[83] G. Gabrielse and F. C. Mackintosh, "Cylindrical Penning traps with orthogonalized anharmonicity compensation," *International Journal of Mass Spectrometry and Ion Processes*, vol. 57, no. 1, pp. 1–17, Apr. 1984.

[84] V. Frerichs, W. G. Kaenders, and D. Meschede, "Analytic construction of magnetic multipoles from cylindric permanent magnets," *Applied Physics A*, vol. 55, no. 3, pp. 242–249, Sep. 1992.

[85] R. Hablützel, J. Alonso, and J. Home, "Novel Atom Sources and Ultra-fast Electronic Switches for Trapped-Ion Quantum-Information Experiments," Ph.D. dissertation.

[86] H. B. Ball, "Robust Quantum Control & Verification & Quantum Simulation with Trapped Ions," Ph.D. dissertation, University of Sydney, Feb. 2018.

[87] E. A. Donley, T. P. Heavner, F. Levi, M. O. Tataw, and S. R. Jefferts, "Double-pass acousto-optic modulator system," *Review of Scientific Instruments*, vol. 76, no. 6, p. 063 112, Jun. 2005.

[88] Y. Colombe, D. H. Slichter, A. C. Wilson, D. Leibfried, D. J. Wineland, K.-f. Klein, C. P. Gonschior, D. Beer, H.-s. Eckhardt, M. Belz, J. Shannon, V. Khalilov, M. Klein, C. Jakob, L. Shang, I.-m. Chou, W. Lu, R. C. Burruss, Y. Zhang, R. Ozeri, W. M. Itano, R. B. Blakestad, J. Britton, J. Chiaverini, J. D. Jost, C. Langer, D. Leibfried, R. Reichle, S. Seidelin, J. H. Wesenberg, and D. J. Wineland, "Single-mode optical fiber for high-power, low-loss UV transmission," *Optics Express*, vol. 2222, no. 1610, pp. 1401–1409, 2014.

[89] C. D. Marciniak, H. B. Ball, A. T. .-H. Hung, and M. J. Biercuk, "Towards fully commercial, UV-compatible fiber patch cords," *Optics Express*, vol. 25, no. 14, 2017.

[90] D. R. Leibrandt and J. Heidecker, "An open source digital servo for AMO physics experiments," *arXiv:1508.06319 [physics]*, Nov. 2015.

[91] D. T. C. Allcock, T. P. Harty, M. A. Sepiol, H. A. Janacek, C. J. Ballance, A. M. Steane, D. M. Lucas, and D. N. Stacey, "Dark-resonance Doppler cooling and high fluorescence in trapped Ca-43 ions at intermediate magnetic field," *New Journal of Physics*, vol. 18, no. 2, p. 023 043, Feb. 2016.

[92] J. F. Goodwin, "Sideband Cooling to the Quantum Ground State in a Penning Trap," Ph.D. dissertation, 2015.

[93] W. M. Itano, L. R. Brewer, D. J. Larson, and D. J. Wineland, "Perpendicular laser cooling of a rotating ion plasma in a Penning trap," *Physical Review A*, vol. 38, no. 11, pp. 5698–5706, Dec. 1988.

[94] W. M. Itano and D. J. Wineland, "Laser cooling of ions stored in harmonic and Penning traps," *Physical Review A*, vol. 25, no. 1, pp. 35–54, Jan. 1982.

[95] J. J. Bollinger, J. N. Tan, W. M. Itano, D. J. Wineland, and D. H. Dubin, "Nonneutral ion plasmas and crystals in penning traps," *Physica Scripta*, vol. 1995, no. T59, pp. 352–359, 1995.

[96] J. J. Bollinger, D. J. Heinzen, F. L. Moore, W. M. Itano, D. J. Wineland, and D. H. E. Dubin, "Electrostatic modes of ion-trap plasmas," *Physical Review A*, vol. 48, no. 1, pp. 525–545, 1993.

[97] L. Brillouin, "A Theorem of Larmor and Its Importance for Electrons in Magnetic Fields," *Physical Review*, vol. 67, no. 7-8, pp. 260–266, Apr. 1945, Publisher: American Physical Society.

[98] M. D. Tinkle, R. G. Greaves, and C. M. Surko, "Modes of spheroidal ion plasmas at the Brillouin limit," in *AIP Conference Proceedings*, ISSN: 0094243X, vol. 331, Berkeley, California (USA) plasmas in traps: AIP, 1995, pp. 229–241.

[99] S. Mavadia, J. F. Goodwin, G. Stutter, S. Bharadia, D. R. Crick, D. M. Segal, and R. C. Thompson, "Control of the conformations of ion Coulomb crystals in a Penning trap," *Nature Communications*, vol. 4, no. 1, pp. 1–7, Oct. 2013.

[100] M. D. Jones and D. M. Ceperley, "Crystallization of the One-Component Plasma at Finite Temperature," *Physical Review Letters*, vol. 76, no. 24, pp. 4572–4575, Jun. 1996.

[101] H. F. Powell, D. M. Segal, and R. C. Thompson, "Axialization of Laser Cooled Magnesium Ions in a Penning Trap," *Physical Review Letters*, vol. 89, no. 9, p. 093 003, Aug. 2002.

[102] H. F. Powell, S. R. de Echaniz, E. S. Phillips, D. M. Segal, and R. C. Thompson, "Improvement of Laser Cooling of Ions in a Penning Trap by use of the Axialisation Technique," *arXiv:quant-ph/0211016*, Nov. 2002.

[103] R. J. Hendricks, E. S. Phillips, D. M. Segal, and R. C. Thompson, "Laser cooling in the Penning trap: An analytical model for cooling rates in the presence of an axializing field," *J. Phys. B: At. Mol. Opt. Phys*, vol. 41, pp. 35 301–12, 2008.

[104] E. S. Phillips, R. J. Hendricks, A. M. Abdulla, H. Ohadi, D. Crick, K. Koo, D. M. Segal, and R. C. Thompson, "Dynamics of axialized laser-cooled ions in a Penning trap," *Physical Review A*, vol. 78, no. 3, p. 032 307, Sep. 2008.

[105] S. B. Torrisi, J. W. Britton, J. G. Bohnet, and J. J. Bollinger, "Perpendicular laser cooling with a rotating-wall potential in a Penning trap," *Physical Review A*, vol. 93, no. 4, 2016.

[106] X.-P. Huang, F. Anderegg, E. M. Hollmann, C. F. Driscoll, and T. M. O'Neil, "Steady-State Confinement of Non-neutral Plasmas by Rotating Electric Fields," *Physical Review Letters*, vol. 78, no. 5, pp. 875–878, Feb. 1997.

[107] X.-P. Huang, J. J. Bollinger, T. B. Mitchell, W. M. Itano, and D. H. E. Dubin, "Precise control of the global rotation of strongly coupled ion plasmas in a Penning trap*," *Physics of Plasmas*, vol. 5, no. 5, May 1998.

[108] T. B. Mitchell, J. J. Bollinger, D. H. E. Dubin, X.-P. Huang, W. M. Itano, and R. H. Baughman, "Direct Observations of Structural Phase Transitions in Planar Crystallized Ion Plasmas," *Science*, vol. 282, no. 5392, pp. 1290–1293, Nov. 1998.

[109] S. Bharadia, M. Vogel, D. M. Segal, and R. C. Thompson, "Dynamics of laser-cooled Ca+ ions in a Penning trap with a rotating wall," *Applied Physics B*, vol. 107, no. 4, pp. 1105–1115, Jun. 2012.

[110] M. W. Chase, "NIST-JANAF Themochemical Tables, Fourth Edition," pp. 1–1951, 1998.

[111] R. Rugango, A. T. Calvin, S. Janardan, G. Shu, and K. R. Brown, "Vibronic Spectroscopy of Sympathetically Cooled CaH+," *ChemPhysChem*, vol. 17, no. 22, pp. 3764–3768, 2016.

[112] B. C. Sawyer, J. G. Bohnet, J. W. Britton, and J. J. Bollinger, "Reversing Hydride Ion Formation in Quantum Information Experiments with Be$ˆ+$," *Physical Review A*, vol. 91, no. 1, p. 011 401, Jan. 2015.

[113] R. Johnson, H. Ecker, and J. Hollis, "Determination of far-field antenna patterns from near-field measurements," *Proceedings of the IEEE*, vol. 61, no. 12, pp. 1668–1694, 1973.

[114] W. M. Itano, L. L. Lewis, and D. J. Wineland, "SHIFT OF $^2$ S $_{1/2}$ HYPERFINE SPLITTINGS DUE TO BLACKBODY RADIATION AND ITS INFLUENCE ON FREQUENCY STANDARDS," *Le Journal de Physique Colloques*, vol. 42, no. C8, pp. C8–283–C8–287, Dec. 1981.

[115] G. Gabrielse, X. Fei, L. Orozco, R. Tjoelker, J. Haas, H. Kalinowsky, T. Trainor, and W. Kells, "Thousandfold improvement in the measured antiproton mass," *Physical Review Letters*, vol. 65, no. 11, pp. 1317–1320, Sep. 1990.